学位論文

Electron scatterings and dynamics of Dirac surface state in a three-dimensional topological insulator

（三次元トポロジカル絶縁体のディラック表面状態における
電子散乱及びダイナミクス）

平成26年12月 博士（理学）申請

東京大学大学院理学系研究科
物理学専攻

金 聖憲

Electron scatterings and dynamics of Dirac surface state in a three-dimensional topological insulator

Sunghun Kim

Department of Physics, Graduate School of Science

The University of Tokyo

A thesis submitted for the degree of

Doctor of Philosophy

December, 2014

1. Reviewer: Prof. Shuji Hasegawa

2. Reviewer: Prof. Ryo Shimano

3. Reviewer: Prof. Hiroshi Fukuyama

4. Reviewer: Prof. Hidefumi Akiyama

5. Reviewer: Prof. Yusuke Kato

Day of the defense: 27, January, 2015

Abstract

The most remarkable point of the topological insulator is a metallic spin-polarized boundary state. An existence of such a state in the bulk energy gap gives a clue to distinguish the peculiar matter from an ordinary insulator. Particularly, interestingly, the edge state is described by massless Dirac equation, and a large Fermi velocity is given to electrons of the edge state. Furthermore, the edge state of the topological insulator is theoretically promised to be robust. Because of those properties, the topological insulator is highly expected to be a good material for the spintronics devices with high performance.

In case of three-dimensional (3D) topological insulator, the edge state is appeared at surface, so-called Dirac surface state. After discovery of 3D topological insulator materials, many theoretical and experimental approaches applied for understanding such a Dirac surface state. Consequently, the electronic property of the peculiar surface state has been clarified gradually in a last few years. In spite of those efforts, a dynamics of the novel surface state electrons, such as the elastic and inelastic scattering, has not been studied in detail, contrary to the electronic structures. In the present study, the dynamics originated in elastic and inelastic scattering of a 3D topological insulator is investigated. Scanning tunneling microscopy (STM) and spectroscopy (STS), as well as time- and angle-resolved photoelectron spectroscopy (TrARPES) experiments have been performed to understand the dynamics. The present thesis mainly consists two parts.

In the first part, electron backscattering in the Dirac surface state of $Bi_{1.5}Sb_{0.5}Te_{1.7}Se_{1.3}$ is clarified with STM/S and TrARPES. Fourier transformed differential conductance images suggest a critical scattering vector length. The comparison with the diameter of constant energy contour of band dispersion measured by TrARPES shows the critical vector length is limited to only 75 % of the diameter. The maximum

scattering angle is calculated to be 100° and this indicates that not only the 180° backscattering, but also a rather wide range scattering angle of 100°-180° are well prohibited due to the spin mismatch. It means the electron backscattering is suppressed with the angle dependence.

The second part of the present thesis focuses on non-equilibrium state of bulk-insulating topological insulator. A decay process of photoexcited electrons in $Bi_{1.5}Sb_{0.5}Te_{1.7}Se_{1.3}$ is clarified from directly observed transient characteristic by TrARPES. The energy dependent transient curves measured on both Dirac surface state and bulk conduction band results a long lifetime of the topological surface state's own and even longer lifetime of the bulk conduction band. The transient photoelectron intensity measured in various sample with different Fermi level shows such a long lifetime is kept in the topological insulator by keeping the bulk-insulating electronic structure. According to the present study, electron scattering process of a bulk-insulating topological insulator was understood experimentally.

Acknowledgements

At first, I would like to give special appreciation to my supervisor Prof. Fumio Komori who allowed an opportunity of studying in such a great environment that I could concentrate to progress this project. Under his intellectual guidance the work become effective. I would like to express my gratitude to my collaborators, Dr. Shunsuke Yoshizawa for his kind advice for STM experiment, as well as the analysis and Dr. Yukiaki Ishida for his great support of the time- and angle-resolved photoelectron spectroscopy experiment and discussions. It is my pleasure to acknowledge the collaboration from Prof. Shik Shin. I would like to appreciate to Dr. Toshio Miyamachi for a great advice including STM experiment and kind discussion about many interesting theme in physics. The work would be impossible without the support of high quality samples, as well as fruitful discussions from Prof. Yoichi Ando, Prof. Kouji Segawa, and Dr. Kazuma Eto.

I could send a great time in Karlsruhe Institute for Technology under kind support from Prof. Wulf Wulfhekel and all members in the group. I would like to thank to Dr. Koichiro Yaji, Mr. Takushi Iimori, Mr. Norikazu Kawamura, Dr. Masamichi Yamada, and Dr. Koichiro Ienaga for their great advice from physics to human life. Thanks to Mr. Ryu Yukawa, Mr. Yukio Takahashi, and Mr. Sogen Toyohisa that I could enjoy all of my time in Japan even in ISSP. I am very glad to give my appreciation to Prof. Iwao Matsuda and all his group members for the fruitful discussions in the weekly joint seminar. I also would like to thank to Advanced Leading Graduate Course for the Photon Science for the financial support.

Finally, I would like to express my special thank to my family. All the work cannot be accomplished without their great support from my own country.

18. December, 2014

Sunghun Kim

Contents

List of Figures **ix**

List of Tables **xi**

1 Introduction **1**

1.1 Preface of the present study 1

1.2 Purpose of the present study 2

1.3 Outline 2

2 Backgrounds **5**

2.1 Introduction to quantum spin Hall insulators 5

2.1.1 Quantum Hall state and Chern invariant 5

2.1.2 Quantum spin Hall state Z_2 topological invariant 7

2.1.3 Quantum spin Hall insulator 10

2.2 Three-dimensional topological insulators 11

2.2.1 Z_2 invariant in three-dimensional topological insulators . . . 11

2.2.2 $Bi_{1-x}Sb_x$ alloy 14

2.2.3 Chalcogen compounds 16

3 Experimental techniques **21**

3.1 Scanning tunneling microscopy 21

3.1.1 Tunneling effect 21

3.1.2 Tunneling current 23

3.1.3 Scanning tunneling spectroscopy and dI/dV map 25

3.1.4 Electron standing wave and quasiparticle interference 26

3.2 Photoelectron spectroscopy 27

3.2.1 Photoemission process 27
3.2.2 Angle-resolved photoelectron spectroscopy 31
3.2.3 Time- and angle-resolved photoelectron spectroscopy 32

4 Angle dependent suppression of electron backscattering in the topological insulator 35
4.1 Introduction 35
4.1.1 Electron backscattering in the topological insulator 35
4.1.2 3D topological insulator $Bi_{2-x}Sb_xTe_{3-y}Se_y$ 37
4.2 Experiment 39
4.3 Results and discussions 40
4.3.1 Topography and tunneling spectrum 40
4.3.2 dI/dV images and quasiparticle interferences 42
4.3.3 Band structure 46
4.3.4 Electron scattering process 48
4.4 Conclusion 50

5 Photoexcited carrier dynamics of Dirac fermion in the intrinsic topological insulator 53
5.1 Introduction 53
5.1.1 Carrier dynamics in solid surface 53
5.1.2 Dynamics of the excessive hole doped topological insulator . 53
5.2 Experiment 55
5.3 Results and discussions 56
5.3.1 Transient characteristic 56
5.3.2 Fermi level dependence 61
5.3.3 Electron-hole recombination 64
5.3.4 Electron scattering process 66
5.4 Conclusion 71

6 Summary 73

Bibliography 75

List of Figures

2.1 Ordinary insulating state and quantum Hall state 6
2.2 Quantum spin Hall state 8
2.3 Two different states of $Z_2 = 0$ and $Z_2 = 1$ 9
2.4 Quantum spin Hall effect in CdTe/HgTe/CdTe quantum well structure 10
2.5 Three-dimensional Brillouin zone with eight time-reversal invariant momenta 12
2.6 Surface states in case of $\nu_0 = 0$ and $\nu_0 = 1$ 13
2.7 Electronic property of $Bi_{1-x}Sb_x$ alloy 15
2.8 Brillouin zone and crystal structure of bismuth chalcogenide 18
2.9 Band dispersions of Bi_2Se_3 and Bi_2Te_3 19

3.1 Schematic of the electron tunneling through a one-dimensional potential barrier 22
3.2 A schematic of the STM geometry 24
3.3 Electron scattering and standing wave 26
3.4 Three step model for photoemission process 28
3.5 Inelastic mean free path of photoelectron 30
3.6 A schematic of ARPES measurement 31
3.7 A principle of TrARPES 32
3.8 A schematic of TrARPES system 34

4.1 Spin selected electron backscattering in the $Bi_{1-x}Sb_x$ alloy 36
4.2 Structural and electronic property of $Bi_{2-x}Sb_xTe_{3-y}Se_y$ 38
4.3 Pictures of sample set up for cleaving 40
4.4 Topography and tunneling spectrum of $Bi_{1.5}Sb_{0.5}Te_{1.7}Se_{1.3}$ 41

LIST OF FIGURES

4.5 Spatial distribution of Dirac point 42
4.6 Differential conductance map and Fourier transformation 43
4.7 Energy dispersion of Fourier transformed amplitude 45
4.8 Photoelectron intensity images and MDCs of $Bi_{1.5}Sb_{0.5}Te_{1.7}Se_{1.3}$ . . 47
4.9 Electron scattering angle and scattering process 49

5.1 Transient characteristic of excessively hole-doped topological insulator 54
5.2 Calibration of $t = 0$ (t_0) 56
5.3 Snapshots of the photoelectron intensity 57
5.4 Transient characteristic of surface and bulk state 59
5.5 Energy dependent decay time 60
5.6 Band dispersion and Fermi level shift 62
5.7 Fermi level dependent transient curves 62
5.8 Fermi level dependent lifetime 63
5.9 Electron - hole recombination 65
5.10 Electron scattering process model to simulate with rate equation . . 67
5.11 Transient curves of experimental results and simulations from the rate equation 69
5.12 Relaxation process in two different topological insulators 70

List of Tables

2.1 Topological number of Bi, Sb, and $Bi_{1-x}Sb_x$ 14
2.2 The parity of several chalcogen compounds 17

5.1 Parameters estimated from the simulation 69

LIST OF TABLES

Chapter 1

Introduction

1.1 Preface of the present study

Condensed matter physics has been studied in order to understand many fundamental properties of materials. In particular, with development of scanning tunneling microscope and photoelectron spectroscopy, powerful technique with surface sensitivity, has given a lot of advantage to make clear many electronic structures in the solid surface. On the other hand, the carrier dynamics on the surface is focused as much as the electronic structures. Because the carrier dynamics takes the important roles to understand the physical properties such as surface electric conductivity and electron transport. An advancement of pump-and-probe method affects many researchers to focus the surface dynamics. Accordingly, it is started to clarify the electron dynamics of various kind of materials.

A recent discovery of topological insulators [1, 2], has provided a lot of interesting subjects related to its spin-polarized Dirac metallic surface state between the insulating bulk energy gap. In order to understand such a novel state of new material, many theoretical and experimental approaches has been applied. As a consequence, the electronic properties of many candidates for the topological insulators have been revealing decently. However, in spite of such efforts, many parts of the dynamics based on the peculiar electronic states are still veiled with insufficient understanding.

1.2 Purpose of the present study

It will be described in Chapter 2 for the detail about the properties of topological insulators, an intrinsic topological insulator shows two representative properties. The first is the perfectly spin-polarized two-dimensional Dirac surface state. Due to the discriminative feature, helical spin structure appears in the constant energy contour. The second is the existence of two-dimensional metallic surface state at the Fermi level between the insulating bulk energy gap. Such new features are expected to show a new electron dynamics that these two peculiar electronic properties are focused in the present study. The eventual purpose of the present study is to understand the dynamics based on these two interesting electronic properties. In particular, 1) quantitative understanding about the suppression of electron backscattering as function of the scattering angle within spin-polarized topological surface state, expected to be protected from the backscattering, and 2) clarifying the electron scattering process, including the inelastic scattering of non-equilibrium state by photoexcitation "bulk-insulating" topological insulator are set to the detailed goals. Especially, these various approaches can give us advantages to understand the dynamics of two-dimensional surface electron in an intrinsic three-dimensional topological insulator. To clarify such dynamics of the particular surface state will suggest a new prospect for the fundamental physics, as well as the applications based on the topological insulators.

1.3 Outline

In the next chapter, Chapter 2, the theoretical and the experimental backgrounds from the birth of the topological insulators to previous studies just before the start of the present study will be described. In Chapter 3, the main experimental techniques, scanning tunneling microscopy and spectroscopy, and time- and angle-resolved photoelectron spectroscopy will be introduced. As well as, the principle of both experimental techniques will be explained. Chapter 4 is devoted to the elastic electron scattering of peculiar spin-polarized surface state in the intrinsic topological insulator of bismuth based chalcogenide, showing angle dependent scattering and the strong suppression of the backscattering. The directly observed carrier

dynamics in the intrinsic topological insulator with time- and angle-resolved photoelectron spectroscopy will be described in Chapter 5. Ultrafast carrier dynamics based on the inelastic scattering process is revealed from the obtained transient characteristic. Finally, the present study is summarized in Chapter 6.

Chapter 2

Backgrounds

2.1 Introduction to quantum spin Hall insulators

2.1.1 Quantum Hall state and Chern invariant

An insulating state is one of the most basic state with separated energy gap between the occupied valence bands and the empty conduction band. Thus such a material is electrically inert because a finite energy is essential to move an electron. In this state electrons are considered as being bound in localized orbitals as shown in Fig. 2.1(a). The discovery of the integer quantum Hall effect by von Klitzing in 1980 [3] changes a view of this property. In the quantum Hall state [3, 4] with perpendicular magnetic field, if the magnetic field is strong enough, the quantization of electrons' circular orbit leads to an energy gap as Landau levels. However, the cyclotron motions cannot be completed at the edge, which allows charge to flow in one-dimensional edge states characterized by the quantized Hall conductivity.

$$\sigma_{xy} = Ne^2/h \tag{2.1}$$

where N is known as the integer filling factor of Landau level. Because both edge states are very-well isolated, they could go around an impurity without any scattering to the opposite direction.

Because of the energy gap, the ordinary insulating state and the quantum Hall state appear similar. Interestingly, the difference between two was explained by Thouless, Kohmoto, Nightingale, and den Nijs (TKNN) with a matter of topology

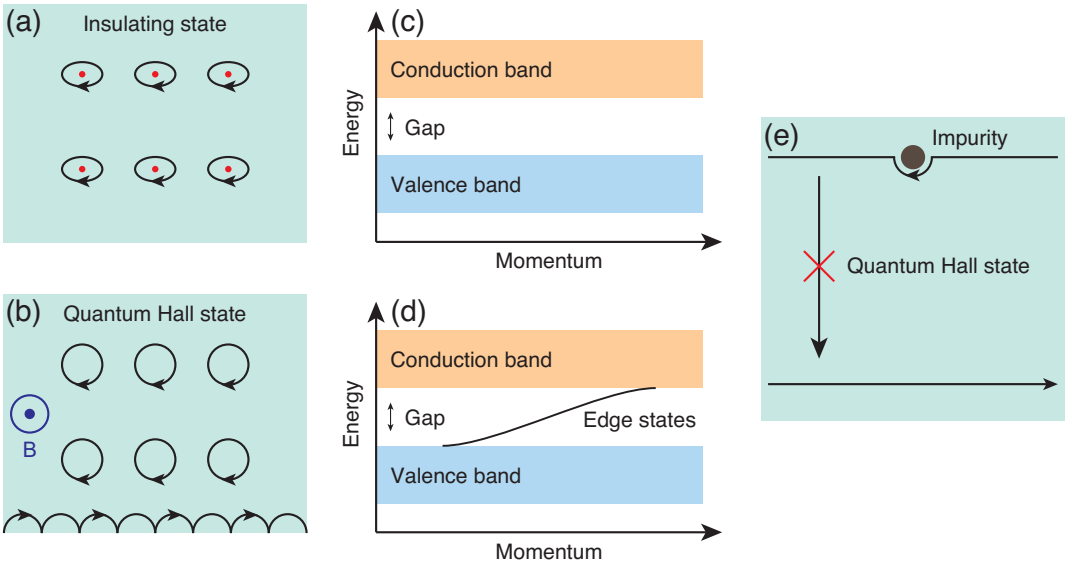

Figure 2.1: (a) Ordinary insulating state and (b) quantum Hall state in a strong magnetic field. Both of band diagrams are depict in (c) and (d), respectively. (a), (c) Electrons are bound in localized orbitals and have an energy gap opening between the filled valence band and the empty conduction band. (b), (d) The qunatum Hall states in a strong magnetic field also have a bulk energy gap as insulators, however allows conduction in the edge state along the boundary. (e) The upper and lower edge states are robust that go around an impurity without any scattering. Figures are reproduced from [5, 6].

[7, 8]. They suggested the expression for the Hall conductance σ_{xy} in a periodic system and found a topological invariant $n \in \mathrm{Z}$ (Z denotes the integers), so called Chern invariant.

The Chern invariant can be understood by Berry phase associated with Bloch functions $|u_m(\mathbf{k})\rangle$. According to TKNN formula, if l Landau levels are filled, quantized Hall conductivity can be expressed as

$$\sigma_{xy} = \frac{e^2}{\hbar} \sum_{m=1}^{l} n_m \tag{2.2}$$

where

$$n_m = \frac{1}{2\pi} \int d^2\mathbf{k} [\nabla \times \mathbf{A}(\mathbf{k})] \tag{2.3}$$

with

$$\mathbf{A}_m = i\langle u_m | \nabla_k | u_m \rangle \tag{2.4}$$

In Eq. (2.3), the term of $\nabla_k \times \mathbf{A}(\mathbf{k})$ can be expressed as a integral of Berry curvature $\mathbf{B}_m$, similar to a treatment of the vector potential in electromagnetism. They showed that N in Eq. (2.1) is identical to the total Chern number $n = \sum_{m=1}^{l} n_m$ and the Chern number n, topological invariant, is the total Berry curvatures in the momentum space. Hence it is insensitive to the detail of sample, that this nature explains the precise quantization of the Hall conductance σ_{xy} and its robustness. Such a situation is very similar to Gauss-Bonnet theorem [9]. According to Gauss-Bonnet theorem, the final result classified by the only genus, which counts the number of holes in the object. Analogously, it becomes possible to distinguish the ordinary insulating state ($n = 0$) from the quantum Hall state ($n \neq 0$) with a topological invariant.

2.1.2 Quantum spin Hall state Z_2 topological invariant

After the quantum Hall state was discovered, Haldane proposed a simple example of an integer quantum Hall state in a band theory [10] provided by honeycomb lattice as a model of two-dimensional graphite, later discovered by Novoselov and Geim, so called graphene [11]. According to the Haldane model, electrons are driven to form a conducting edge state by the periodic magnetic flux, even though the total flux is zero.

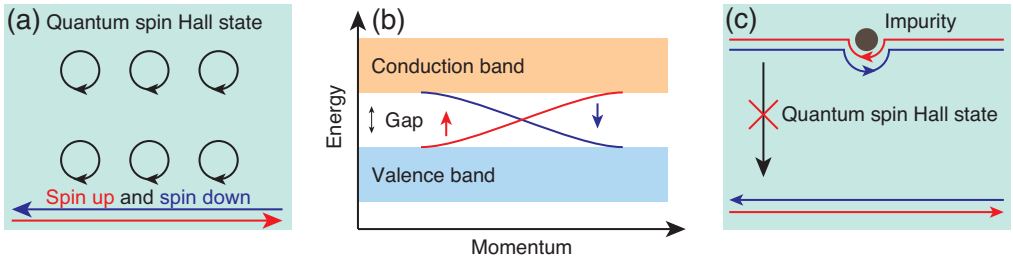

Figure 2.2: (a) A schematic of the quantum spin Hall state at zero magnetic field and (b) the band diagram. In spite of a bulk energy gap, the quantum spin Hall state allows conduction in "spin-filtered" edge states. (c) Both scattering into the opposite edge and anti-chiral edge are forbidden, which can allow the perfect transmission. Adapted from [5, 6].

Unlike Haldane model, in which lattice system with spinless electrons was used, Kane and Mele generalized Haldane model to a graphene lattice of spin 1/2 electrons with strong spin-orbit coupling [12]. The strong spin-orbit coupling was suggested to replace the periodic magnetic flux, regarded in the Haldane model, and leads to a new novel state, so called quantum spin Hall state. In contrast to the quantum Hall state, where time-reversal symmetry is violated, the quantum spin Hall state has a small bulk energy gap, and gapless spin filtered edge states on the boundary with time-reversal invariant as shown in Fig. 2.2(a). This phenomenon is explained simply by the spin-orbit coupling term of Hamiltonian, which can be given as $(\mathbf{E} \times \mathbf{p}) \cdot \sigma$ [13]. Assuming a two-dimensional plane, the Hamiltonian is written as

$$H_{SOC} \propto (E_x p_y - E_y p_x)\sigma_z = B_{eff}\sigma_z \tag{2.5}$$

Thus, electrons with opposite spin can affect each other as effective magnetic field B_{eff} perpendicular to the two-dimensional plane. Consequently, the system has opposite chiral edge states characterized by quantized conductance with fractional multiples of e^2/h, which depend on the spin. Similarly to the quantum Hall state, upper and lower edge states are robust from the scattering between the two, because of the bulk insulating property. Furthermore, in the quantum spin Hall state, time-reversal symmetry inhibit a backscattering to the opposite direction of chiral edge state. Consequently, it is expected to be a candidate for the perfect transmission with spin-polarized currents as shown in Fig. 2.2(c) [14].

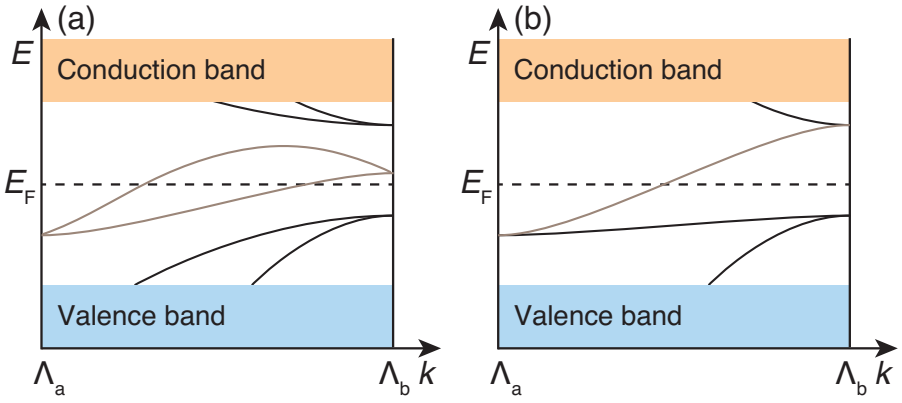

Figure 2.3: Energy dispersion between the center Λ_a ($k = 0$) and a boundary Λ_b ($k = \pi$) of Brillouin zone. The number of edge states crossing the Fermi level is (a) even ($Z_2 = 0$) and (b) odd ($Z_2 = 1$). Reproduced from [15].

In 2005, a new number of Z_2 topological invariant was proposed by Kane and Mele to distinguish the quantum spin Hall phase from an ordinary insulating state [16]. This novel Z_2 invariant, analogous to classification of the quantum Hall phase by Chern invariant, is defined for time-reversal invariant Hamiltonians. Z_2 can have only 0 or 1, which indicates even (Fig. 2.3(a)) or odd (Fig. 2.3(b)) number of times that one-dimensional edge state crosses the Fermi level between two Kramers degenerate points $k = 0$ and $k = \pi$, which are time-reversal invariant momenta, respectively.

Assuming a two-dimensional system with periodic boundary conditions along both directions, the two-dimensional Brillouin zone would have four time-reversal invariant moment. In this situation, Z_2 invariant ν can be described as

$$(-1)^{\nu} = \prod_{a=1}^{4} \frac{\mathrm{Pf}[w(\Lambda_a)]}{\sqrt{\det[w(\Lambda_a)]}} \tag{2.6}$$

where a unitary matrix $w_{ij}(\mathbf{k}) = \langle u_i(\mathbf{k})|\Theta|u_j(\mathbf{k})\rangle$, and the Pfaffian $\mathrm{Pf}[w(\Lambda_a)]$ can be defined as

$$\mathrm{Pf}[w(\Lambda_a)]^2 = \det[w(\Lambda_a)] \tag{2.7}$$

where $\det[w(\Lambda_a)]$ is a determinant of $w(\Lambda_a)$, because $w(\Lambda_a)$ is antisymmetric. Therefore, it can be possible to classify "trvial" ($\nu = 0$) and "non-trivial" ($\nu = 1$) state by Z_2 topological invariant [17].

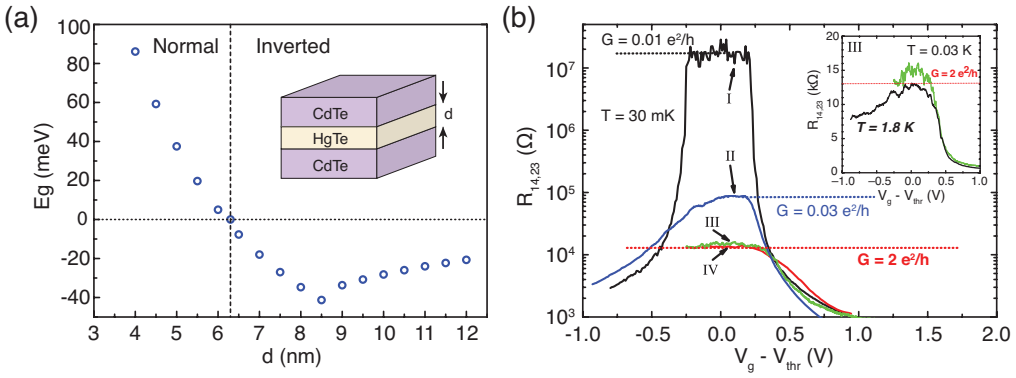

Figure 2.4: (a) A band inversion transition at the critical thickness (d_c = 6.3 nm) in the quantum well structure of HgTe between CdTe. (b) Experimental four-ternminal resistance as a function of the gate voltage with zero magnetic field. III and IV ($d > d_c$)quantized conductance while I ($d < d_c$) shows insulating behavior. Reproduced from [19].

2.1.3 Quantum spin Hall insulator

In 2006, Bernevig, Hughes and Zhang proposed a two-dimensional quantum well system of CdTe/HgTe/CdTe heterostructure as a new candidate of quantum spin Hall insulator [18]. They predicted that the electronic structure would be changed from a "normal" to an "inverted" at a certain thickness of quantum well. Soon after, in 2007, this prediction was verified experimentally by König *et al.*[19].

The energy gap size that was obtained by $\mathbf{k} \cdot \mathbf{p}$ calculation [20] is shown in Fig. 2.4(a) for the quantum well structure as shown in an inset of Fig. 2.4(a) as a function of a quantum well width d. The value of gap size changes from positive to negative at the critical thickness $d = 6.3$ nm, which represents a band inversion transition in the same system. Fig. 2.4(b) shows the resistance measurements for several different samples as a function of a gate voltage. Sample III and IV ($d_c < d = 7.3$ nm), the "inverted" regime, show a quantized conductance $2e^2/h$ associated with both top and bottom edge, while an insulating property is observed in Sample I ($d_c > d = 5.5$ nm). This quantized conductance proves the existence of the edge states due to the quantum spin Hall effect in CdTe/HgTe/CdTe quantum well system.

After the prediction of CdTe/HgTe/CdTe quantum well structure, similar two-dimensional system, AlSb/InAs/GaSb/AlSb quantum well, was predicted [21] and

experimentally confirmed [22, 23], which shows quantum spin Hall effect. In addition, other materials, Bi bilayer [24] and Na_2IrO_3 [25], are also regarded as candidates of quantum spin Hall insulators. Particularly, the topological nature of Bi bilayer was addressed first by photoemission study [26], then, the probability for the existence of the edge states was proved by scanning tunneling spectroscopy [27] and conductance measurement [28].

2.2 Three-dimensional topological insulators

2.2.1 Z_2 invariant in three-dimensional topological insulators

After the theoretical studies of quantum spin Hall state with the Z_2 topological invariant, as written in Sec. 2.1.3, the Z_2 invariant was generalized into three-dimensional topological insulators [15, 29, 30, 31]. According to those, three-dimensional time-reversal symmetric electronic structures are described by four Z_2 invariants $\nu_0; (\nu_1\nu_2\nu_3)$, rather than a single Z_2 invariant. Considering a three-dimensional Brillouin zone of cubic system as depict in Fig. 2.5, one can notice eight time-reversal invariant momenta exist. The four Z_2 invariants $\nu_0, \nu_1, \nu_2, \nu_3$ are described as

$$(-1)^{\nu_0} = \prod_{n_j=0,\pi} \delta_{n_1,n_2,n_3} \tag{2.8}$$

$$(-1)^{\nu_i} = \prod_{n_{j\neq i}=0,\pi;n_i=\pi} \delta_{n_1,n_2,n_3} \quad (i = 1, 2, 3) \tag{2.9}$$

where δ_{n_1,n_2,n_3} is defined as

$$\delta_{n_1,n_2,n_3} = \frac{\mathrm{Pf}[w(\Lambda_{n_1,n_2,n_3})]}{\sqrt{\det[w(\Lambda_{n_1,n_2,n_3})]}} = \pm 1 \tag{2.10}$$

for each time-reversal invariant momentum point. Eqs. (2.8) and (2.9) show the invariant ν_0 is the only product of eight δ, unique to a three-dimensional system, and is robust in the presence of disorder. Analogous to the two-dimensional case, a topological phase ($\nu_0 = 1$) can be distinguished from an ordinary three-dimensional insulating state ($\nu_0 = 0$). A matter with the three-dimensional topological phase is

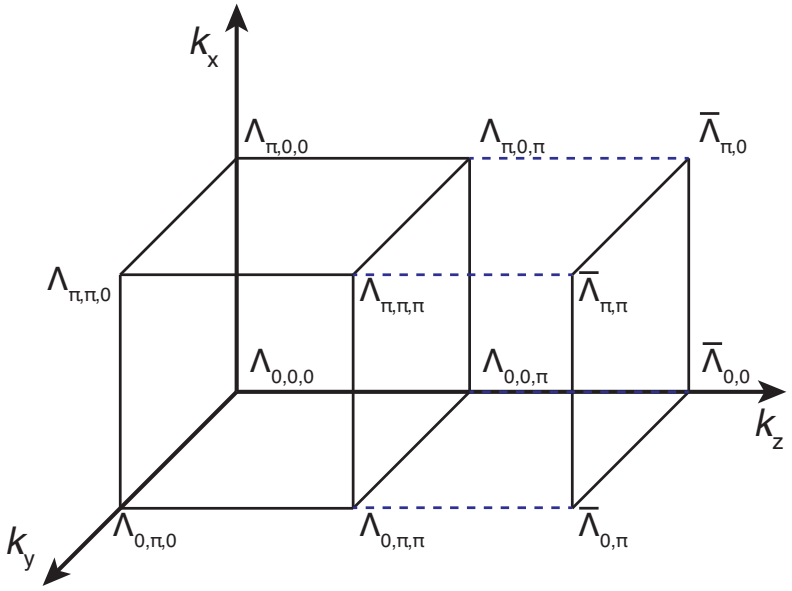

Figure 2.5: Eight time-reversal invariant momenta in a three-dimensional Brillouin zone (a cubic case), and its projection to two-dimensional plane

called as "Topological insulator", which possesses spin-polarized surface states, instead of the spin-filtered one-dimensional edge states in the two-dimensional quantum spin Hall insulators.

Assuming a two-dimensional projection of three-dimensional Brillouin zone as shown in Fig. 2.5, the number of times surface bands to cross Fermi level between arbitrary time-reversal invariant momenta $\bar{\Lambda}_i$ and $\bar{\Lambda}_j$ depends on the surface fermion parities $\pi(\bar{\Lambda}_a)\pi(\bar{\Lambda}_b) = \pm 1$, respectively, where $\pi(\bar{\Lambda}_a) = \delta(\mathbf{k}_{a1})\delta(\mathbf{k}_{a2})$. Thus, there are separated two surface Brillouin zone regions, in which time-reversal invariant momenta with $+1$ or -1, by the Fermi surface boundary. Generally, each region contains odd (even) number of time-reversal invariant momenta when $\nu_0 = 1$ ($\nu_0 = 0$) as shown in Figs. 2.6(b) and 2.6(a) [15]. By Kramers' theorem, a pair of spin-polarized bands should be degenerate at $\bar{\Lambda}_i$ ($i = a, b, c, d$) due to the time-reversal symmetry. Considering degenerated surface bands at $\bar{\Lambda}_a$, when $\nu_0 = 1$, each spin-polarized surface band degenerates with different spin-polarized band at $\bar{\Lambda}_b$, while the same pair degenerate at $\bar{\Lambda}_b$ as $\bar{\Lambda}_a$ for $\nu_0 = 0$. Fig. 2.6(c) and 2.6(d) describe this "parter switching" well. The distinction between $\nu_0 = 0$ and $\nu_0 = 1$ is quite similar to the two-dimensional one, which can be easily understood by

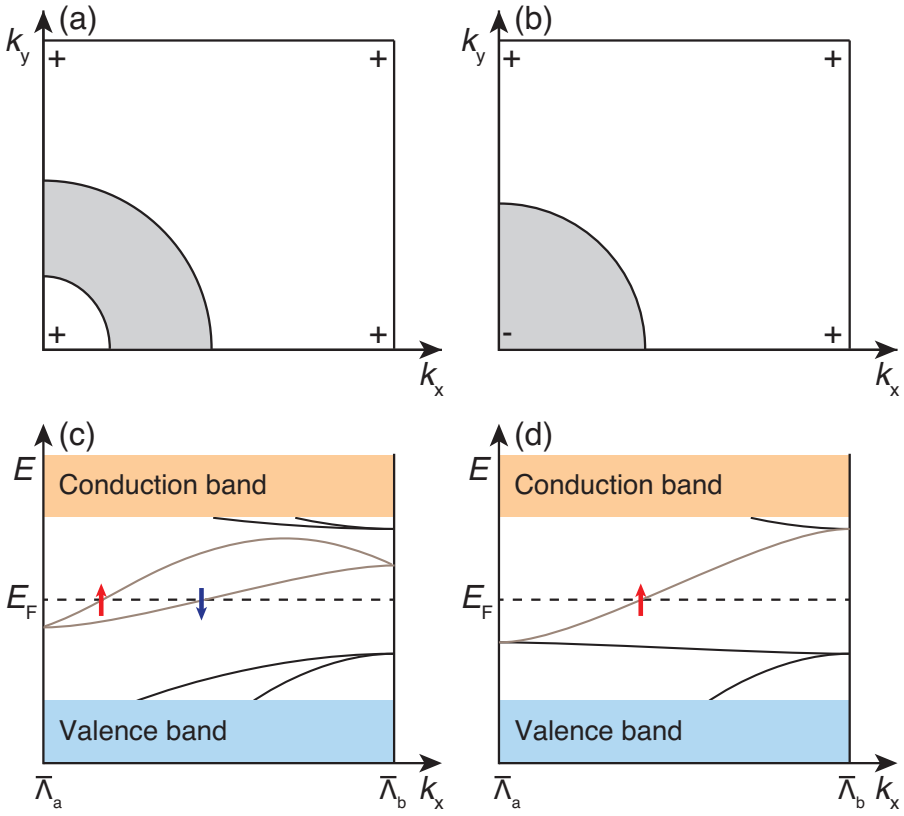

Figure 2.6: Surface Brillouin zone for (a) $\nu_0 = 0$ and (b) $\nu_0 = 1$. White and grey region indicate two separated region by Fermi surface boundary. (c), (d) Surface band dispersions along k_x direction, corresponding to (a) and (b), respectively. A pair of spin-polarized surface bands degenerate at $\bar{\Lambda}_b$ with (c) same band and (d) different spin-polarized band. Adapted from [15].

Material	$\delta\Gamma$	δ(T)	δ(L)	δ(X)	ν_0
Bi	-1	-1	-1	-1	0
Sb	-1	-1	+1	-1	1
$Bi_{1-x}Sb_x$	-1	-1	+1	-1	1

Table 2.1: Topological number of Bi, Sb, and $Bi_{1-x}Sb_x$. Four time-reversal invariant momenta ($\bar{\Gamma}$, $3\times\bar{\mathrm{M}}$) are projected from eight time-reversal invariant moment (Γ, T, 3×L, 3×X) as shown in Fig. 2.7(a). Adapted from [30].

comparing Fig. 2.6 with Fig. 2.3. Later, $\delta(\mathbf{k}_i)$ is simplified as

$$\delta(\mathbf{k}_i) = \prod_{m=1}^{N} \xi_{2m}(\mathbf{k}_i) \tag{2.11}$$

in the inversion symmetric system, where $\xi_{2m}(\mathbf{k}_i)$ is the parity eigenvalues (+1 or −1) of the occupied bulk states and N is the number of degenerate states below Fermi level. With this formula, several real materials were predicted as "three-dimensional topological insulators" [30].

2.2.2 $Bi_{1-x}Sb_x$ alloy

The topological phase was predicted in real materials, including, $Bi_{1-x}Sb_x$ alloy as well as α-Sn and strained HgTe [15]. Among those materials, semiconducting (or semi-metallic) $Bi_{1-x}Sb_x$ alloy was experimentally identified as the three-dimensional topological insulator at the first [32], strained HgTe was also confirmed later [33]. Unlike bismuth, $Bi_{1-x}Sb_x$ alloy ($0.07 < x < 0.22$) shows $\nu_0 = 1$ of Z_2 topological number as arranged in Table 2.1 with bulk parity invariants. It has bulk energy gap, including band inversion of L_a and L_s at $x = 0.04$, in the Sb concentration range of 0.07 to 0.22 as shown in the energy diagram of each state (Fig. 2.7(b)) [34]. Thus this material was expected to have a quantum spin Hall state in three-dimension. As a matter of fact, an odd number of surface bands were observed with angle-resolved photoelectron spectroscopy between the bulk energy gap in $Bi_{0.9}Sb_{0.1}$ [32]. This is one of the key propertie of topological phase, at E_F between both time-reversal invariant momenta $\bar{\Gamma}$ and $\bar{\mathrm{M}}$ points.

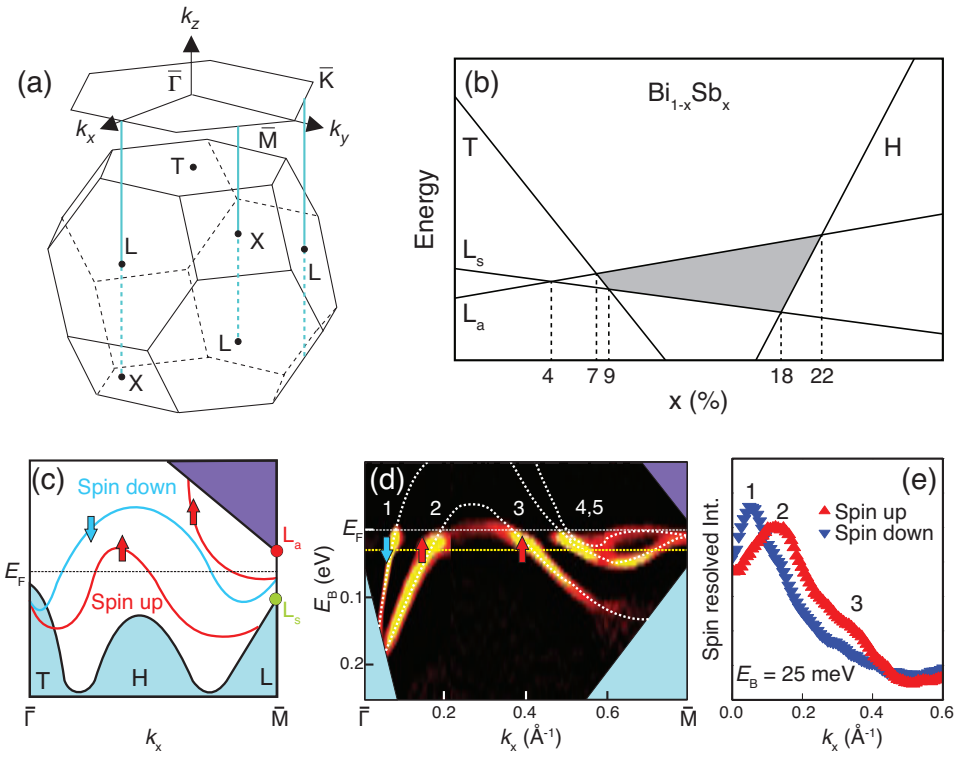

Figure 2.7: (a) The bulk Brillouin zone and its projection to the surface Brillouin zone of $Bi_{1-x}Sb_x$ crystal. (b) Energy diagram for each state of $Bi_{1-x}Sb_x$ as a function of x. The grey filled area shows the region, where is considered to be topological insulator. (c) A schematic of spin-polarized surface states dispersion, which shows "partner switching". (d) Spin-integrated photoelectron intensity image along $\bar{\Gamma} - \bar{M}$ direction. Surface bands cross the Fermi level five times. (e) Spin-resolved momentum distribution presented from the yellow dotted line in (d), $E_B = 25$ meV. Figures are adapted from [32, 34, 35].

Soon after, helically spin-polarized surface states were observed in $Bi_{1-x}Sb_x$ directly using spin- and angle-resolved photoelectron spectroscopy [35] as shown in Fig. 2.7(e). Though the spin-polarization of the fourth and fifth surface bands were not clarified, this is the first experimental evidence to be "non-trivial" topological phase due to the quantum spin Hall effect in three-dimensional matter. Later, the spin-polarization was completely accomplished [36] with high efficient spin-polarimeter using very low energy electron diffraction [37]. As mentioned in Sec. 2.1.2, these helical spin-polarized surface states are expected to be robust, so that backscattering into anti-chiral state might be prohibited due to the time-reversal symmetry. A scanning tunneling spectroscopy study showed an experimental evidence of this protection [38], of which the detail will be described in Sec. 4.1.1.

In spite of these properties as three-dimensional quantum spin Hall state, the small energy gap (only up to 30 meV) and complicated surface states motivated researchers to search for ideal topological insulators, which have a larger bulk energy gap with simple surface states.

2.2.3 Chalcogen compounds

It was simultaneous with the prediction of $Bi_{1-x}Sb_x$ alloy that Bi_2Te_3, known as thermoeletric materials [39], was also suggested for a candidate of three-dimensional topological insulator [30]. This prediction verified using theoretical calculation based on first principles by *Zhang et al.* [40]. The theoretical works demonstrated not only for Bi_2Te_3 (Fig. 2.9(d)), as well as several chalconen based compounds such as Bi_2Se_3 (Fig. 2.9(a)), Sb_2Te_3 and Sb_2Se_3. And the results revealed topological properties with only a single linearly dispersed surface band crossing the Fermi level at Γ point, so-called Dirac cone, in those materials only except Sb_2Se_3, in which no band inversion between the highest occupied band and the lowest unoccupied band was reported as shown in Table 2.2. In particular, the calculated electronic structure of Bi_2Se_3 predicted relatively a large bulk energy gap of $E_G = 300$ meV, which can be regarded as a new generation of three-dimensional topological materials.

Such a series of chalcogen compounds crystallize in tetradymite structure as shown in Fig. 2.8(b). This type of crystal structure can be classified into the rhombohedral structure with the space group $R\bar{3}m$. The crystal has a layered

Material	OB														UB	Γ
Sb_2Se_3	+	−	+	−	+	−	+	−	+	−	+	−	−	−	+	+
Sb_2Te_3	+	−	+	−	+	+	−	+	−	+	−	−	−	+	−	−
Bi_2Se_3	+	−	+	−	+	−	+	−	+	−	+	−	−	+	−	−
Bi_2Te_3	+	−	+	−	+	−	+	+	−	+	−	−	−	+	−	−

Table 2.2: The parity of each band, fourteen occupied bands (OB) and the lowest unoccupied band (UB), at the Γ point for Sb_2Se_3, Sb_2Te_3, Bi_2Se_3, Bi_2Te_3. Adapted from [40].

structure, which consists of covalently bonded five atomic layer (e.g. Se1-Bi-Se2-Bi-Se1), so-called "quintuple layer". These layers are stacked in -C-A-B-C-A-B-C- and weakly interacting with van der Waals force contrary to the strong bonding within the quintuple layer. Thus, those materials can be easily cleaved between quintuple layers that the top layer of surface consist of outer chalcogen atoms (X1).

Fig. 2.8(a) shows a three-dimensional Brillouin zone for those materials with space group $R\bar{3}m$. The four time-reversal invariant points are Γ, L, F, and Z, which are remarked in the figure. The two-dimensional Brillouin zone of the projected (111) surface is drawn as the blue hexagon with high symmetry points of $\bar{\Gamma}$, $\bar{\mathrm{K}}$ and $\bar{\mathrm{M}}$.

After the prediction of several materials for the second generation topological insulators, the topological surface states, or Dirac cone, were experimentally observed for Bi_2Se_3 [41, 43, 44], Bi_2Te_3 [42, 44], as well as Sb_2Te_3 [45] with ARPES. The spin-polarized surface states of binary bismuth chalcogenide were observed directly with spin-and angle-resolved photoelectron spectroscopy [46, 47], as well as in very similar materials Bi_2Te_2Se and Bi_2Se_2Te [48]. In particular, Bi_2Se_3 is considered as an ideal topological insulator from the following reasons. First, Bi_2Se_3 has the only a single Dirac cone-like surface state, which means basically no scattering channels exist because of the time-reversal symmetry. Second, it is stoichiometric, hence, in principle, high homogeniety is allowed rather than alloy material such as $Bi_{1-x}Sb_x$. Finally, Bi_2Se_3 has a large bulk energy gap of ~ 0.3 eV, already mentioned above.

Despite of the topological phase feature, those result unfortunately showed that not only the single surface band, but also the bulk conduction band crosses the

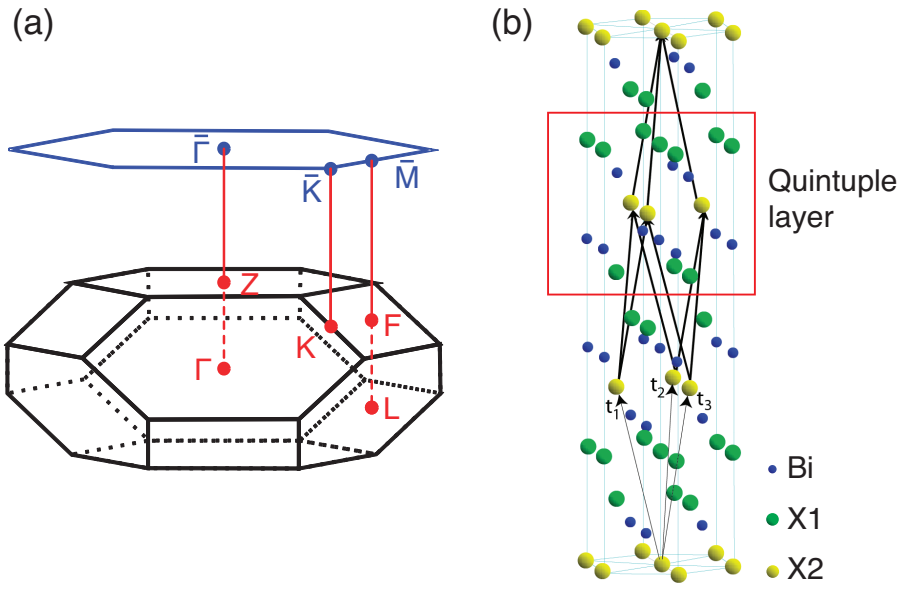

Figure 2.8: (a) Three-dimensional Brillouin zone (black) of Bi_2X_3 (X = Se, Te) and a projection to two-dimensional Brillouin zone (blue) (b) Crystal structure of same materials. A red square indicates an unit layer of X_1-Bi-X_2-Bi-X_1, so called quintuple layer. Adapted from [40].

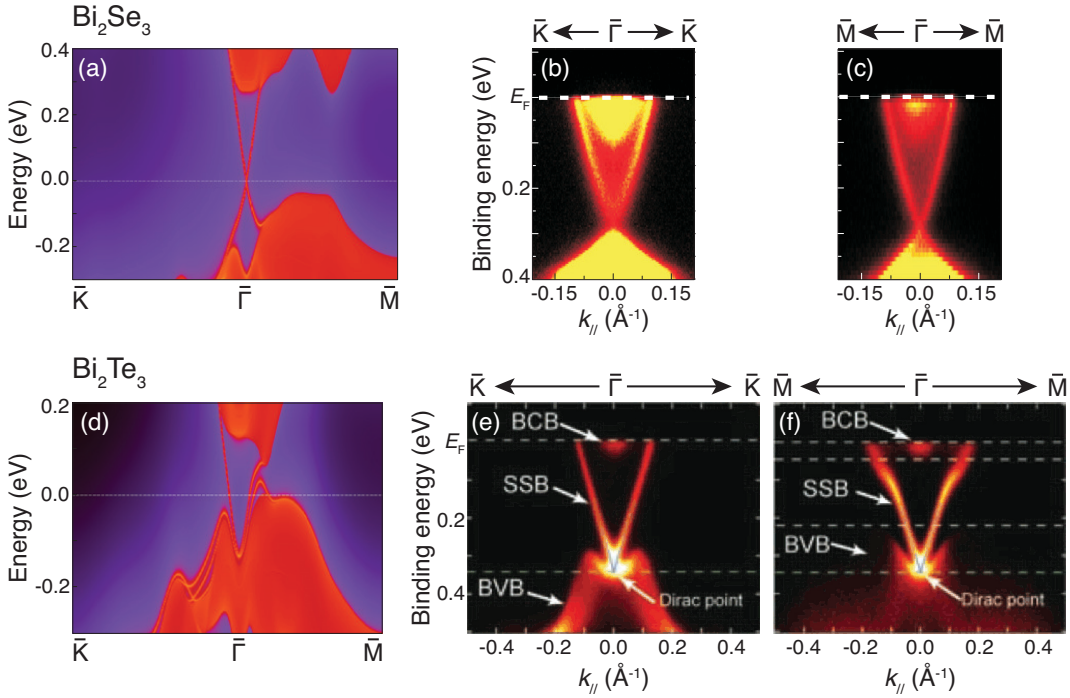

Figure 2.9: (a), (d) Energy and momentum dispersions of Bi_2Se_3 and Bi_2Te_3, respectively on the [111] surface. Comparatively larger energy gap is shown in Bi_2Se_3 ($\sim$ 0.3 eV) than Bi_2Te_3 ($\sim$ 0.1 eV), however, both have surface state between the gap. Experimentally observed band dispersions of Bi_2Se_3 along (b) $\bar{\Gamma} - \bar{K}$ and (c) $\bar{\Gamma} - \bar{M}$ directions, as well as of Bi_2Te_3 along (e) $\bar{\Gamma} - \bar{K}$ and (f) $\bar{\Gamma} - \bar{M}$ directions. ARPES results also show Dirac cone shaped surface states clearly. Figures are adapted from [40, 41, 42].

Fermi level in Bi_2Se_3 and Bi_2Te_3 as shown in Fig. 2.9, due to electron doping effect originating from chalcogen site vacancies in the as-grown samples. Thus, it is very difficult to grow an intrinsic bulk-insulating crystal. The transport property has a same problem that the surface originated property is hardly observed [49]. In contrast to the Bi_2Se_3 with Se vacancies, the surface transport property was firstly observed in Bi_2Te_3, however, the surface contribution to the transport is still very low, which did not exceed ~ 0.3 % [50]. Furthermore, a scanning tunneling spectroscopy study for Bi_2Se_3 found the scattering between the surface state and bulk continuum band [51], also supported by theoretical study [52], which can disturb the perfect transmission in this material.

Nevertheless, those materials based on the chalcogen compound, especially Bi_2Se_3, are more suitable for the detailed study than the first discovered $Bi_{1-x}Sb_x$ alloy and the further electronic property was studied. Moreover, new candidates for the topological insulators were explored among the chalcogen coumpound. As a result, several new materials, such as $TlBiSe_2$ [53, 54, 55], $PbBi_2Te_4$ [56, 57] and $GeBi_2Te_4$ [58, 59], were regarded as new topological materials from the experimental results of band structure.

Chapter 3

Experimental techniques

3.1 Scanning tunneling microscopy

Since the scanning tunneling microscope (STM) was invented by Gerd Binnig and Heinrich Rohrer in 1981[60, 61], it became one of the most powerful techniques in the surface science field. Using an atomically sharpened metal tip, surface topographic and electronic structures can be observed in the real space with very high spatial resolution[62, 63]. Due to this reason, nowadays, STM is widely used in nanoscopic surface science and plays a key role in many related field.

3.1.1 Tunneling effect

The most important variable in STM is the tunneling current, generated by electron tunneling effect. The tunneling current flows at a finite applied voltages when the tip - surface distance reaches to about 1 nm. Although electrons are not allowed to overcome a potential barrier with the energy higher than themselves in classical mechanics, quantum mechanics describes that there is a finite value of the wave functions of electrons decaying exponentially into the potential barrier. Therefore, the wave function still has a finite value even beyond the barrier, which means electrons could penetrate the barrier.

Assuming one-dimensional system with potential barrier with V_0, depict as Fig. 3.1, the Schrödinger equation gives a simple description of the tunneling probability

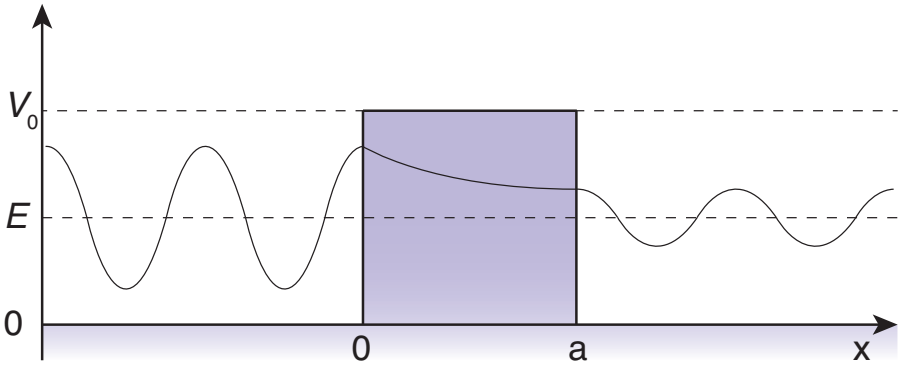

Figure 3.1: Schematic of the electron tunneling through a one-dimensional potential barrier

of electron.

$$E\psi(x) = \begin{cases} -\frac{\hbar^2}{2m}\frac{d^2\psi(x)}{d^2x} & (x < 0) \\ -\frac{\hbar^2}{2m}\frac{d^2\psi(x)}{d^2x} + V_0\psi(x) & (0 < x < a) \\ -\frac{\hbar^2}{2m}\frac{d^2\psi(x)}{d^2x} & (x > a) \end{cases} \tag{3.1}$$

where $\psi(x)$ denotes wave function of electron. General solutions of above equations are

$$\psi(x) = \begin{cases} Ae^{ikx} + Be^{-ikx} & (x < 0) \\ Fe^{-k'x} + Ge^{k'x} & (0 < x < a) \\ Ce^{ikx} & (x > a) \end{cases} \tag{3.2}$$

where

$$k = \frac{\sqrt{2mE}}{\hbar} \tag{3.3}$$

$$k' = \frac{\sqrt{2m(V_0 - E)}}{\hbar} \tag{3.4}$$

According to the boundary conditions of wave functions and their derivatives at $x = 0$ and $x = a$, the transmission probability can be obtained as

$$T = \left[1 + \frac{4k^2k'^2}{(k^2 + k'^2)^2}\sinh^2 k'a\right]^{-1} \tag{3.5}$$

In the geometry of STM, $e^{-k'a} \ll 1$, Eq. 3.5 can be approximated to

$$T \simeq \frac{16k^2k'^2}{(k^2 + k'^2)^2}e^{-2k'a} \tag{3.6}$$

As described in Eq. 3.6, the transmission probability depends on the barrier width, thus T decays rapidly when the width of the barrier increases.

3.1.2 Tunneling current

Even though above description about the tunneling effect might be rough, it does represent the key point of STM. Considering an atomically sharp, ideally, with a single atom at its apex, conducting tip is placed a nanometer far from the sample surface, a tunneling current arises with applied electric potential between the tip and the sample. The current is proportional to the transmission coefficient, thus, it strongly depends on the distance of tip - sample. For a metallic sample, k' will be about 1 Å^{-1} that only a few angstrom change of the distance can make a significant response on tunneling current. When the tip scans along the sample surface even the sub-angstrom changes of surface topography provide a considerable change in the current. Usually an experiment is performed with a constant current mode, the change of the current is compensated immediately by controlling the tip height. Therefore, one can observe the sample topography as a reflection of the tip position even with atomic resolution.

The simple model of the tunneling effect with the one-dimensional system is useful to describe the basic phenomenon related to STM. However, this model is insufficient to explain the STM experiments. One need a more accurate theory, and such a precise treatment of tunneling was performed by Bardeen [64]. Assuming a potential V is applied between two electrodes, the tunneling current between two electrodes can be given as

$$I = \frac{2\pi e}{\hbar} \sum_{\mu\nu} f(E_\mu)[1 - f(E_\nu + eV))]|M_{\mu\nu}|^2 \delta(E_\mu - E_\nu - eV) \tag{3.7}$$

where $f(E)$ is the Fermi distribution function and μ, ν are the states of those electrodes. Thus an electron from the state μ with energy E_μ can tunnel to the other state ν, with a probability given by the transmission efficiency $|M_{\mu\nu}|^2$. Bardeen has shown the tunneling matrix element $M_{\mu\nu}$ as

$$M_{\mu\nu} = \frac{\hbar^2}{2m} \int (\psi_\mu^* \nabla \psi_\nu + \psi_\nu^* \nabla \psi_\mu) d\mathbf{S} \tag{3.8}$$

where ψ_μ and ψ_ν are the wave functions of the corresponding states without tunneling. In the STM, which indicate the states of the tip and the sample. For a

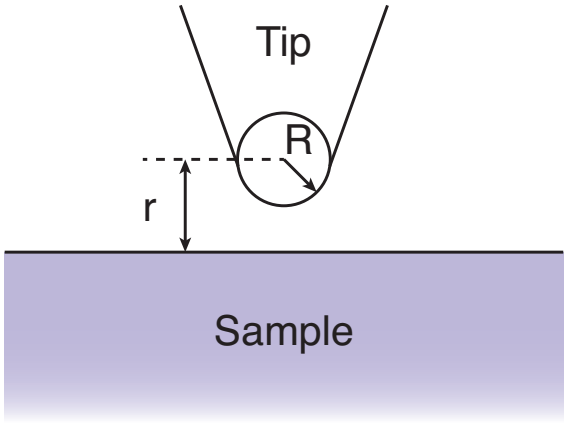

Figure 3.2: A schematic of the STM geometry between the tip and the sample. The tip apex is supposed as locally spherical with a radius R.

further evaluation of $M_{\mu\nu}$, hereafter, a fixed electrode geometry is essential that one can consider the geometry as depict in Fig. 3.2. This was first applied for STM by Tersoff and Hermann [65]. According to their model, the tunneling current can be calculated under the limit of small voltage and low temperature as

$$I \propto \rho_\mu(E_F)\rho_\nu(\mathbf{r}, E_F)V\phi^4 e^{2R\sqrt{2m\phi}/\hbar} \tag{3.9}$$

for a locally spherical tip with a radius R. In the case of STM, $\rho_\mu(E_F)$ is the tip density of states at Fermi level, $\rho_\nu(\mathbf{r}, E_F)$ is the local density of state of the sample at the center of tip position, and ϕ is the work function. ρ_ν can be written as

$$\rho_\nu(\mathbf{r}, E) = \rho_\nu(E)T(E, V, r) \tag{3.10}$$

with the transmission coefficient $T(E, V, r_0)$, which depends on the properties of the tunneling barrier.

With the larger bias voltage, the current described in Eq. (3.3) should be considered over all of contributing states and be integrated, thus the current I can be written as

$$I \propto V \int_o^{eV} \rho_\mu(E_F - eV + E)\rho_\nu(E_F + E)T(E, V, r)dE \tag{3.11}$$

where E is the tunneling electron energy relative to E_F. From Eq. (3.11), one can notice that the tunneling current represents the sample local density of states

rather than the structural properties. In other word, the tip density of state can also affect to the tunneling current significantly. Thus, materials with a flat density of state near the E_F, such as tungsten, generally used for the tip.

3.1.3 Scanning tunneling spectroscopy and dI/dV map

The tunneling current depends on not only the topography of the sample surface, but also the local density of state as described above. This property allows to measure the electronic states of the sample with STM. According to the Tersoff-Hamann model, the tunneling current is understood as the integration of local density of state for all contributing bias voltage. Thus, the first derivative of the current indicates local density of state, which can be calculated as

$$\begin{aligned}
\frac{dI}{dV} &\propto \frac{d}{dV}\int_0^{eV} \rho_t(E_F + E - eV)\rho_s(E_F + E)T(E, V, r)dE \\
&= \rho_t(E_F)\rho_s(E_F + eV)T(eV, V, r) \\
&\quad + \int_0^{eV} \frac{d}{dV}\rho_t(E_F + E - eV)\rho_s(E_F + E)T(E, V, r)dE \\
&\quad + \int_0^{eV} \rho_t(E_F + E - eV)\rho_s(E_F + E)\frac{d}{dV}T(E, V, r)dE \qquad (3.12)
\end{aligned}$$

where ρ_μ and ρ_ν are substituted by ρ_t and ρ_s from Eq. (3.11), respectively. Generally, $\rho_t(E)$ and T(E, V, r) have no significant change near the Fermi level compared to $\rho_s(E)$. Therefore, one can ignore the last two terms in Eq. (3.12), and the local density of state is given by the first derivative of the tunneling current.

$$\frac{dI}{dV} \propto \rho_s(E_F + eV) \qquad (3.13)$$

Normally, in the STM experiment, the lock-in amplifier is used to provide periodic modulation for getting differential conductance (dI/dV). If the bias voltage is fixed during the scanning with modulations, one can observe the spatial distribution of the local density of states, so called dI/dV image of same bias. Thus, STM is widely used not only to observe the topological features of the surface, but also to clarify the local electronic properties of the materials.

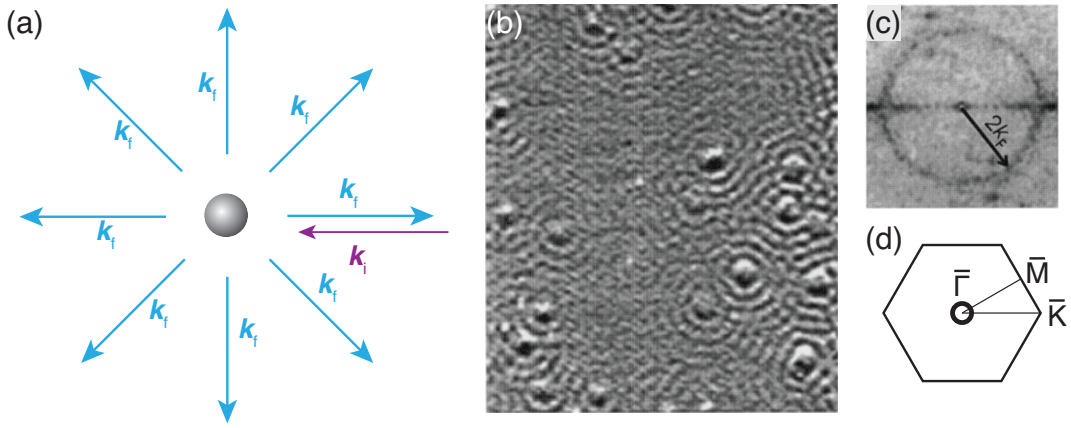

Figure 3.3: (a) A schematic drawn electron scattering at an impurity. The initial state $\mathbf{k}_i$ is scattered to the final states $\mathbf{k}_f$. (b) Constant current topography of Cu(111) surface. The bias voltage (V_B) is -5 mV and $T = 150$ K. Complex pattern of circular standing waves due to point defects. (c) Two-dimensional Fourier transformed image of (b). (d) Surface Brillouin zone of Cu(111) with Fermi contour of surface state. Adapted from [68].

3.1.4 Electron standing wave and quasiparticle interference

The differential conductance image allows to focus the localized surface electronic states. Using this technique, the electron standing waves were observed with STM on the clean surface of Cu(111) [66] and Au(111) [67]. On the clean surface of both single crystals, electrons behavior as two-dimensional free electron gas. Thereby, an impurity or a crystal defect can cause the electron scattering, also at the step edge. Due to the wave-particle duality, electrons can interfere with the scattered one. The interferences appear as the spatial modulations on the surface, the electron standing waves.

Moreover, energy dispersion of spin degenerate system even in the momentum space can be provided by the observed electron standing waves. Assuming the elastic scattering, electrons can be scattered into the constant energy contour of dispersion with opposite momentum $-\mathbf{k}$. The length of the scattering vector q is equal to $q = |-k-k| = 2k$ accordingly to the scattering vector $\mathbf{q}$ as following equation.

$$\mathbf{q} = \mathbf{k_f} - \mathbf{k_i} \tag{3.14}$$

Thus, Fourier transformed periodicity of the standing waves correspond to $2k$ in

the momentum space, that the energy dispersion can be clarified. This is well appeared in Figs. 3.3(b) and 3.3(c). Electron standing waves on the clean surface of Cu(111) are found in the Fig. 3.3(b), and Fig. 3.3(c) shows the corresponding Fourier transformed image. The circular constant energy contour corresponds to the Shokley state of the Cu as described in Fig. 3.3(d) with surface Brillouin zone. The operating system of the STM with high stability at very low temperature, this technique is used to understand electronic structure of various solid material, such as high-T_c superconductors [69].

3.2 Photoelectron spectroscopy

Photoelectron spectroscopy is experimental technique extensively used in order to study electronic structures of solid materials. The basic principle of photoelectron spectroscopy is photoelectric effect, which had been first observed by Heinrich Hertz, and had explained by Albert Einstein with introducing the quantum nature of light, now so-called photons.

3.2.1 Photoemission process

In the process of photoelectric effect, electrons, given enough energy over the work function ϕ, could be emitted with kinetic energy E_k. From the energy conservation law, the kinetic energy of emitted electrons can be written as

$$E_k = h\nu - \phi - E_B \tag{3.15}$$

where $h\nu$ is energy of photons, and E_B is binding energy of electrons in the materials. For the interpretation of the photoemission experiment, a three-step model is useful. The basis of this model is shown in Fig. 3.4.

(1) Photoexcitation of the electrons

In the first step, locally the photon is absorbed and an electron is excited. Assuming a small perturbation by photoemission as H', the transition probability w per unit time between an initial state ψ_i and a final state ψ_f is calculated as

$$w \propto |\langle \psi_f | H' | \psi_i \rangle|^2 \delta(E_f - E_i - h\nu) \tag{3.16}$$

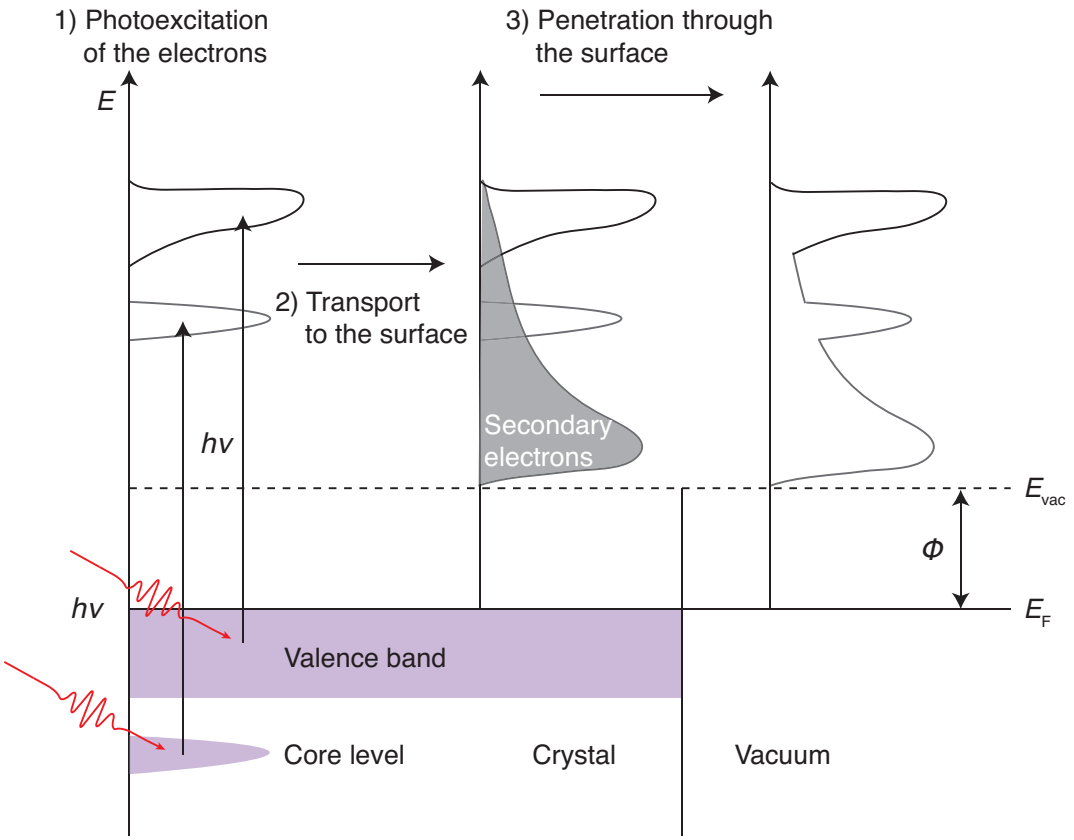

Figure 3.4: Three step model for photoemission process. (i) Photoexcitation of electrons (ii) Travel through the bulk to the surface (iii) Penetration through the surface and detection. Adapted from [70].

by Fermi's Golden Rule. Here, Hamiltonian of perturbation H' can be written as

$$H' = \frac{e}{2mc}(\mathbf{A}\cdot\mathbf{p} + \mathbf{p}\cdot\mathbf{A}) + \frac{e^2}{2mc^2}|\mathbf{A}|^2 \tag{3.17}$$

where $\mathbf{A}$ is the vector potential of electromagnetic field and $\mathbf{p}$ is the momentum operator of electrons. Neglecting the term of higher degree $|\mathbf{A}|^2$, H' can be approximated as

$$H' = \frac{e}{mc}\mathbf{A}\cdot\mathbf{p} \tag{3.18}$$

because $\nabla\cdot\mathbf{A}$ becomes 0 in the solid. Thus, the transition probability w can be written as

$$w \propto |\langle\psi_f|\mathbf{A}\cdot\mathbf{p}|\psi_i\rangle|^2\delta(E_f - E_i - h\nu) \tag{3.19}$$

In PES, energy range of photons is from several eV to several keV that its wavelength is enough large to neglect the spatial change of $\mathbf{A}$. Thus, finally, w can be described as

$$w \propto |\mathbf{A}_0\langle\psi_f|\mathbf{p}|\psi_i\rangle|^2\delta(E_f - E_i - h\nu) \tag{3.20}$$

(2) Travel to the surface

In the second step, the photoexcited electron travels to the surface. During this process, electrons lose energy due to electron-electron and electron-phonon interactions and give rise to secondary electrons as shown in Fig. 3.4. This inelastic scattering process can be estimated by using electron mean free path $\lambda(E_f)$. The probability of traveling to the sample surface without inelastic scattering $D(E_f,\omega)$ can be written as

$$D(E_f,\omega) \sim \alpha(\omega)\lambda(E_{fin}) \tag{3.21}$$

in the wavelength of vacuum ultra-violet (VUV) region, because of $\alpha,\lambda \ll 1$, where $\alpha(\omega)$ is the extinction coefficient of light absorption. As shown in Fig. 3.5, electron mean free path has an universal behavior among various materials. From this figure, we can also notice PES is very surface sensitive.

(3) Penetration through the surface

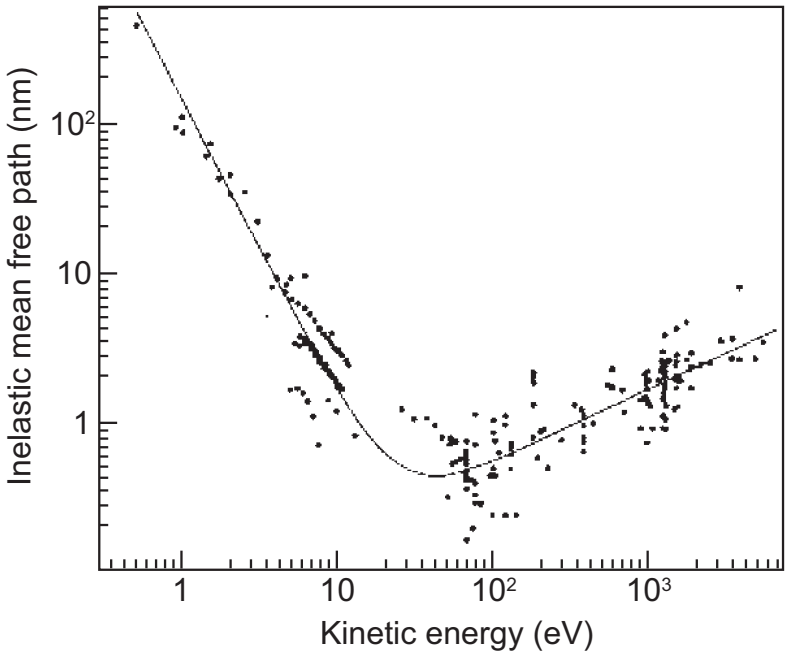

Figure 3.5: The universal curve, showing inelastic mean free path of photoelectron. Adapted from [71].

In the final step, the electrons penetrate through the surface and escape from the surface into the vacuum. This process is usually described by electrons overcoming a potential barrier, called inner potential (V_0), at the surface. Assuming the momentum in solid $\mathbf{k}$, following relations should be brought into existence to escape from the surface to vacuum.

$$V_0 < \frac{|\hbar \mathbf{k}_\perp|^2}{2m} \tag{3.22}$$

Thus, the probability of electron escape $T(E_f, \mathbf{k})$ is can be defined as $T(E_f, \mathbf{k}) = 1$ when

$$|\mathbf{k}_\perp| > \sqrt{2mV_0}/\hbar \tag{3.23}$$

with $E_f > \phi$, or 0. Therefore, the number of photoelectrons by photon injection can be written as

$$N(E_k, h\nu) \propto \sum \int d^3\mathbf{k}\{|\mathbf{A}_0\langle\psi_f|\mathbf{p}|\psi_i\rangle|^2 D(E_f, \omega)T(E_f, \mathbf{k})\}\delta(E_f - E_i - h\nu)\delta(E_k - (E_f - \phi)) \tag{3.24}$$

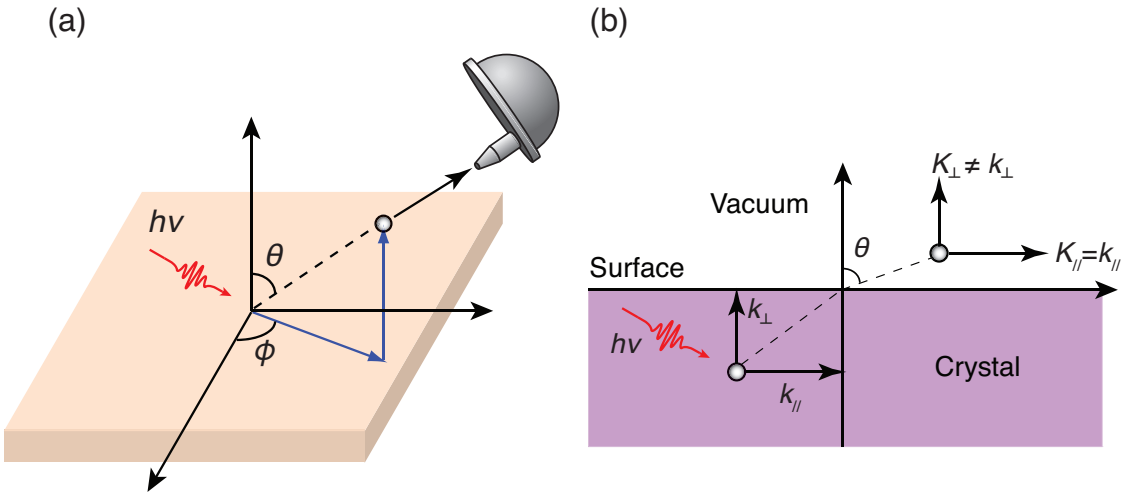

Figure 3.6: (a) A schematic of ARPES measurement (b) Relation of momentum during the electron escape. A perpendicular component would not be conserved, in contrast to a parallel component is conserved even after escape from the sample surface.

There is also one-step model, which treats the whole process described above (three-step model) as one step. However it can be shown that both models give the same results in analyzing the photoemission spectra[70].

3.2.2 Angle-resolved photoelectron spectroscopy

Angle-resolved photoemission spectroscopy (ARPES) is a type of photoelectron spectroscopy to study the electronic structure of solid matter. Since ARPES is the only experimental technique to determine the electron band structure directly, it is one of the most important methods to study energy dispersion of the valence band of materials. In ARPES, parallel component wave vector ($K_\parallel$) to the surface is conserved during the photoemission to the vacuum as electron energy as mentioned above. Thus, two-dimensional band dispersion between energy and wave vector can be determined as following relation.

$$K_\parallel = \sqrt{\frac{2mE_k}{\hbar^2}} \sin\theta = k_\parallel \tag{3.25}$$

Where k is wave vector before electron transmission to the surface, and m is the mass of an free electron. So, we can obtain the 2D band dispersion by rotating the emission angle (θ). Meanwhile, wave vector component, perpendicular to the surface, is not conserved, because of the potential barrier between solid and vacuum. Therefore, $K_\perp$ can be described as followed.

$$K_\perp = \sqrt{\frac{2m}{\hbar^2}(E_k + V_0)} \tag{3.26}$$

Here, if one uses synchrotron radiation, it is possible to inject the variable energy of photons. Thus, we can obtain E-$K_\perp$ dispersion, and also determine the value of inner potential (V_0) for each material. Fig. 3.6 shows schematic drawing of ARPES measurement and the relation of wave vector in photoemission process from the solid to the vacuum as mentioned above.

3.2.3 Time- and angle-resolved photoelectron spectroscopy

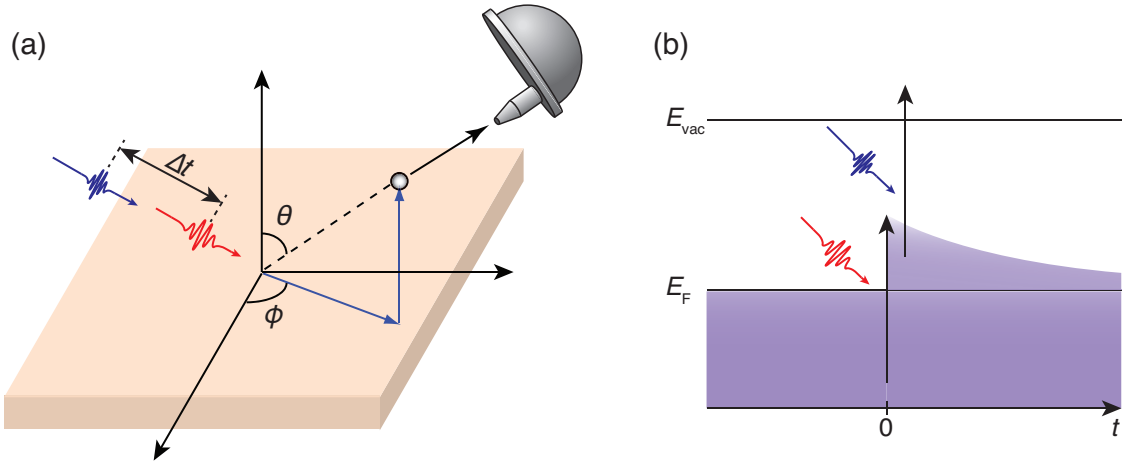

Figure 3.7: (a) A schematic of TrARPES measurement (b) A simple energy diagram of time-resolved photoelectron spectroscopy. A red wave indicates a pump pulse and a blue wave indicates a probe pulse in both figures.

An ultrafast pump-and-probe method of ARPES with pulsed laser source lets us possible to observe time dependent electronic structures [72]. One pulse (pump) raises dynamics in the matter and the other pulse probes the non-equilibrium

electronic state as snapshots. The difference of the optical path length between the pump and probe pulses causes the different arrival time, so-called delay time. Thus, one can observe the recovery from the impact, by varying the optical path as described in Fig. 3.7(b). This is a basic principle of time-resolved photoelectron spectroscopy. If the information of angle is added as shown in Fig. 3.7(a), one can get snapshots of non-equilibrated energy-momentum distribution with time- and angle-resolved photoelectron spectroscopy (TrARPES). In order to vary the delay time, the optical path of pump pulse is controlled usually.

Fig. 3.8 shows an example of the practical experimental set up for TrARPES with a hemispherical analyzer [73, 74], which was used for the present study. A laser pulse from Ti:sapphire photon source is split into two different pulses of pump and probe. Black ticks indicate mirrors that both optical paths of pump and probe are controlled. Especially, the optical path of pump pulse includes a movable delay stage, that one can vary the delay time between two pulses.

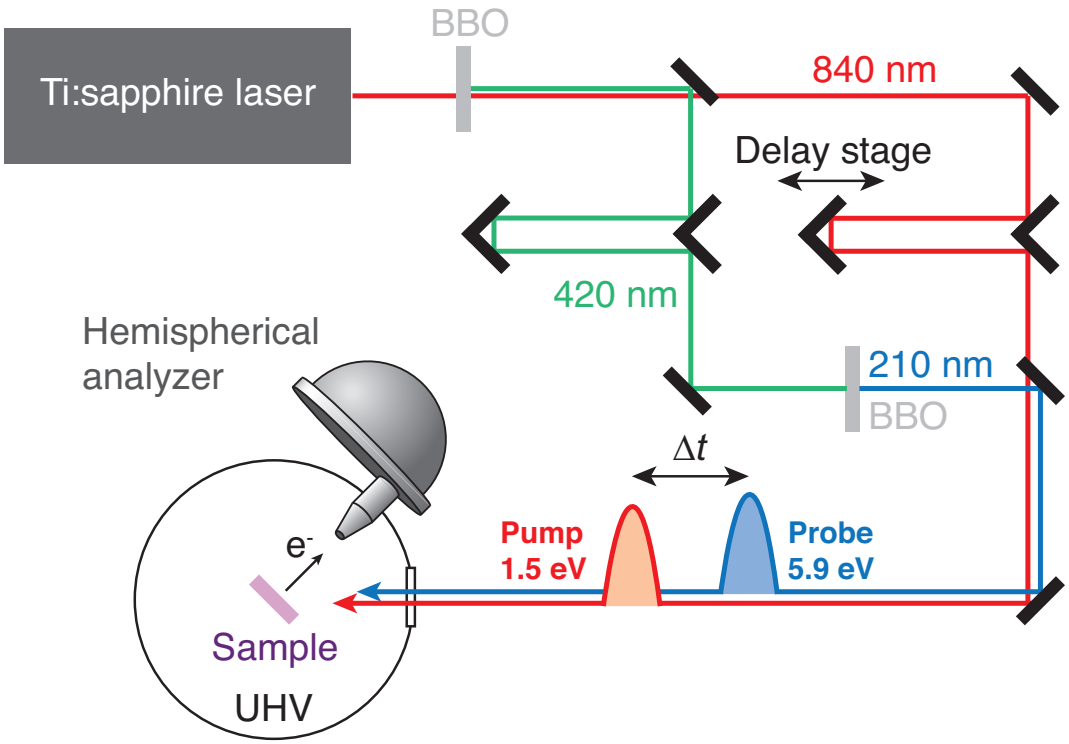

Figure 3.8: A schematic of the TrARPES system with a hemispherical analyzer. The photon source is Ti:sapphire laser. The optical path of pump pulse includes a movable delay stage. Black ticks are mirrors to reflect laser.

Chapter 4

Angle dependent suppression of electron backscattering in the topological insulator

4.1 Introduction

4.1.1 Electron backscattering in the topological insulator

Three-dimensional topological insulators are accompanied by metallic surface states due to a Z_2 topology of the bulk wave function as mentioned in Chapter 2. Such a peculiar topological surface state is spin-polarized with helical texture, which is expected to lead to a suppression of electron scattering due to mismatch of spin between the eigenstates before and after the scattering. Especially, the perfect backscattering of 180° is expected to be absent, because of the time-reversal symmetry. A scanning tunneling microscopy and spectroscopy study of $Bi_{1-x}Sb_x$ alloy demonstrated this interesting expectation experimentally first [38]. The protected backscattering was proven by the measurement of quasi-particle interference due to the electron scattering. Quasi-particle interference pattern, appeared in Fourier transformed differential conductance image of Fig. 4.1(a), was compared with two different intensity patterns, the joint density of states (JDOS)

$$\mathrm{JDOS}(\mathbf{q}) = \int I(\mathbf{k})I(\mathbf{k}+\mathbf{q})d^2\mathbf{k} \tag{4.1}$$

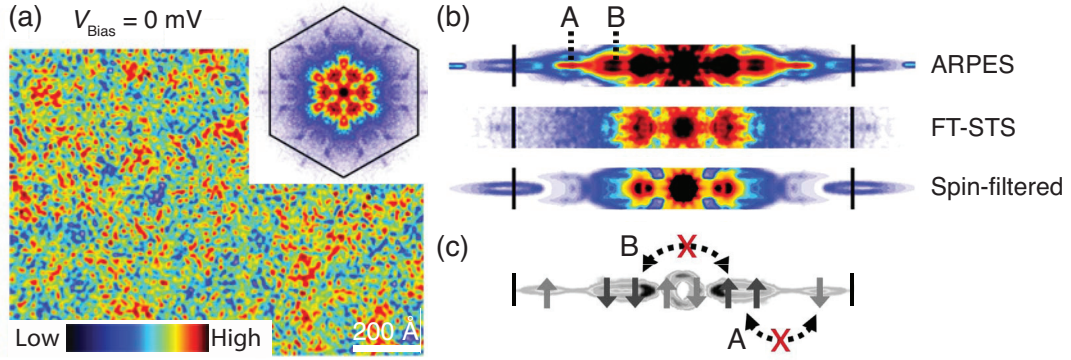

Figure 4.1: (a) dI/dV image at $V_B = 0$ mV and Fourier transformed amplitude image (*inset*) of $Bi_{0.92}Sb_{0.08}$. (b) Calculated intensity of the inner product from the ARPES measurement of $Bi_{0.91}Sb_{0.09}$ [35] without spin (top) and spin filtered one (bottom). Fourier transformed dI/dV image at the same energy shown in the middle. All images are cut along $\bar{\Gamma}$-$\bar{M}$ direction. (c) A schematic of prohibited backscattering channels, which depend on spin chirality. Adapted from [38].

and spin-dependent scattering probability (SSP)

$$\mathrm{SSP}(\mathbf{q}) = \int I(\mathbf{k})T(\mathbf{q},\mathbf{k})I(\mathbf{k}+\mathbf{q})d^2\mathbf{k} \tag{4.2}$$

as shown in Fig. 4.1(b), where $I(\mathbf{k})$ is ARPES intensity proportional to the surface states' density of states and $T(\mathbf{q},\mathbf{k}) = |\langle\sigma(\mathbf{k})|\sigma(\mathbf{k}+\mathbf{q})\rangle|$. Namely, JDOS and SSP are computed value from the Fermi surface observed by ARPES [35] with and without a backscattering of $\mathbf{k}$ to $-\mathbf{k}$, because spin directions are opposite at $\mathbf{k}$ and $-\mathbf{k}$. In the Fourier transformed dI/dV image, one can realize the intensity corresponding to scattering channels as drawn in Fig. 4.1(c) suppressed that it means backscattering is inhibited in $Bi_{1-x}Sb_x$. However, strong interference is still observed due to multiple surface band, some of which have the same spin orientation.

Similarly, the quasi-particle interference measured in Bi_2Se_3 [75], as well as in impurity doped Bi_2Te_3 [76, 77, 78, 79] and Bi_2Se_3 [79], which have only a single Dirac-cone surface state. As a result, no interference was detected at energies away from unless the Dirac cone is significantly warped [42, 80], owing to the cubic spin-orbit coupling term proportional to $k^3\sigma_z$ [81]. The quasi-particle interference in the warped Dirac cone is also predicted by theoretical study [82].

In these previous experiments, the suppression due to the helical spin texture of the topological surface state was only elucidated qualitatively, because no interference was observed for circular constant-energy contours of surface state in Bi_2Se_3 and Bi_2Te_3. In other words, it is still not understood what extent the backscattering is suppressed as a function of scattering angle within the same surface band, of which constant-energy contour is not warped. Even such information is crucial to understand the transport in the topological surface state, no material allows to observe interference in an unwarped Dirac cone.

4.1.2 3D topological insulator $Bi_{2-x}Sb_xTe_{3-y}Se_y$

Bi_2Te_2Se has been paid attention due to high surface contribution to the transport [83], about 20 times larger than Bi_2Te_3 [50]. $Bi_{2-x}Sb_xTe_{3-y}Se_y$ is the first topological insulator material, which has similar surface dominant transport with nonmetallic bulk single crystal [84]. Fig. 4.2 shows structural and electronic properties of $Bi_{2-x}Sb_xTe_{3-y}Se_y$ at several combinations of (x, y). Hereafter, all compositions of $Bi_{2-x}Sb_xTe_{3-y}Se_y$ with rhombohedral structure will be discussed, marked with white circle in Fig. 4.2(a). In case of $x = 0, y = 1$, Bi_2Te_2Se, it naturally crystallize in a chalcogen-ordered structure as with quintuple layer of Te-Bi-Se-Bi-Te as a unit layer, where X_1 = Te and X_2 = Se in Fig. 2.8(b). This is identical with other chalcogen based materials as already mentioned above. When x and y increase, Bi and outer Te layers will be mixing layers of Bi/Sb and Te/Se. The most remarkable feature of the series of this material is tunable Fermi level. The Fermi energy E_F of the crystal can be controlled by changing the composition along particular combinations of x and y in the bulk band gap [85]. This is similar to $(Bi, Sb)_2Se_3$ [86], but the position depends on x and y. Fig. 4.2(c)-(f) show the in-plane band dispersions in a series of $Bi_{2-x}Sb_xTe_{3-y}Se_y$ for four different x, y compositions, $x = 0, 0.25, 0.5$ and 1.0 where $y = 1, 1.15, 1.3$ and 2.0. Such a tuning of the topological surface carrier properties permits us Dirac cone engineering, for example, p-n junction of the topological surface state.

All of those materials have their Fermi level in the bulk energy gap as shown in Fig. 4.2(c)-(f), and the bulk is an insulator [85]. Fig. 4.2(b) shows temperature dependence of the resistance for a series of $Bi_{2-x}Sb_xTe_{3-y}Se_y$ [87]. The resistance increases in all composition with decreasing temperature, which indicates its bulk-

4. ANGLE DEPENDENT SUPPRESSION OF ELECTRON BACKSCATTERING IN THE TOPOLOGICAL INSULATOR

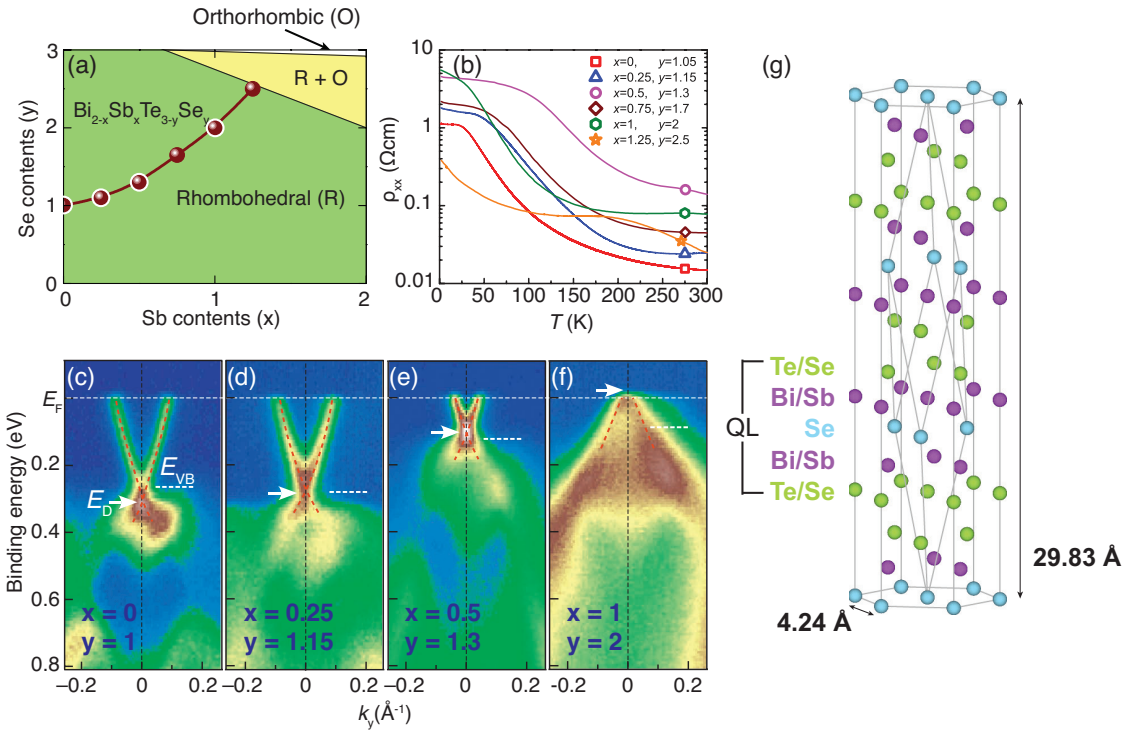

Figure 4.2: Structural and electronic property of $Bi_{2-x}Sb_xTe_{3-y}Se_y$. (a) Structure diagram and (b) temperature dependences of ρ_{xx} for several optimized compositions of $Bi_{2-x}Sb_xTe_{3-y}Se_y$ series, reproduced from [87]. (c)-(f) Band dispersions in $Bi_{2-x}Sb_xTe_{3-y}Se_y$ for four different x, y compositions, enclosed by white circles in (a), $x = 0, 0.25, 0.5$ and 1.0 where $y = 1, 1.15, 1.3$ and 2, respectively. White arrows and white dotted lines, drawn in (c)-(f), indicate Dirac point energy E_D and the energy of the valence band maximum. All band dispersions are adapted from [85]. (g) Crystal structure of $Bi_{1.5}Sb_{0.5}Te_{1.7}Se_{1.3}$, adapted from [88]. Lattice distance of a- and c-axis are 4.24Å and 29.83Å, respectively [87].

insulating property. In particular, $Bi_{1.5}Sb_{0.5}Te_{1.7}Se_{1.3}$ shows the highest resistance, which can be considered to be a bulk insulator. As well as, its band dispersion shows that the Dirac point is quite close to Fermi level, or just below E_F, thus, it can be a good candidate for an ideal three-dimensional topological insulator. The Alloy property of crystal structure might allow the observable quasi-particle interference, therefore, $Bi_{2-x}Sb_xTe_{3-y}Se_y$ offers a promising platform for quantitative understanding of the suppression of backscattering in an ideal Dirac cone.

4.2 Experiment

The single crystals of $Bi_{1.5}Sb_{0.5}Te_{1.7}Se_{1.3}$ were grown by melting stoichiometric of mixtures of high-purity elements in sealed quartz tubes[87] and the quality of single crystal was confirmed by x-ray diffraction. It will be shown later, clearly atomic resolved topography of the surface with STM and very sharp spectra with TrARPES measurement are also verifying the quality of the crystal. Experiments using STM and TrARPES were performed in two separated ultrahigh vacuum (UHV) systems.

Figs. 4.3(a) and 4.3(b) show the pictures of sample set up for each STM and TrARPES experiment, respectively. In both experiments, clean surface was prepared by cleaving with scotch tape as shown in Fig. 4.3. After cleaving the crystal in UHV with the pressure below 2×10^{-8} Pa at room temperature, the sample was transferred *in situ* in UHV either to the cooled stage in the STM chamber or to the TrARPES chamber.

The STM topography and tunneling spectra were taken at 5 K using a cryogenic STM with and electrochemically etched tungsten tip. The tip apex and its metallic density of states were checked by scanning a clean platinum surface. Topographic images were obtained using a constant current mode. For the study of quasi-particle interference, dI/dV spectroscopy was performed using a standard lock-in technique with a bias voltage modulation of 5 and(or) 10 mV at 496 Hz. The dI/dV curve was measured at every point of a 256×256 grid on the surface. The obtained data were plotted as function of position to make a dI/dV map. The constant energy dI/dV maps were Fourier transformed, and the peaks due to the surface lattice were used for the calibration of the wave vector space. The Fourier transformed patterns were symmetrized with respect to the sixfold symmetry, on the basis of

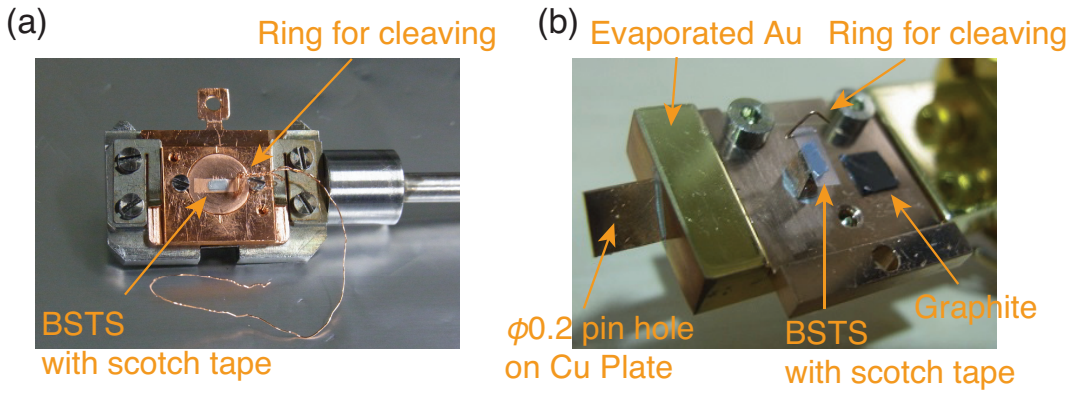

Figure 4.3: Pictures of the set up for sample cleaving in (a) the STM system and (b) the TrARPES system. Adapted from [73].

the C_{3v} symmetry of the cleaved surface.

For the TrARPES experiments, 1.5 eV (pump) and 5.9 eV (probe) pulsed photons from an amplified Ti:sapphire laser system with repetition rate of 250 kHz [73, 74] were used. The spot diameters were $\sim$ 0.4 and $\sim$ 0.2 mm for the 1.5 and 5.9 eV photons, respectively. Those diameters were estimated by the pin hole represented in Fig. 4.3(b). The pulse width was 170 ps for the pump and 250 ps for the probe, which was calculated from the total time resolution. A graphite shown in Fig. 4.3(b) was used to calibrate the total time resolution, and the detail will be described in Sec. 5.2. The time delay between the pump and the probe pulses was optimized to clarify the unoccupied TSS band in the bulk band gap [89]. Photoelectrons from the cleaved surface cooled at 5 K were detected by a hemispherical analyzer. The energy resolution of the photoelectrons was 15 meV and the pump power was fixed to 70 mW.

4.3 Results and discussions

4.3.1 Topography and tunneling spectrum

Fig. 4.4(a) shows a STM topography of cleaved $Bi_{1.5}Sb_{0.5}Te_{1.7}Se_{1.3}$ surface for a wide range. An atomically resolved topography is shown in Fig. 4.4(b). Atoms of the top Te/Se layer are visible as precise protrusions and the density of surface point defects is less than 3 %. In this magnified image, surface atoms are recognized

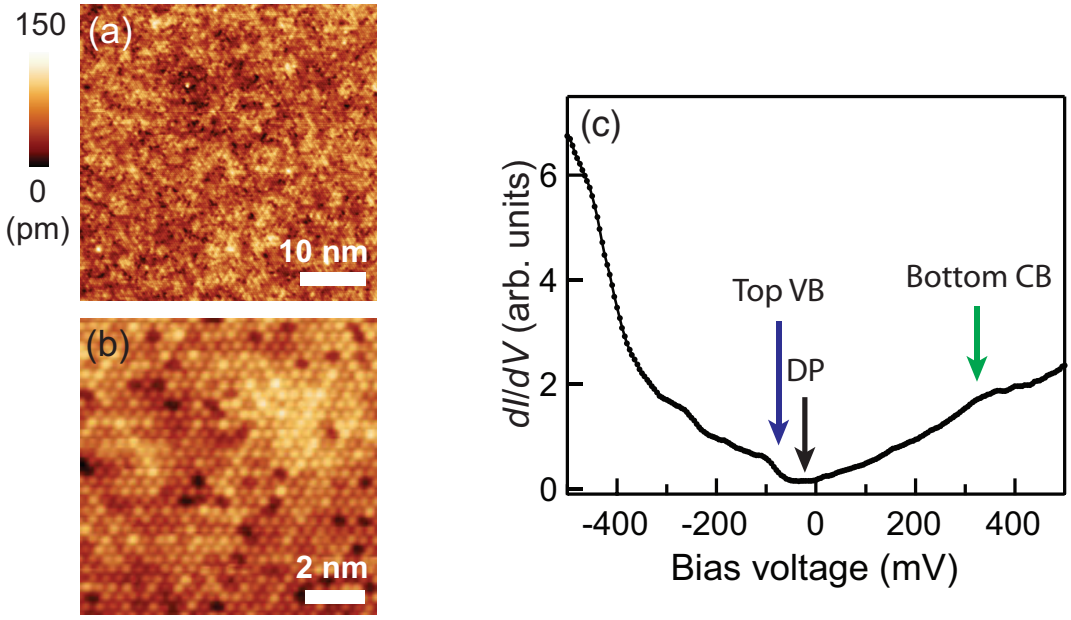

Figure 4.4: (a) Topography of cleaved $Bi_{1.5}Sb_{0.5}Te_{1.7}Se_{1.3}$ with 45 × 45 nm^2. (b) An atomically resolved STM image of $Bi_{1.5}Sb_{0.5}Te_{1.7}Se_{1.3}$. V_B and tunneling current were set to -0.4 V and 20 pA for (a), and -0.6 V and 100 pA for (b) (c) A typical tunneling spectrum of $Bi_{1.5}Sb_{0.5}Te_{1.7}Se_{1.3}$. The tunneling current was set to 200 pA at V_B = 0.5 V. Each arrow with blue, black, and green is corresponding to top of valence band, Dirac point, and bottom of conduction band, respectively. Adapted from [88].

with a distribution of the apparent height. The local density of states fluctuates because of the inhomogeneous distributions of Te and Se, as well as those of Bi and Sb in the crystal as shown in Fig. 4.2(g). Thus, the observed distribution of the height is attributed to the electronic effect due to the alloying in the Te/Se and Bi/Sb layers.

A typical point tunneling spectrum is shown in Fig. 4.4(c). The energy of Dirac point (E_D) can be defined as the minimum in dI/dV[79] where is indicated by black arrow. The differential conductance rapidly increases below E_D compared to that above E_D. This is because the top of the bulk valence band, which can be recognized as a shoulder in the dI/dV curve in Fig. 4.4(c), is located just below E_D (blue arrow). The bottom of the bulk conduction band is also visible (green arrow), corresponding to the TrARPES result, which will be shown in Fig. 4.8(b),

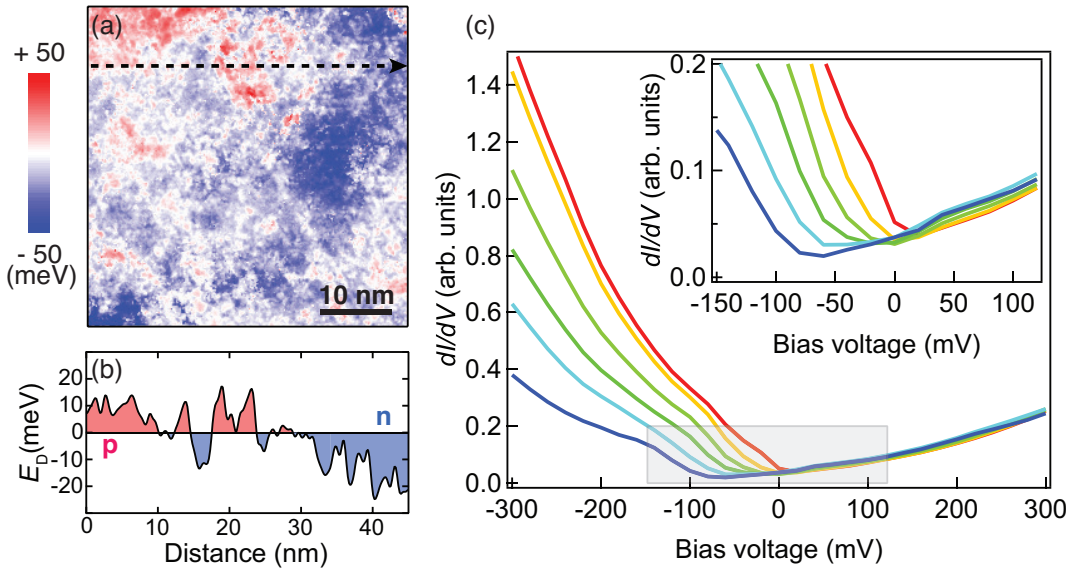

Figure 4.5: (a) Spatial variation of local Dirac point and (b) line profile of the energy variation along the black dotted arrow on (a). (c) The blue (red) curve shows the average of all dI/dV curves with E_D between -70 meV and -50 meV (20 meV and 40 meV) averaged over all points exhibiting given energy of Dirac point in (a) and *inset* shows zoomed in one of gray area. Adapted from [88].

even it is not very clear.

The energy of E_D, obtained from the minimum of dI/dV curves varies over the surface as shown in Fig. 4.5(a). Blue (red) areas depict in the image correspond to the n-type (p-type) region where E_D is below (above) the Fermi level. This is due to spatial fluctuation of the element composition. The line profile of E_D distribution map along black dotted arrow is shown in Fig. 4.5(b). Interestingly, each n-type and p-type area has a spatial extent of the order of 10 nm that indicates such a local p-n junction. E_D is distributed within tens of meV energy range and the average location of E_D is 10 ± 15 meV below Fermi level. The dI/dV curves averaged over all points with E_D in energy range of every 20 meV is plotted in Fig. 4.5(c).

4.3.2 dI/dV images and quasiparticle interferences

Figs. 4.6(a)-(d) show differential conductance maps of the cleaved sample surface for several selected values of V_B, which correspond to the energy in the bulk band

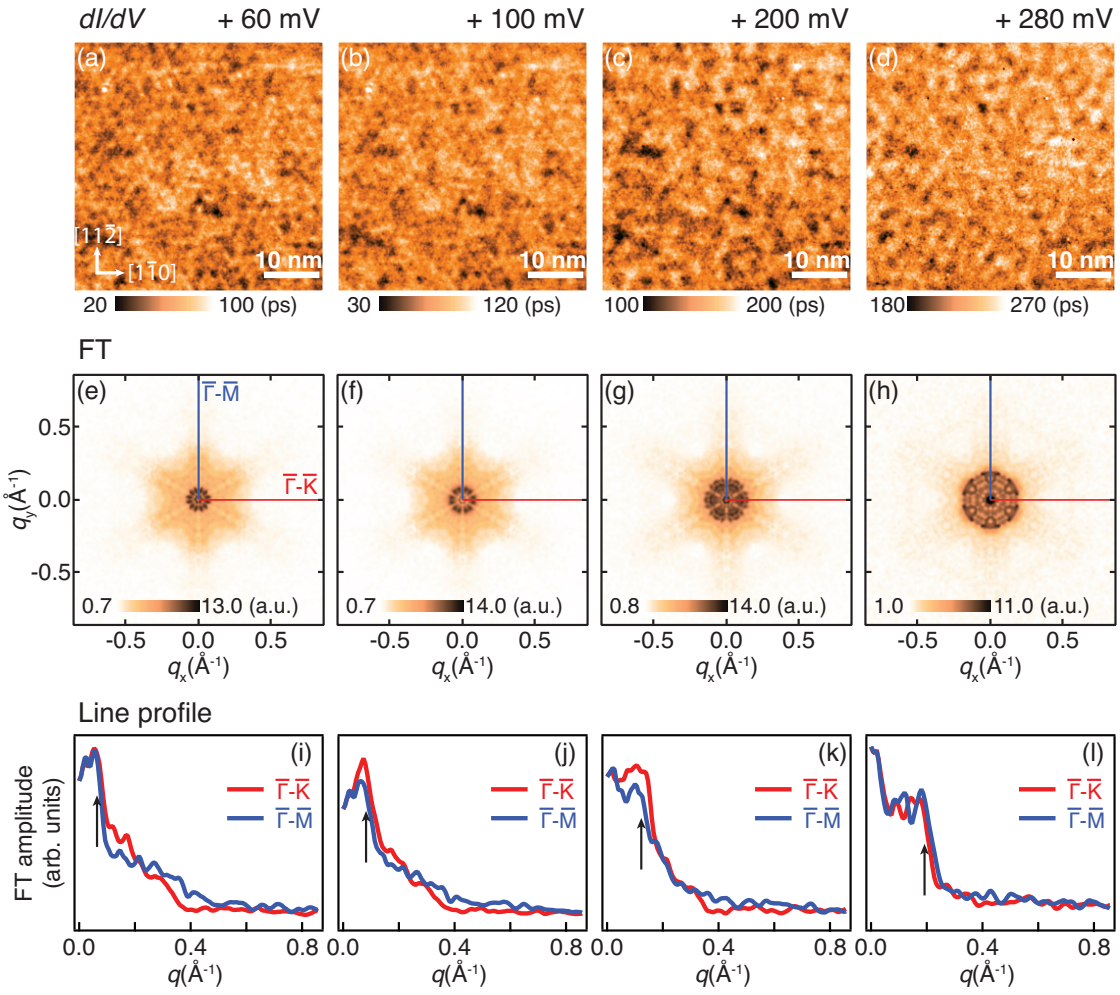

Figure 4.6: Differential conductance images of the cleaved $Bi_{1.5}Sb_{0.5}Te_{1.7}Se_{1.3}$ surface for (a) 60 mV, (b) 100 mV, (c) 200 mV, and (d) 280 mV. (e)-(h) Corresponding Fourier transformed amplitude images. (i)-(l) Cross-sections of Fourier transformed amplitude for the images (e)-(h) along both $\bar{\Gamma}$-$\bar{K}$ (red) and $\bar{\Gamma}$-$\bar{M}$ (blue) directions. The black arrows drawn in (i)-(l) indicate the critical scattering vector length. Adapted from [88].

gap. Standing waves due to the quasi-particle interference are observed as spatial modulation in the dI/dV maps. dI/dV maps are Fourier transformed to analyze the interferences. Figs. 4.6(e)-(h) are Fourier transformed amplitude images, corresponding to Figs. 4.6(a)-(d). The reciprocal space was calibrated with the peaks due to the surface lattice and Fourier transformed patterns were symmetrized with respect to the sixfold symmetry, on the basis of the C_{3v} symmetry of the cleaved crystal surface. The cross-sections of the Fourier transformed images at each V_B are plotted in Figs. 4.6(i)-(l) along two high-symmetry directions, $\bar{\Gamma}$-$\bar{\mathrm{K}}$ (red) and $\bar{\Gamma}$-$\bar{\mathrm{M}}$ (blue). As shown in Figs. 4.6(i)-(l), one can realize a steep decrease of the scattering amplitude with increasing length of scattering vector $\mathbf{q}$. Such a steep decrease in the scattering amplitude was observed in the V_B range of 60 - 300 mV, which corresponds to the energy range in the bulk band gap. These cross-section data indicate that the electron scattering within topological surface states rapidly vanishes at a certain critical value of the length of scattering vector. Hence, it is defined as a critical scattering vector length and denoted q_{cx} and q_{cy} for $\bar{\Gamma}$-$\bar{\mathrm{K}}$ and $\bar{\Gamma}$-$\bar{\mathrm{M}}$ directions, respectively.

In the Fourier transformed images, weak six-fold flower-shaped patterns were recognized in the areas outside of the critical scattering vectors. These are explained as follows. The height of the STM tip from the surface is not constant during the measurements of the dI/dV image over the surface, and is determined locally by the integrated local density of states between E_F and the energy corresponding to the bias voltage for fixing the tip position [90]. In this experiment, the tip was fixed using $V_B = 500$ mV. The integrated local density of state includes information on the bulk electronic states with the six-fold symmetry. Even this can affect the Fourier transformed dI/dV images, the artifact does not affect the assignment of the energy dependent round-shaped critical scattering vector, because the shape of the weak artifact pattern is almost independent of the bias voltage.

In order to understand the energy dependence of the critical scattering vectors q_{cx} and q_{cy}, the cross-sections of the Fourier transformed amplitude are arranged as a function of the sample bias voltage. This is shown in Fig. 4.7(a). q_{cx} and q_{cy} are marked by red diamond and blue square on the image, respectively, and one can easily notice obvious increase of critical scattering length with increasing V_B. These symbols are replotted in Fig. 4.7(b). A black dotted line depict in Fig. 4.7(b) shows a linear fitting curve with $E_D = 10$ mV, estimated from Fig. 4.5

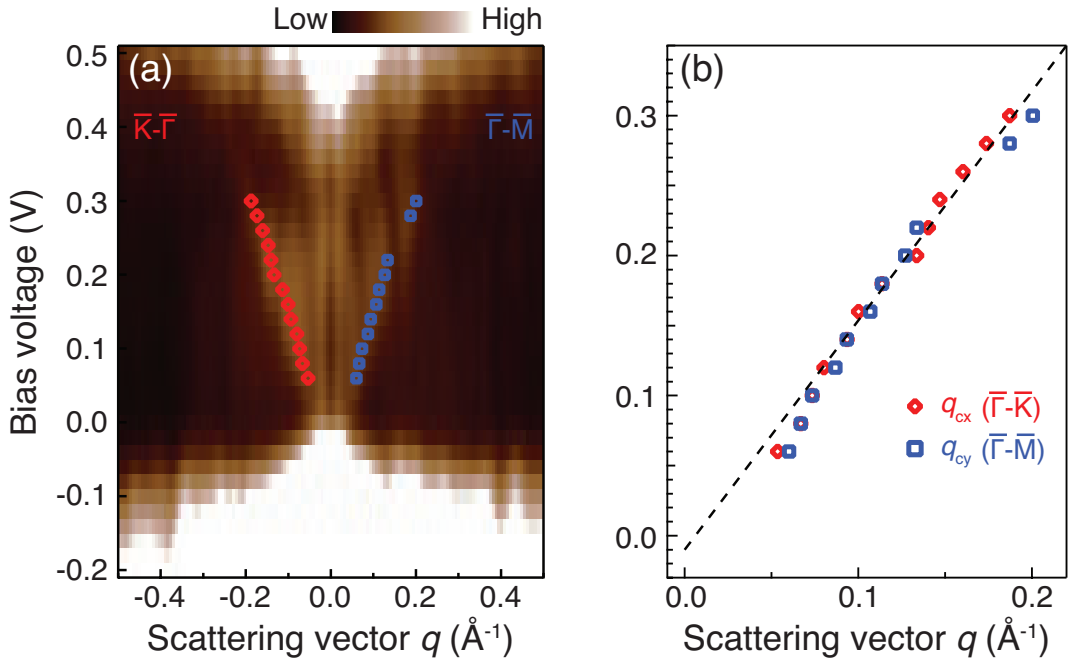

Figure 4.7: (a) Line profiles in the Fourier transformed amplitude intensity as a function of sample bias. The intensity of amplitude plotted along $\bar{\Gamma}$-$\bar{\mathrm{K}}$ (left) and $\bar{\Gamma}$-$\bar{\mathrm{M}}$ (right) directions, respectively. (b) The critical scattering vector lengths q_{cx} (red diamond) and q_{cy} (blue square) for $\bar{\Gamma}$-$\bar{\mathrm{K}}$ and $\bar{\Gamma}$-$\bar{\mathrm{M}}$ directions, overwrote in (a). A black dotted line shows linear fitting curve with $E_D = 10$ mV. Adapted from [88].

above. This result means the critical scattering vector length is dispersing linearly as a function of V_B. Moreover, both q_{cx} and q_{cy} have almost the same value at all V_B below $V_B = 280$ mV, so that one can analogize $Bi_{1.5}Sb_{0.5}Te_{1.7}Se_{1.3}$ has single conical band without warping effect.

4.3.3 Band structure

For the quantitative understanding of the observed critical scattering vector length, information regarding the topological surface state is essential. However, most of topological surface state in $Bi_{1.5}Sb_{0.5}Te_{1.7}Se_{1.3}$ exist above E_F, thus, such information is unavailable with the ordinary ARPES [85]. The advantage of TrARPES can leads to it possible to measure band dispersion even above E_F with a high resolution. Inverse photoelectron spectroscopy[70, 91, 92], even with angle-resolvable [93, 94], also allows to observe unoccupied electronic structures, however, the energy resolution is very low (∼several hundreds of meV), that to detect topological surface state is quite difficult, because size of bulk band gap is only ∼300 meV.

Figs. 4.8(a) and 4.8(b) show photoelectron intensity images measured with TrARPES on a cleaved $Bi_{1.5}Sb_{0.5}Te_{1.7}Se_{1.3}$ surface along the $\bar{\Gamma}$-$\bar{\mathrm{K}}$ direction, the measurement range is indicated with yellow thick in the inset of Fig. 4.8(a), before ($t = -0.8$ ps) and after ($t = +1.1$ ps) 1.5 eV pump photons, respectively. While the only occupied states are visible without pump photons, the band dispersion of the topological surface state was observed obviously up to 0.25 eV above E_F, also including the bulk conduction band at the center of the surface Brillouin zone, after band filling with pump photons. E_D is located at $E = 0.15$ eV below E_F in the TrARPES data shown in Fig. 4.8, and lower than that estimated from spectra shown in Figs. 4.5(a) and 4.5(b). This is caused by the electron doping from adsorbates of residual gas, such as hydrogen, in UHV chamber during TrARPES measurements at low temperature [95], which cannot be happened during STM measurement due to the radiation shield of cryostat. In spite of the energy shift of E_F, the velocity of TSS band remains the same, thus, it does not affect the further discussion.

The momentum distribution curves (MDCs) in the same energy range of Figs. 4.8(a) and 4.8(b) are represented in Figs. 4.8(c) and 4.8(d), respectively, where

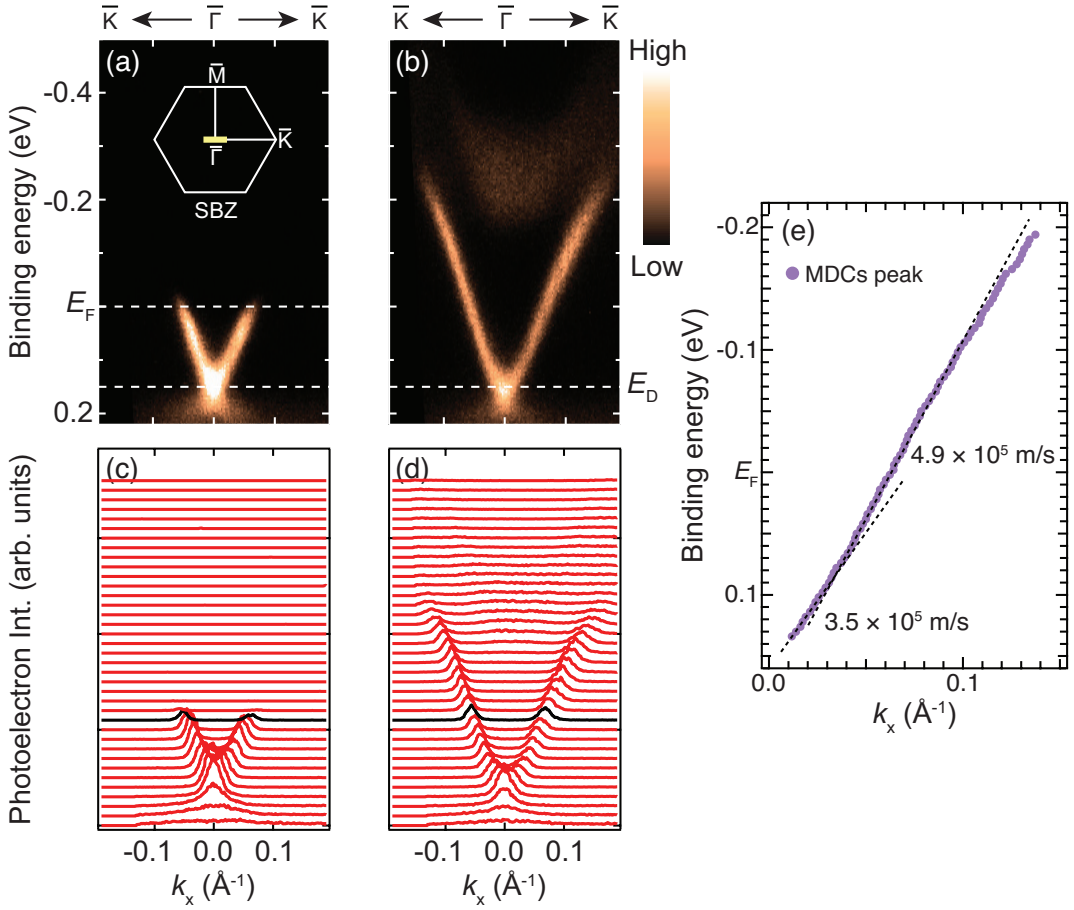

Figure 4.8: Photoelectron intensity images of $Bi_{1.5}Sb_{0.5}Te_{1.7}Se_{1.3}$ along $\bar{\Gamma}$-$\bar{K}$ direction observed (a) before (-0.8 ps) and (b) after (+1.1 ps) filling the empty states with the 1.5 eV pump photons, respectively. (c) and (d) show momentum distribution curves in same energy range of (a) and (b). The black curves are spectra at E_F, and the energy separation between two adjacent curves is 20 meV. (e) The peak points are plotted from all MDCs of (b). The inset of (a) shows the surface Brillouin zone of $Bi_{1.5}Sb_{0.5}Te_{1.7}Se_{1.3}$ and the yellow thick line indicates the measurement range. Adapted from [88].

black curves correspond to spectra at E_F. The peak positions of all momentum distribution curves taken from Fig. 4.9(b) are plotted in Fig. 4.9(e), obtained by analyzing the MDCs with Lorentzian function. The velocity of the surface band can be estimated as 4.9×10^5 m/s for $E - E_D > 80$ meV, and decreases to 3.5×10^5 at $E - E_D = 30$ meV as previous reports on Bi_2Se_3 [54, 96].

4.3.4 Electron scattering process

In order to clarify the elastic scattering process in the topological surface state of $Bi_{1.5}Sb_{0.5}Te_{1.7}Se_{1.3}$, the critical scattering vector lengths were analyzed quantitatively. Compared q_{cx} and q_{cy} with the diameter of the cross-section of the single topological surface state observed by TrARPES are shown in Fig. 4.9(a). Fig. 4.9(a) is reproduced from Figs. 4.7(b) and 4.8(e) with vertical axis to be energy relative to E_D. The critical scattering vector lengths are only about 75 % of the corresponding diameter of the topological surface state at the energy between 90 an 310 meV above E_D. If the scattering is permitted for the scattering angle up to 180°, namely, no restriction for backscattering, either the only perfect backscattering is prohibited, q_c should have equal value with the diameter of the topological surface state. For instance, in the spin degenerate system, such as high-T_C superconductors, the scattering vectors equal to the diameter of the constant energy contour observed by ARPES [97, 98] In order to understand this 75 % of scattering vector length between the two states, the scattering angle of each energy point was calculated as represented in Fig. 4. 9(b). A black dotted line indicates a linear fitting curve, which has the only constant variable corresponding to the angle. The averaged scattering angle is $98 \pm 1°$. Hence limited q_c to 75 % of the diameter of the topological surface state means the maximum of the allowed scattering angle to be 100°.

This situation is schematically well described in Figs. 4.9(c)-(e). Fig. 4.9(c) is a schematic drawn of the shape of the upper Dirac cone with the available scattering vectors at representative energies. Figs. 4.9(d) and 4.9(e) are cross-sections of circular and warped topological surface state with energy dependence, respectively. Those graphics represent the maximum scattering angle does not change with energy, which can be also recognized from Fig. 4.9(b). Particularly, this result indicates that not only the 180° backscattering but also a rather wide

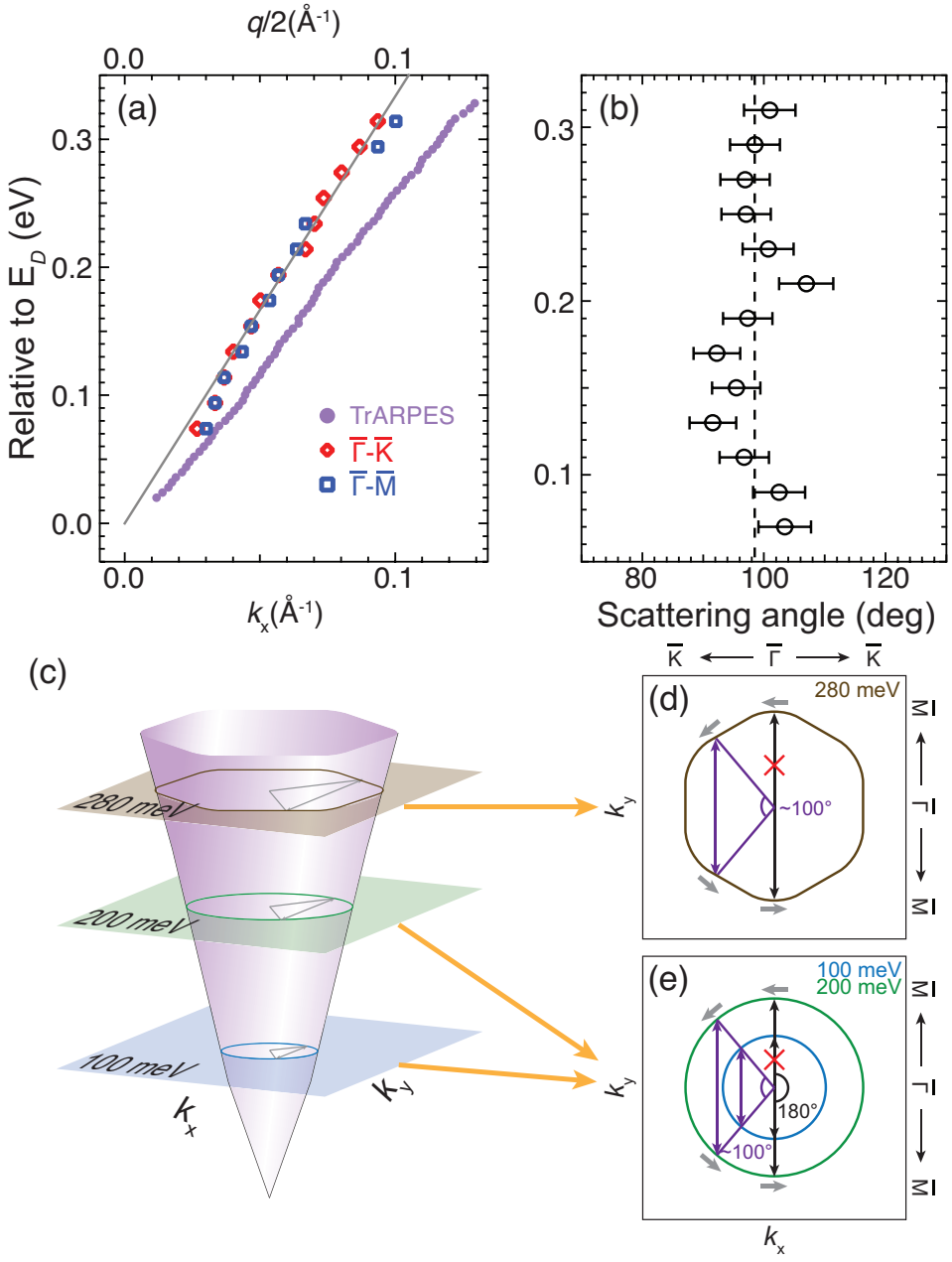

Figure 4.9: (a) Comparison between the critical scattering vector (red diamond for q_{cx} and blue square for q_{cy}) and diameter of constant energy contour of the topological surface state taken from TrARPES (purple filled circle) result. (b) Scattering angle at each energy from E_D calculated from (a). (c) A schematic picture of the energy dependent shape of the upper Dirac cone with the available scattering vectors at representative energies. (d), (e) Schematic pictures for circular and warped TSS, respectively, to indicate the critical scattering vector lengths being 75 % of the diameter of TSS corresponds to the maximum angle of 100°. Adapted from [88].

range of backscattering angle of $100° - 180°$ are effectively suppressed due to the spin mismatch between the initial and final states in the topological surface state.

The spin mismatch mechanism for the present helical spin system introduces an angle dependent factor to the scattering probability. This factor is given as $1+\cos\theta$ [99] that the probability decreases rapidly with increasing θ, where $\theta > 90°$, and completely vanishes at $\theta = 180°$. This explains the strong suppression of scatterings for a relatively wide range of the scattering angle, at least qualitatively.

4.4 Conclusion

The angle dependent scattering process was clarified using the results of STM and STS, as well as TrARPES experiments. Quasi-particle interferences due to the elastic scattering of electrons were observed using STM and STS. The amplitude of the scattering vector were suddenly decreased at a certain scattering vector length. Beyond such a critical scattering vector lengths, the elastic scattering of electrons in the topological surface state is much suppressed. Those critical scattering vector lengths were compared with the diameter $2k$ of the topological surface band for the electronic empty states obtained from TrARPES. We found that the critical scattering vector lengths are only 75 % of $2k$, and conclude that the protection from backscattering in the topological surface state occurs not only for 180° but also for a rather wide angle range of $100° - 180°$. If the scatterings are fully allowed, the maximum scattering vector length should be equal to $2k$ in the circular constant energy contour. Such a wide angle range for the prohibition of backscattering is revealed to be independent of the energy until the Dirac cone becomes warped.

Above the energy of 300 meV from the Dirac point, where the Dirac cone warping appears, hexagonal patterns in the Fourier transformed images come from the warped Dirac cone. It might be similar to Fig. 4.9(d), however, in this range the critical scattering vector was not precisely observed. When V_B is larger than 300 meV, the bottom of the bulk conduction band is located there. Because of the spin degenerate bulk state, surface - bulk scattering becomes dominant at those energies. In case of negative V_B, the scattering within the bulk states leads the strong amplitude in the Fourier transformed dI/dV. This implies the scatterings within the topological surface state are overwhelmed by the bulk scattering events with the same scattering vectors, hence, the former are hardly visible.

A quantitative analysis of elastic backscattering of spin-polarized electrons in the bulk-insulating topological insulator allows to understand the robust protection from the backscattering in the same system. This new understanding can be good news for applications, simultaneously, suggest another challenge to the theoretical understanding of the transport in the topological Dirac states.

4. ANGLE DEPENDENT SUPPRESSION OF ELECTRON BACKSCATTERING IN THE TOPOLOGICAL INSULATOR

Chapter 5

Photoexcited carrier dynamics of Dirac fermion in the intrinsic topological insulator

5.1 Introduction

5.1.1 Carrier dynamics in solid surface

The development of the pulsed laser source and an ultrafast pump-and-probe method led the time-resolved photoelectron spectroscopy technique, which made it possible to observed ultrafast time-dependent electronic structures directly. Thereby, the electron dynamics of the various solid surface systems has revealed with this epochal technique [72]. Using this technique, the detailed mechanisms of electron scattering, such as electron-electron scattering or electron-phonon scattering, and electron-hole recombination at the surface have been studied. Moreover, recent development of the time-resolved photoelectron spectroscopy system has enabled us to observe electron dynamics with high energy resolution.

5.1.2 Dynamics of the excessive hole doped topological insulator

The topological surface state is promised to be robust due to the suppression of the backscattering. Because of this peculiar property, the optically excited

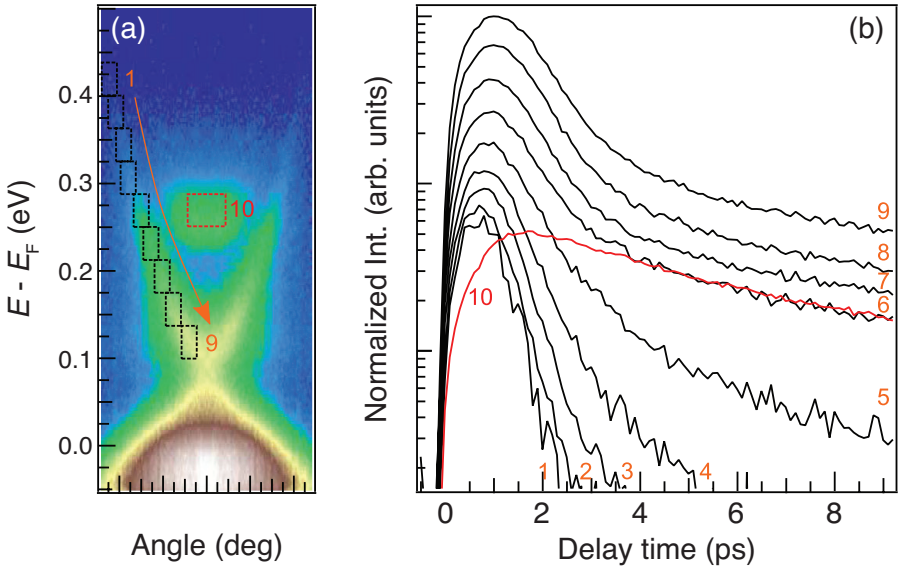

Figure 5.1: (a) Photoelectron intensity image of excessively hole-doped Bi_2Se_3 observed by TrARPES. (b) Transient photoemission intensities integrated within the each window drawn in (a). The red curve is taken from bulk conduction band. Adapted from [89].

electron dynamics in the three-dimensional topological insulator has become an interesting subject. In particular, a "bulk-insulating" topological insulator shows a well-controlled two-dimensional metallic surface state between the intrinsic insulating bulk energy gap, a new class, even if the spin-polarization of the topological surface state are not concerned.

Meanwhile, a time- and angle-resolved photoelectron spectroscopy experiment was performed in one of the three-dimensional topological insulator Bi_2Se_3 [89]. The transient characteristic of the *p*-type Bi_2Se_3, which is excessively hole-doped, were observed as shown in Fig. 5.1. The transient photoelectron intensity curves from the energy resolved surface state and bulk conduction band are shown in Fig. 5.1(b). Surprisingly, the transient curves from the surface state with the energies below the bulk conduction bottom don't show any energy dependence and the latter part of them seem to be dominated by that of the conduction band bottom. From this result, a continuos supplying of electrons from the bulk conduction band to the topological surface state is suggested, however, detailed scattering process and the own decay parameter of the surface state are still veiled. Moreover, the bulk

valence band of this materials exists at the Fermi level because of the heavy doping, so that the electron dynamics is concerned to be affected by the bulk metallic electron dynamics. Thus, in order to clarify the original dynamics of the topological surface electrons in a bulk-insulating topological insulator, we have studied the electron dynamics in the intrinsic bulk-insulating sample $Bi_{1.5}Sb_{0.5}Te_{1.7}Se_{1.3}$ with TrARPES.

5.2 Experiment

TrARPES system as drawn in Fig. 3.8 with a hemispherical analyzer was used for the experiment as described in Sec. 4.2. In this experiment, both pump and probe are linearly polarized. In order to understand ultrafast dynamics, the calibration of the delay time point of $t = 0$ (t_0) should be very important. In other words, both pump and probe photons illuminate the surface simultaneously. In the present experiment, a single crystal of graphite was used for the standard sample to calibrate t_0 and the total time resolution. The electronic structure of graphite is well-known, and the preparation of its clean surface is quite simple. Thus it is suitable for the calibration. Fig. 5.2 shows the normalized photoelectron intensity observed at each delay stage position. The photoelectrons were observed between 3.0 and 3.1 eV of kinetic energy, where are 1.4 to 1.5 eV above Fermi edge, because 1.5 eV pulse was used for the pump. The intensity curve is fitted by Gaussian, and the value of the delay stage position at t_0 is estimated as 26467. The full width at half maximum (FWHM) of the Gaussian is calculated as 21.844, which corresponds to the converted total time resolution $\sim$ 290 fs. The pulse width of the pump is 170 fs, hence, the pulse width of the probe is estimated to be $\sim$ 250 fs. Moreover, the flux of the probe pulse was controlled not to occur the space-charge effect [100, 101]. A bunch of photoelectrons generated by the intense probing pulse repel each other due to the Coulomb interaction, that distorts the energy and angular distribution of the photoelectrons. Thus, this space-charge effect should be minimized to measure the fine structures correctly.

The clean surface of the sample was prepared by the cleaving with scotch tape as Fig. 4.3(b) in the UHV system, of which the base pressure was below 2×10^8 Pa. The sample is cooled down to 5 K soon after the cleaving. In the present study, the band structure at each delay time was observed repeatedly during the delay

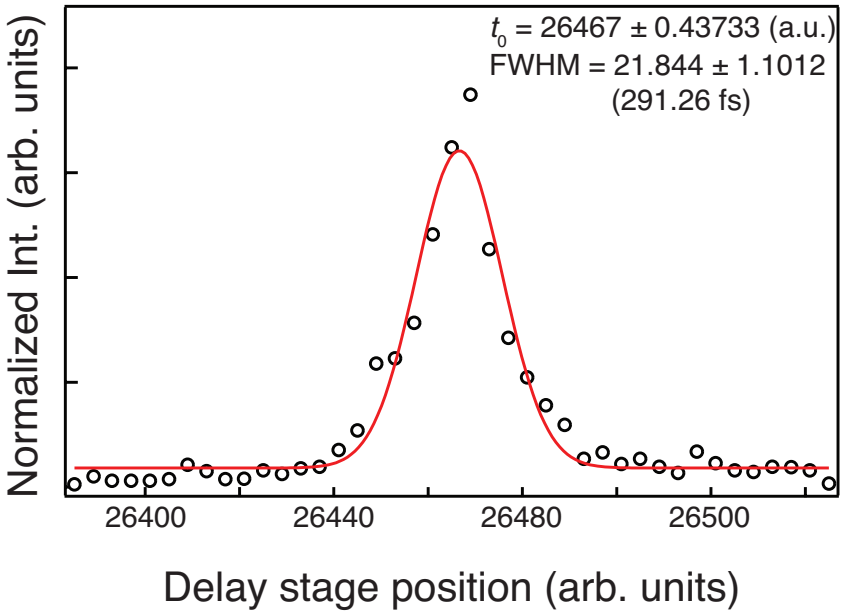

Figure 5.2: Calibration of $t = 0$ (t_0) with Graphite. Delay stage position of t_0 is 26467 and time resolution of the whole TrARPES system is estimated to be $\sim$ 290 fs. The curve is fitted by Gaussian.

stage going and returning.

5.3 Results and discussions

5.3.1 Transient characteristic

Observed photoelectron intensity snapshots at several selected delay times, $t = -2.67, -0.2, 0, +0.2, +0.67, +1.96, +5.39, +10.95$ and $+19.24$ ps, are displayed in Fig. 5.3. All images were observed along $\bar{\Gamma} - \bar{\mathrm{K}}$ direction, referred to the surface Brillouin zone as depict in the inset of Fig. 4.8(a). Fig. 5.3(a) shows the spectrum observed at a negative delay time before the arrival of the pump photons and indicates the thermally equilibrium electronic state, the ground state. In Fig. 5.3(b), showing the result just before the pump pulse arriving, photoexcited electrons became observable. The photoelectron intensity were clearly observed even up to 1 eV above the Fermi energy in Figs. 5.3(c) and 5.3(d), of which the delay times are 0 and +0.2 ps, respectively. The electrons filled the unoccupied states, thus

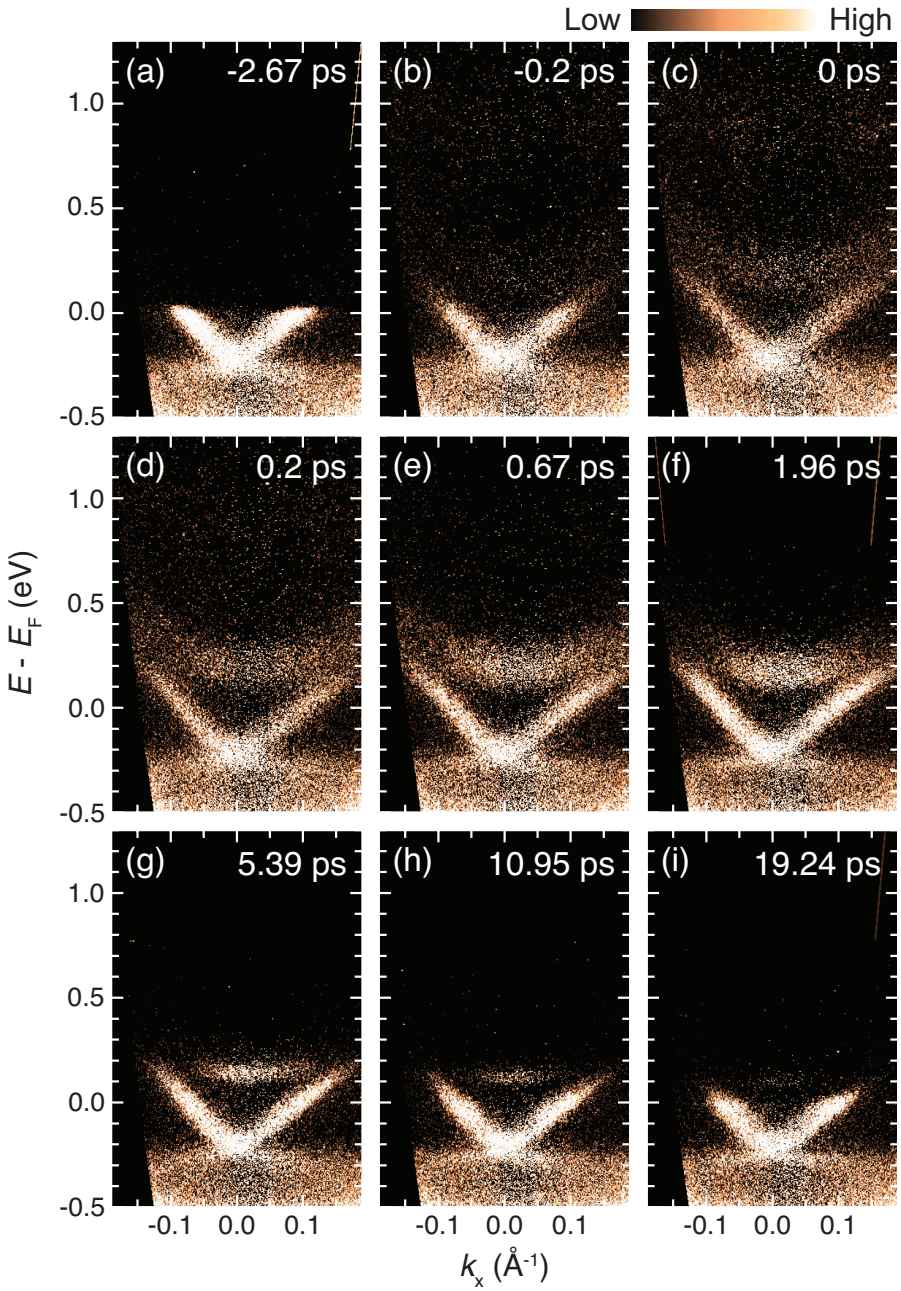

Figure 5.3: (a)-(i) Snapshots of photoelectron intensity images observed along $\bar{\Gamma}-\bar{\mathrm{K}}$ at delay times of $t = -2.67$(a), -0.2(b), 0(c), 0.2(d), 0.67(e), 1.96(f), 5.39(g), 10.95(h), and 19.24 ps (i), respectively. Precise photoexcitation and relaxation are visible.

the upper Dirac cone above the Fermi level and the bulk conduction band were observed as in those figures. The populated electrons at t_0 are slowly scattered into the states with the lower energy and the electron relaxation can be traced in Figs. 5.3(b)-(i). Even at $t = +19.24$ ps of the delay time, the bottom of the conduction band was still found, indicating this system has a pretty long lifetime.

In the Fig. 5.3(a), one can notice the photoelectron intensity even slightly above ($\sim$ 20 meV) the Fermi level, which was fixed using the spectrum without the pump pulse. This is a phenomenon caused by the repetitive pump pulses. After the sample pumped, if the system does not fully recovered to the ground state before the next pump, the photoelectrons can be observed above the Fermi level. Surface photo-voltage effect [102] exhibited from a semiconductor surface can be an example relevant to this phenomenon. Generally, the lifetime of surface photo-voltage exceeds micro seconds order, hence, if the interval time of the pump pulses is shorter than the lifetime of the surface photo-voltage, pump-induced energy shifts can be observed even at $t < 0$ [73]. The repetition rate dependent pump-induced shift of SmB_6 was attributed to the surface photo-voltage [103]. The spectra shift shown in Fig. 5.3(a) is considered to have the same origin because a bulk-insulating band structure is similar to a semiconductor.

In order to understand the further transient character, the observed photoelectron intensity was integrated within the selected windows drawn in Fig. 5.4(a). Fig. 5.4(a) is a snapshot of photoelectron intensity image at $t = +0.2$ ps, the same as Fig. 5.3(d). We modified the image for explanations. Red and blue windows are drawn on the topological surface state and bulk conduction band, respectively. A green window on the energy more than 1 eV from E_F indicates another bulk band. In Fig. 5.4(a) we divided the each window into sub-windows with the energy range of 50 meV. Then we integrated the photoelectron intensity in each sub-window. The integrated intensity is plotted as a function of delay times, which are shown in Figs. 5.4(b), (c) for topological surface state and Figs. 5.4(d), (e) for bulk conduction band. The transient curves taken from different energy described in corresponding color to the scale bar drawn above the graph. The transient curve of the green window in Fig. 5.4(a) is shown in the inset of the Fig. 5.4(d). All curves have their peak positions not on $t = 0$ due to the indirect population by scattering from the states with higher value of energy. This is consistent with the previous study [89, 104]. In both surface and bulk states, the intensity curves show

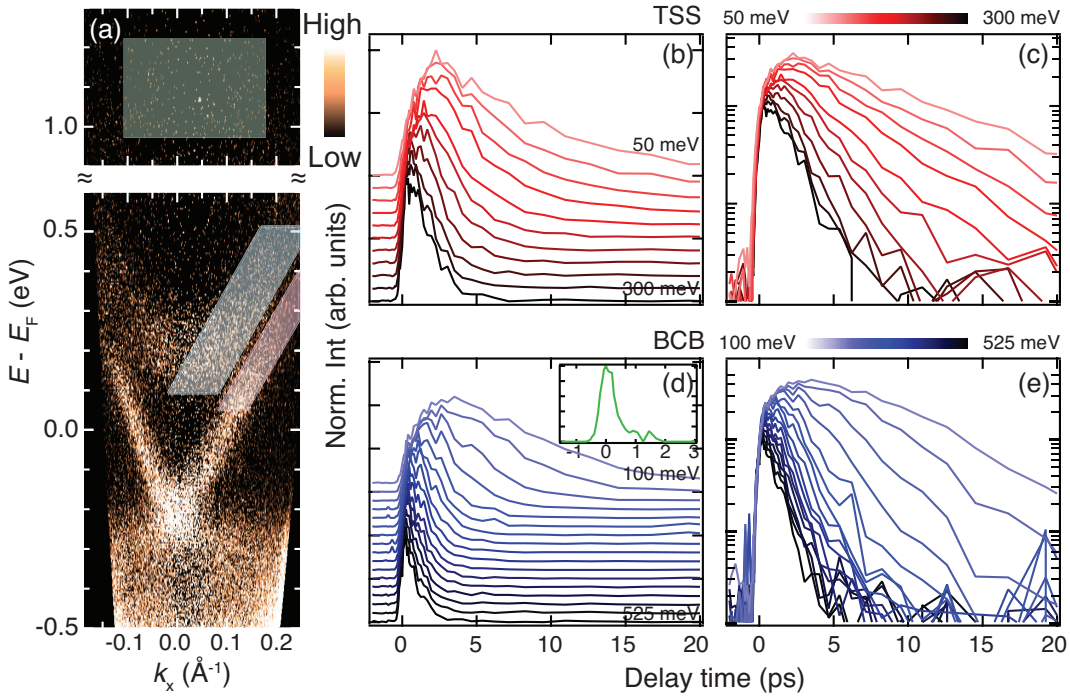

Figure 5.4: (a) Photoelectron intensity image observed at delay time of $t = 0.2$ ps. (b) Normalized photoelectron intensity as a function of delay time taken from the red area in (a), which is corresponding the topological surface state. Same curves are plotted with logarithmic scale in (c). The red scale bar shows the energy from Fermi level of filled area in (a) and the curves with same color is taken from the corresponding energy. The transient curves from the blue area (conduction band) are represented in (d) and (e) same as (b) and (c). The inset of (d) shows transient curve of green area in (a), much higher energy above more than 1 eV from Fermi energy.

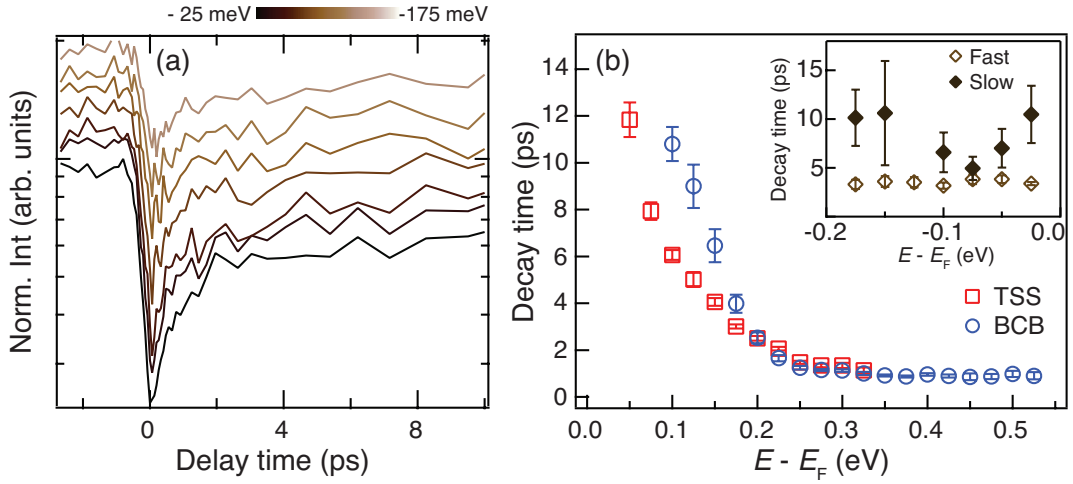

Figure 5.5: (a) The transient curves of holes (topological surface state) plotted similarly to Fig 5.4(c) in log scale. In contrast to the electron dynamics, the relaxation obviously have two components, before and after about 2 ps. (b) Energy dependent decay times, calculated from Figs. 5.4(c) and 5.4(e), fitted by single exponential curve. Both surface (red square) and bulk (blue circle) decay times have energy dependence and bulk conduction band has much longer lifetime. The inset of (b) is decay time of the surface holes, which has two component, before (opened diamond) and after (filled diamond) 2 ps. No energy dependence is found.

an energy dependence, which is precisely described in Figs. 5.4(b) and 5.4(d). Interestingly, the intensity of the surface and bulk electrons does not fully decay even at $\sim$ 20 ps. Figs. 5.4(c), (e) show the same results in log scale and indicate the decays with single exponential components.

The decay time τ of each curve is calculated by curve fitting with single exponential. The calculated decay times of all curves in Fig. 5.4(c),(e) are shown in Fig. 5.5(b) as a function of the energy from the Fermi level. In Fig. 5.5(b), one can realize that the decay times of both the topological surface state and bulk conduction band depend on the energy, and become longer with decreasing energy. At higher energy ($>$ 0.2 eV from the Fermi level), the decay times of both states are very similar, however, at lower energy than that, the bulk conduction state shows much longer decay time than the surface state.

The time evolution of the topological surface holes was also measured. Fig. 5.5(a) shows the energy-dependent transient curves of holes in the topological surface

state. In contrast to the results of the electron dynamics, the transient curves taken from several different energies show almost the same relaxation so that there is no energy dependence. As well as, contrary to the electrons in the both surface and bulk states, those obviously have two components in the decay process. Before 2 ps of the delay time, the intensity decays very fast, however, it decay slowly after 2 ps. Each component of decay times are calculated from the transient curves shown in Fig. 5.5(a) by fitting the data with single exponential curve separately before and after 2 ps. The calculated relaxation time are shown in the inset of the Fig. 5.5(b). Opened and filled diamond indicate two decay components of fast and slow, respectively. The two components are independent of the binding energy. The transient curves show that the holes are not perfectly decayed even at 10 ps of the delay time, which corresponds to the result of electrons that the relaxation is not finished even over the 10 ps.

5.3.2 Fermi level dependence

In order to bring out the own dynamics of the bulk-insulating topological insulator, the result described in Sec. 5.3.1 was compared with several samples of different Fermi energy. Fermi level was varied by exposing the cleaved $Bi_{1.5}Sb_{0.5}Te_{1.7}Se_{1.3}$ to the residual gas in UHV system [85]. Figs. 5.6(a)-(g) show the energy shift by band bending due to the gas adsorption during the TrARPES measurements. The data shown in Fig. 5.6(g) was measured at 20 hours after the data in Fig. 5.6(a). Both the surface and bulk states were shifted as a rigid band shift. After finishing the whole experiments, the sample was annealed up to room temperature again and the band dispersion was returned to the first. Which indicates that the adsorbed gases desorbed and the sample surface was not destroyed during the adsorption. The surface state is as stable as the previous study with ARPES [105]. The white dotted lines in figures indicate the Dirac energy $E_D = 0.21, 0.25, 0.27, 0.31, 0.35, 0.36$ and 0.37 eV of binding energy. One can realize that, in Figs. 5.6(e)-(g), the bulk conduction band clearly crosses the Fermi level while Figs. 5.7(a)-(c) are bulk-insulating. As well as, the bottom of the conduction band just touched to the Fermi level in Fig. 5.7(d).

To understand the detail of electron dynamics in each states shown in Fig. 5.6, the time evolution of the photoelectron intensity were analyzed. Figs. 5.7(a) and

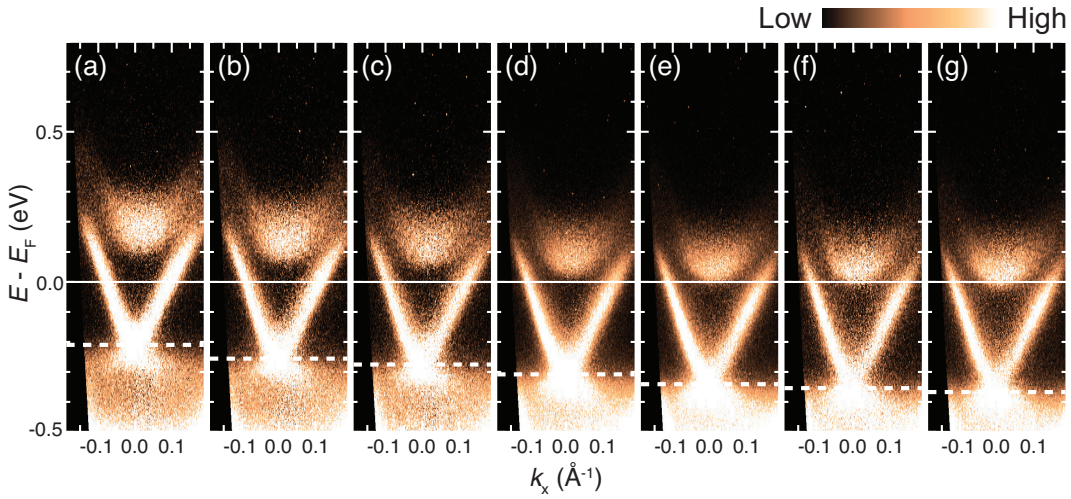

Figure 5.6: (a)-(g) Observed band dispersions as photoelectron intensity. White solid lines indicate the Fermi level, that the Fermi level shift is visible. White dotted lines show the Dirac energy $E_D = 0.21, 0.25, 0.27, 0.31, 0.35, 0.36$ and 0.37 eV below E_F, respectively. All images are from integrated photoelectron intensity between 0.67 and 1.96 ps of delay times.

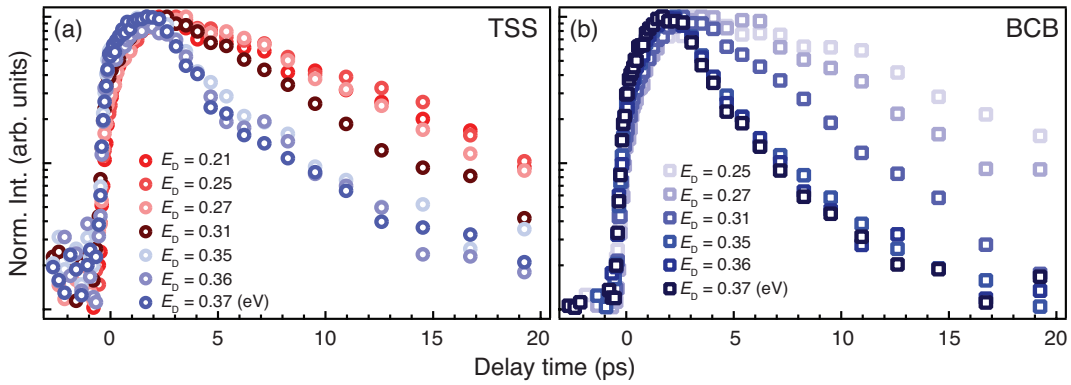

Figure 5.7: Transient photoelectron intensity curves of (a) the topological surface states and (b) bulk conduction band at the energy 75 meV above E_F. The curves taken from the data shown in Fig. 5.6 of corresponding E_D.

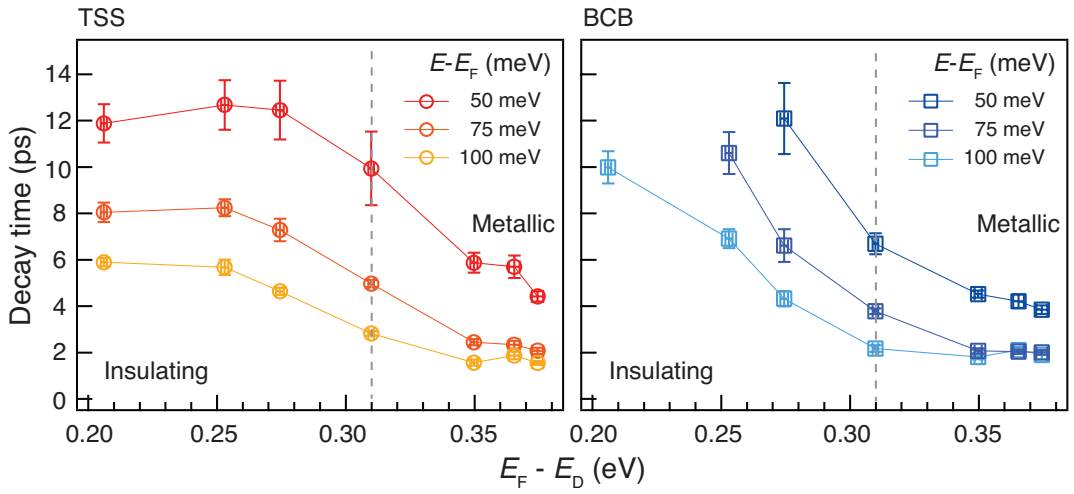

Figure 5.8: Decay times calculated at 50, 75 and 100 meV above from the Fermi level as a function of the Dirac energy for (a) the topological surface state and (b) bulk conduction band. Each color corresponds to the energy where the intensities are integrated. The grey vertical dotted line indicates the energy between the Dirac point and the bottom of the conduction band, equal to 0.31 eV.

5.7(b) show the integrated photoelectron intensity curves of the surface and the bulk states at 75 meV above the Fermi level, respectively. All the intensities are integrated from the band dispersions with corresponding Dirac energy with the energy window of 50 meV. In Fig. 5.7(a), the transient curves can be separated to two groups. One is the group plotted with red opened circles and the other is the group plotted with blue opened circles. The case of $E_D = 0.31$ eV is the boundary between the two groups. Interestingly, the former group corresponds to the photoelectron intensity images with the conduction band above the Fermi level. The decay time is changed very much at $E_D = 0.31$ eV. A similar, but, a little different tendency can be seen in Fig. 5.7(b) for the bulk band. The decay time τ gradually decrease with the band shift from $E_D = 0.25$ eV, and become convergence when the bulk conduction band crosses the Fermi level. Moreover, one can recognize that both the decay curves of the surface and bulk states have two different components with the metallic bulk state.

The same analysis is applied to two more different energy of 50 and 100 meV above from the E_F. Figs. 5.8(a) and 5.8(b) show the calculated decay times at 50, 75 and 100 meV above the Fermi level as a function of the Dirac energy for

the topological surface states and the bulk conduction bands, respectively. The grey dotted line shows the difference of the energy between the Dirac point and the bottom of the conduction band, which is equal to 0.31 eV, so that the bulk conduction band starts to cross the Fermi level from Fig. 5.6(d) with increasing $E_F - E_D$. In each graph, three plotted curves behave similar. In the band dispersion with $E_F - E_D > 0.31$ eV, one can realize that the decay times converge without the classification of bulk and surface.

5.3.3 Electron-hole recombination

As described in Sec. 5.1.1, there are several kinds of mechanisms to determine electron dynamics [72], including both elastic and inelastic scattering. Focusing to the photoexcited electrons as the present experiment, the inelastic scattering can be considered to explain the electron dynamics. Because the energy of the excited electrons are very high, so that those can return to their ground state by the inelastic scattering, such as electron-phonon scattering. After such a scattering, electrons near Fermi level can be recovered to the ground state by electron-hole recombination.

The observed electron dynamics can also be explained by these scattering process. In case as shown in Fig. 5.6(a), the bulk-insulating, the calculated decay time shows that the electrons of the bulk conduction band have a larger τ than the electrons of the topological surface band as described in Fig. 5.5(b). Because of the energy gap between the bulk conduction band and the bulk valence band, the electrons of the bulk conduction band are difficult to recombine with holes directly. Thus, they can be scattered into the surface state, and can recombine with holes below the Fermi level soon after the scattering. This scattering process will be described in detail with a simple simulation in Sec. 5.3.4. On the contrary, the electrons from the topological surface state can be scattered to both bulk and surface bands with lower energy, and the electrons, which scattered into the surface band with lower energy, can recombine with holes at Fermi level. In the bulk-insulating case, as shown in Fig. 5.9(a), the only channel of the recombination between electrons and holes in topological surface state can be possible. Thus , the decay process of electrons in the surface state does not depend on the Fermi level, if the band structure keeps the bulk-insulating character. This corresponds to the result of

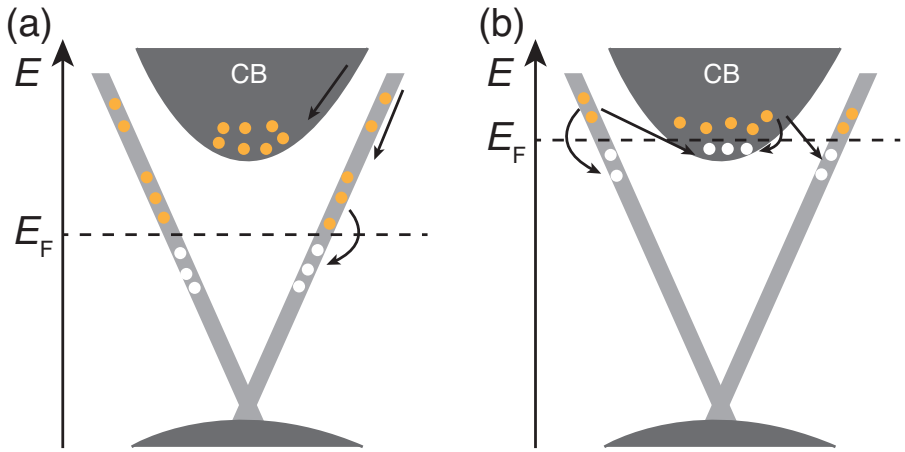

Figure 5.9: (a) A schematic drawn band diagram of the bulk-insulating topological insulator and (b) n-type topological insulator with bulk conduction band at E_F. In both, electron - hole recombination channels are depict on each diagram.

bulk-insulating part shown in Fig. 5.8(a).

In the bulk metallic case, after the pump pulse, both electrons and holes generated in the bulk conduction band. Therefore, holes remain not only in the topological surface state, but also in the bottom of the conduction band. Considering the recombination process, holes in the bulk conduction band can affect to the dynamics. As shown in Fig. 5.9(b), electrons in the surface state above the Fermi level can recombine with holes in both of the surface state and the bulk conduction band. The opposite is also possible that the electrons in conduction band above the Fermi level can be scattered into both surface and bulk band. Reminding that the transient curves shown in Fig. 5.7 from the bulk metallic samples seem to have two different decay components, a few picoseconds and over 5 ps. This is also related to the bulk conduction band. Because of the holes in the bulk conduction band, electrons can take a lot of channels to recombine. However, the hole density in the conduction band is quite small, that the recombination with hole in the conduction band will finish very soon. Note that the bottom of the bulk conduction band is lying just below the Fermi level. The gradients of the latter part in the transient curves, actually similar to that of transient taken from the bulk-insulating sample. Which means the latter part corresponds to the electron (TSS) - hole (TSS) recombination.

5.3.4 Electron scattering process

As described in Sec. 5.3.1, the decay time of the bulk conduction state is much larger than the that of surface state. In order to understand such a different decay time between two states at low energy, transient curves are simulated with following scattering process as shown in Fig. 5.10. Figs. 5.10(a)-(c) show the initial condition with three steps. First, an equilibrium state (ground state) is supposed. And the electrons are photoexcited to the high energy (B_0) by the pump pulse. Finally, those electrons distribute into the other five different states, B_1, B_2, S_1, S_2, and S_3, as non-thermal process. The electron filling of B_0 as a function of the delay time t can be described as

$$\begin{aligned}\frac{dB_0(t)}{dt} &= P_0(t) - \frac{B_0(t)[1-B_1(t)]}{b_{01}} - \frac{B_0(t)[1-B_2(t)]}{b_{02}} \\ &\quad - \frac{B_0(t)[1-S_1(t)]}{c_{01}} - \frac{B_0(t)[1-S_2(t)]}{c_{02}} - \frac{B_0(t)[1-S_3(t)]}{c_{03}} \end{aligned} \tag{5.1}$$

where $P_0(t)$ is a gaussian function with the FWHM of total time resolution, $B_i(t)$ ($i = 1, 2$) and $S_j(t)$ ($j = 1, 2, 3$) are the electron filling of each states at t. The rate equations for each state, used to simulate the transient curves, are described as following.

$$\begin{aligned}\frac{dB_1(t)}{dt} &= P_1(t) + \frac{B_0(t)[1-B_1(t)]}{b_{01}} - \frac{B_1(t)[1-S_1(t)]}{a_1} + \frac{S_1(t)[1-B_1(t)]}{a_1} \\ &\quad - \frac{B_1(t)[1-B_2(t)]}{b_{12}} \end{aligned} \tag{5.2}$$

$$\begin{aligned}\frac{dS_1(t)}{dt} &= Q_1(t) + \frac{B_0(t)[1-S_1(t)]}{c_{01}} - \frac{S_1(t)[1-B_1(t)]}{a_1} + \frac{B_1(t)[1-S_1(t)]}{a_1} \\ &\quad - \frac{S_1(t)[1-S_2(t)]}{c_{12}} \end{aligned} \tag{5.3}$$

$$\begin{aligned}\frac{dB_2(t)}{dt} &= P_2(t) + \frac{B_0(t)[1-B_2(t)]}{b_{02}} - \frac{B_2(t)[1-S_2(t)]}{a_2} + \frac{S_2(t)[1-B_2(t)]}{a_2} \\ &\quad + \frac{B_1(t)[1-B_2(t)]}{b_{12}} \end{aligned} \tag{5.4}$$

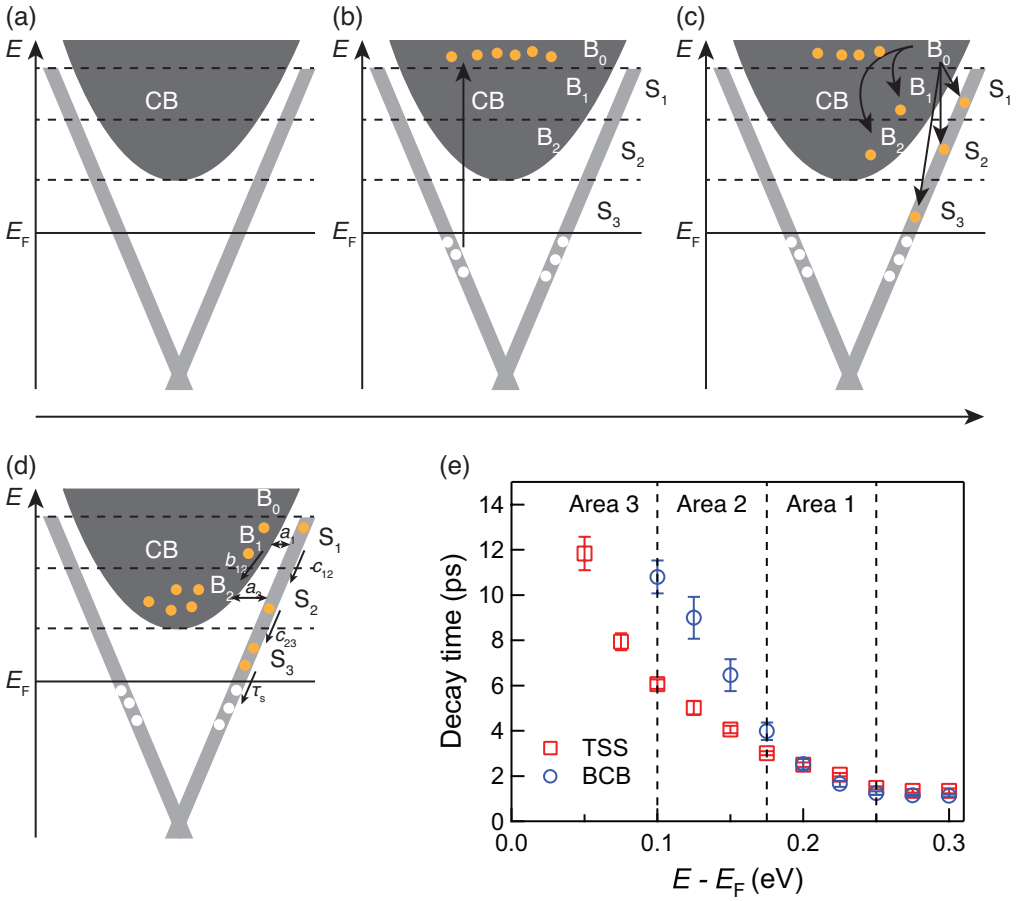

Figure 5.10: (a) An initial state (ground state) before the pump. (b) Photoexcitation of electrons to high energy region (B_0). (c) Non-thermal distribution of electrons from B_0 to the other states. These three steps, from (a) to (c), are supposed as an initial condition. (d) Supposed scattering channels. Each states has scattering channels of drawn arrows with rate parameters. (e) An expanded graph for a part of Fig. 5.5(b). The black dotted lines in (a)-(d) correspond to the energies represented in (e).

$$\frac{dS_2(t)}{dt} = Q_2(t) + \frac{B_0(t)[1-S_2(t)]}{c_{02}} - \frac{S_2(t)[1-B_2(t)]}{a_2} + \frac{B_2(t)[1-S_2(t)]}{a_2} + \frac{S_1(t)[1-S_2(t)]}{c_{12}} - \frac{S_2(t)[1-S_3(t)]}{c_{23}} \quad (5.5)$$

$$\frac{dS_3(t)}{dt} = Q_3(t) + \frac{B_0(t)[1-S_3(t)]}{c_{03}} + \frac{S_2(t)[1-S_3(t)]}{c_{23}} - \frac{S_3(t)}{\tau_s} \quad (5.6)$$

Where $P_i(t)$ $(i = 1, 2)$ and $Q_j(t)$ $(j = 1, 2, 3)$ are the gaussian functions, similar to $P_0(t)$ in Eq. (5.1). a_l $(l = 1, 2)$ is rate parameter for the scattering between the bulk state and the surface state with detailed balance. b_{mn} and c_{mn} $(m = 0, 1, 2$ and $n = 1, 2, 3)$ are the rate parameters of the scatterings to the lower energy within the bulk conduction band and the surface band, respectively. τ_s is a decay time of the state S_3, which represents the time for electron-hole recombination at Fermi level in the metallic surface state.

The simulated curves from the Eqs. (5.2)-(5.6) with parameters written in Table 5.1 are shown in Fig. 5.11(b). The plotted squares and circles represent the integrated photoelectron intensity as a function of delay time taken from each enclosed area drawn in Fig. 5.11(a). Both experimental data and simulation curves show similar behavior that the electrons of the bulk conduction band (B_2) have a larger decay time than the surface state (S_2) at the energy range of area 2, even though the decay curves of two states at higher energy (B_1 and S_1) are very similar. This means that the electrons are accumulated at the bottom of bulk conduction band. The electrons of the bulk conduction bottom have the only scattering channel to the surface state and electron scatterings are delayed because of the low DOS of the surface band and the long distance to the surface band in the momentum space ($a_1 < a_2$). Note, in area 1 shown in Fig. 5.10(e), corresponding to B_1 and S_1, the bulk conduction band and the surface band are close in the momentum space that it is very easy to be scattered into each other. As a result, the supposed scattering process model described in Fig. 5.10 reproduced the experiment results very well and this explains the accumulation of the electrons at the bulk conduction bottom.

The most important point of this simulation is the decay time of the surface state τ_s, which is independent to the decay time of the bulk state. Though the electron scattering from the bulk conduction band, it is possible to estimate τ_s as ~ 4 ps from the above equations. Considering the supposed scattering process, the

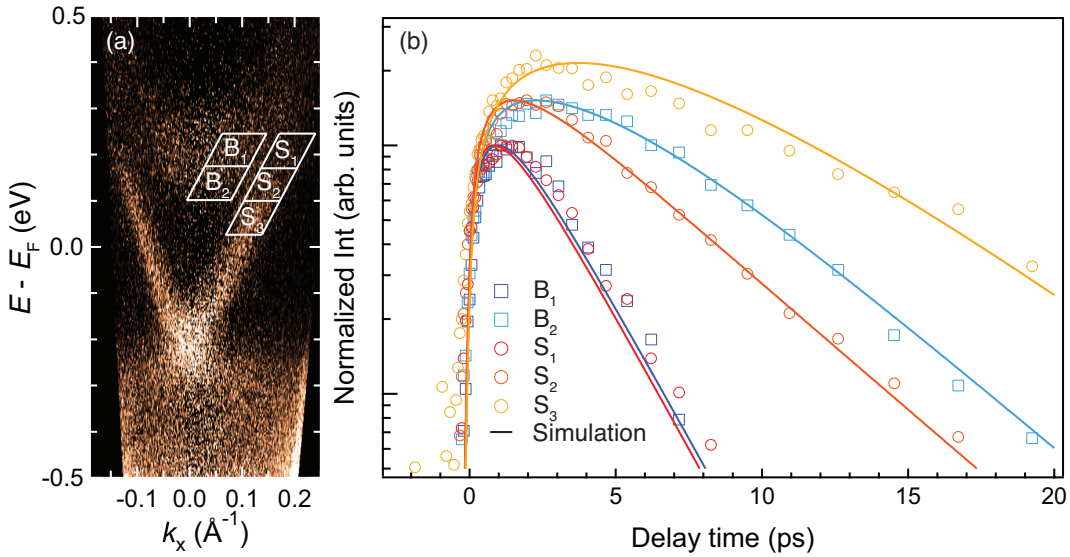

Figure 5.11: (a) Photoelectron intensity image taken at $t = 0.2$ ps. (b) Transient curves taken from the bulk states (squares) and the surface states (circles) indicated in (a). The solid lines with same color indicate the simulation curves from the rate equations of Eqs. (5.2)-(5.6).

a_1	a_2	b_{12}	c_{12}	c_{23}	τ_s
0.7 ± 0.2 ps	2.7 ± 0.2 ps	13.1 ± 0.5 ps	0.9 ± 0.1 ps	1.2 ± 0.1 ps	4.1 ± 0.2 ps

Table 5.1: Parameters for Fig. 5.11(b) estimated from the decay curve simulation with the rate equations of Eqs. (5.2) - (5.6).

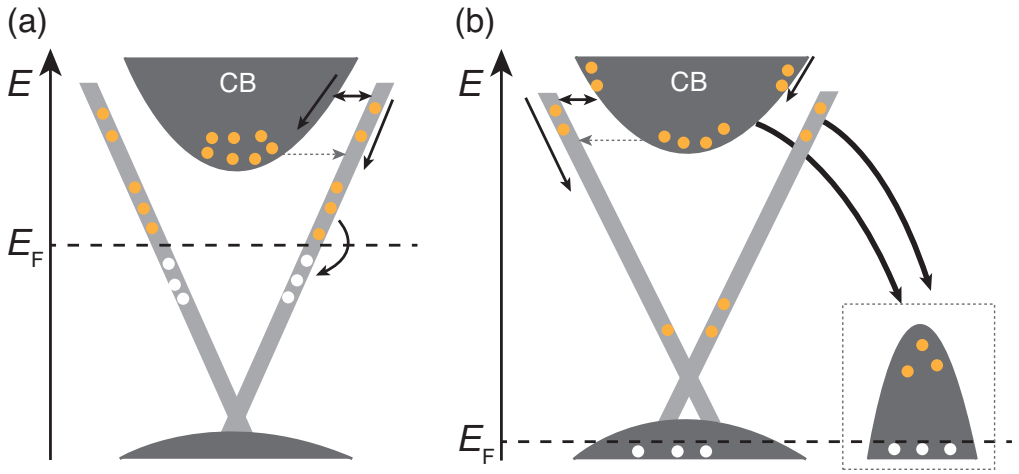

Figure 5.12: A schematic drawn of the band diagram with electron scattering process of (a) bulk-insulating $Bi_{1.5}Sb_{0.5}Te_{1.7}Se_{1.3}$, the present study, and (b) *p*-type Bi_2Se_3, the sample of the previous study [89].

estimated value indicates the own decay time of the metallic topological surface state between the insulating bulk energy gap.

The electron scattering process including electron-hole recombination of the bulk-insulating topological insulator discovered in the present study is shown in Fig. 5.12(a). This describes that the electrons of bulk conduction band have no scattering channel only except the surface state, similarly discussed in the previous study by *Sobota et al.*[89]. However, the result of the previous study shows no energy dependence of decay time between the bulk energy gap, and this is different with the present study. In case of Bi_2Se_3, the following idea can describe such a different behavior. Most of all, excessively hole doped Bi_2Se_3 is a bulk metallic topological insulator that its dynamics can be different with the present study for a bulk-insulating topological insulator. Moreover, the band calculation of Bi_2Se_3 [51, 52] shows that bulk valence band along the $\bar{\Gamma} - \bar{\mathrm{M}}$ direction positioned much higher energy than that on the $\bar{\Gamma}$ point as schematically drawn in Fig. 5.12(b). Thus, there is a possibility that another scattering channel between the bulk conduction and the bulk valence band by electron - phonon coupling exist, which results in the decrease of the electron density of the bulk conduction band. As well as, the electrons of the surface state can be also scattered into the bulk valence band, so that the decay time of the bulk conduction band and the surface state can be

almost same.

5.4 Conclusion

A dynamics of photoexcited electrons in the intrinsic three-dimensional topological insulator is clarified with TrARPES experiment. Due to the advantage of this pump-and-probe method with high energy resolution, the photoelectron intensity curves as a function of the delay time were taken at the various energies. The calculated decay times of the transient photoelectron intensity curves show the obvious energy dependence. Both topological surface state and the bulk conduction band have long lifetime beyond 10 ps near the Fermi level, in addition, even much longer lifetime was observed in the bulk conduction band. This delayed relaxation at the bulk conduction bottom was explained by the simulation of the simple scattering process model. According to the scattering process, the electrons of the bulk conduction band near the bottom have no other scattering channels except the surface state at the same energy. Due to the low DOS of the surface state, electrons are accumulated at the bulk conduction bottom. Moreover, the simulation gave us the decay parameter τ_s, which is the own decay time of the metallic surface state near the Fermi level. The result of $\tau_s \sim 4$ ps is similar order with the decay time of the surface state shown in Fig. 5.5(b) that it means the observed decay time, different with that of bulk conduction band, is the original value of intra-band scattering in the topological surface band. This is the most important point of the present experiment that it is the first proof, which observed the own decay time of the metallic surface state in the topological insulator. By comparing the transient characteristic of bulk-insulating sample with that of bulk metallic sample, which is due to the band shift, these scattering processes and the decay time proved to be the own feature of the bulk-insulating topological insulator. Even though it is difficult to discuss the electron scattering which depends on the spin-polarized property, the result is very important that it is the first experimental result to give the decay process of the two-dimensional metallic state between the intrinsic insulating bulk energy gap.

5. PHOTOEXCITED CARRIER DYNAMICS OF DIRAC FERMION IN THE INTRINSIC TOPOLOGICAL INSULATOR

Chapter 6

Summary

To summarize, the Dirac electrons dynamics has been investigated by STM and STS, as well as TrARPES. A combination of STS and TrARPES techniques is very powerful not only to study the electronic structures, but also to study such dynamics. Which leads the present work to the first experimental study about the Dirac electrons dynamics defined from both elastic and inelastic scattering in the ground and photoexcited state.

From the observed differential conductance images of $Bi_{1.5}Sb_{0.5}Te_{1.7}Se_{1.3}$ using STM, the spatial modulations originated in a result of quasi-particle interferences of surface electrons are found even in the energy range with circular constant energy contour of band dispersion. The amplitude of Fourier transformed differential conductance images suggest an existence of the critical scattering vector length. This critical scattering vector length is limited up to only 75 %, which indicates the maximum scattering angle is 100°. The result shows that not only the 180° backscattering, but also a rather wide range of the scattering angle between 100° and 180° are well prohibited due to the spin helical texture. The quantitative analysis for Dirac surface state elastic scattering suggests the backscattering is significantly suppressed angle dependency. This is the first understanding the scattering as a function of scattering angle experimentally. There is a question still we have, such as the sudden decrease of the scattering intensity, and in order to understand this property, the theoretical study for the angle dependent scattering probability considering the spin-orbit coupling is required to the future work.

The TrARPES measurement of $Bi_{1.5}Sb_{0.5}Te_{1.7}Se_{1.3}$ gave us the electron dynamics

of a bulk insulating topological insulator in non-equilibrium state. The time evolution of the energy dependent photoelectron intensity, measured on both topological surface state and bulk conduction band, reveal the lifetimes longer than 10 ps in both states. In particular, much longer lifetime is measured on the bulk conduction band. The simulation with the supposed scattering process reproduces the experimental result of this electron accumulation at the bottom of the bulk conduction band. According to the scattering process, the electrons at the bulk conduction bottom have the only one scattering channel to the surface state at the same energy and this makes the relaxation to be delayed. Even though electron filling from the bulk conduction band, the own decay time of the surface electron near the Fermi level was estimated from the present experimental results. This is the first experimental evidence of the original surface decay parameter in a three-dimensional topological insulator. Though it is hard to find the feature of the "spin-polarized", the present experiment is the first study to understand two-dimensional metallic surface state between the insulating bulk band gap and can give advantages to clarify the detailed dynamics of such a new state.

The TrARPES experiment gave us a lot of advancement to understand the dynamics of two-dimensional Dirac surface state in a bulk-insulating topological insulator. This is the first step to study the dynamics of the peculiar surface state that further experimental and theoretical studies are still necessary to find the representative dynamics of "topological surface state", for example, spin dependent suppression of electron scattering as described in the first half. Such a further study can give a lot of advantages not only to the fundamental physics, but also to the applications based on the spin polarized surface state in a bulk-insulating topological insulator.

Bibliography

[1] Hasan, M. Z. and Kane, C. L. Colloquium: Topological insulators. *Review of Modern Physics* **82**, 3045 (2010).

[2] Qi, X.-L. and Zhang, S.-C. Topological insulators and superconductors. *Review of Modern Physics* **83**, 1057 (2011).

[3] von Klitzing, K., Dorda, G. and Pepper, M. New method for high-accuracy determination of the fine-structure constant based on quantized Hall resistance. *Physical Review Letters* **45**, 494 (1980).

[4] Prange, R. E. and Girvin, S. M. *The quantum Hall effect* (Springer, 1987).

[5] Kane, C. L. and Mele, E. J. A new spin on the insulating state. *Science* **314**, 1692 (2006).

[6] Qi, X.-L. and Zhang, S.-C. The quantum spin Hall effect and topological insulators. *Physics Today* **63**, 33 (2010).

[7] Thouless, D. J., Kohmoto, M., Nightingle, M. P. and den Nijs, M. Quantized Hall conductance in a two-dimensional periodic potential. *Physical Review Letters* **49**, 405 (1982).

[8] Kohmoto, M. Topological invariant and the quantization of the Hall conductance. *Annals of Physics* **160**, 343 (1985).

[9] Nakahara, M. *Geometry, topology and physics* (IOP Publishing, 2003), 2nd edn.

[10] Haldane, F. D. M. Model for a quantum Hall effect without Landau levels: Condensed-matter realization of the "parity anomaly". *Physical Review Letters* **61**, 2015 (1988).

[11] Novoselov, K. S., Geim, A. K., Morozov, S. V., Jiang, D., Katsnelson, M. I., Grigorieva, I. V., Dubonos, S. V. and Firsov, A. A. Two-dimensional gas of massless Dirac fermions in graphene. *Nature* **438**, 197 (2005).

[12] Kane, C. L. and Mele, E. J. Quantum spin Hall effect in graphene. *Physical Review Letters* **95**, 226801 (2005).

[13] Bychkov, Y. A. and Rashba, E. I. Properties of a 2D electron gas with lifted spectral degeneracy. *Journal of Experimental and Theoretical Physics* **39**, 78 (1984).

[14] Wu, C., Bernevig, B. A. and Zhang, S.-C. Helical liquid and the edge of quantum spin Hall systems. *Physical Review Letters* **96**, 106401 (2006).

[15] Fu, L., Kane, C. L. and Mele, E. J. Topological insulators in three dimensions. *Physical Review Letters* **98**, 106803 (2007).

[16] Kane, C. L. and Mele, E. J. Z_2 topological order and the quantum spin Hall effect. *Physical Review Letters* **95**, 146802 (2005).

[17] Fu, L. and Kane, C. L. Time reversal polarization and a Z_2 adiabatic spin pump. *Physical Review B* **74**, 195312 (2006).

[18] Bernevig, B. A., Hughes, T. L. and Zhang, S.-C. Quantum spin Hall effect and topological phase transition in HgTe quantum wells. *Science* **314**, 1757 (2006).

[19] König, M., Wiedmann, S., Brüne, C., Roth, A., Buhmann, H., Molenkamp, L. W., Qi, X.-L. and Zhang, S.-C. Quantum spin Hall insulator state in HgTe quantum wells. *Science* **318**, 766 (2007).

[20] Novik, E. G., Pfeuffer-Jeschke, A., Jungwirth, T., Latussek, V., Becker, C. R. and Landwehr, G. Band structure of smimagnetic $Hg_{1-y}Mn_yTe$ quantum wells. *Physical Review B* **72**, 035321 (2005).

[21] Liu, C., Hughes, T. L., Qi, X.-L., Wang, K. and Zhang, S.-C. Quantum spin Hall effect in inverted type-ii semiconductors. *Physical Review Letters* **100**, 236601 (2008).

[22] Knez, I., Du, R.-R. and Sullivan, G. Evidence for hellical edge modes in inverted InAs/GaSb quantum wells. *Physical Review Letters* **107**, 136603 (2011).

[23] Knez, I., Du, R.-R. and Sullivan, G. Andreev reflection of helical edge modes in InAs/GaSb quantum spin Hall insulator. *Physical Review Letters* **109**, 186603 (2012).

[24] Murakami, S. Quantum spin Hall effect and enhanced magnetic response by spin-orbit coupling. *Physical Review Letters* **97**, 236805 (2006).

[25] Shitade, A., Katsura, H., Kuneš, J., Qi, X.-L., Zhang, S.-C. and Nagaosa, N. Quantum spin Hall effect in a transition metal oxide Na_2IrO_3. *Physical Review Letters* **102**, 256403 (2009).

[26] Hirahara, T., Bihlmayer, G., Sakamoto, Y., Yamada, M., Miyazaki, H., Kimura, S.-I., Blügel, S. and Hasegawa, S. Interfacing 2D and 3D topological insulator: Bi(111) bilayer on Bi_2Te_3. *Physical Review Letters* **107**, 166801 (2011).

[27] Yang, F., Miao, L., Wang, Z. F., Yao, M.-Y., Zhu, F., Song, Y. R., Wang, M.-X., Xu, J.-P., Fedorov, A. V., Sun, Z., Zhang, G. B., Liu, C., Liu, F., Qian, D., Gao, C. L. and Jia, J.-F. Spatial and energy distribution of topological edge states in single Bi(111) bilayer. *Physical Review Letters* **109**, 016801 (2012).

[28] Sabater, C., Gosálbez-Martínez, D., Fernández-Rossier, J., Rodrigo, J. G., Untiedt, C. and Palacios, J. J. Topologically protected quantum transport in locally exfoliated bismuth at room tempertature. *Physical Review Letters* **110**, 176802 (2013).

[29] Moore, J. E. and Balents, L. Topological invariants of time-reversal-invariant band structures. *Physical Review B* **75**, 121306(R) (2007).

[30] Fu, L. and Kane, C. L. Topological insulators with inversion symmetry. *Physical Review B* **76**, 045302 (2007).

[31] Roy, R. Topological phases and the quantum spin hall effect in three dimensions. *Physical Review B* **79**, 195322 (1009).

[32] Hsieh, D., Qian, D., Wray, L., Xia, Y., Hor, Y. S., Cava, R. J. and Hasan, M. Z. A topological Dirac insulator in a quantum spin Hall phase. *Nature* **452**, 970 (2008).

[33] Brüne, C., Liu, C. X., Novik, E. G., Hankiewicz, E. M., Buhmann, H., Chen, Y. L., Shen, Z. X., Zhang, S. C. and Molenkamp, L. W. Quantum Hall effect from the topological surface states of strained bulk HgTe. *Physical Review Letters* **106**, 126803 (2011).

[34] Lenoir, B., Cassart, M., Michenaud, J.-P., Scherrer, H. and Scherrer, S. Transport properties of Bi-rich Bi-Sb alloys. *Journal of Physics and Chemistry of Solids* **57**, 89 (1996).

[35] Hsieh, D., Xia, Y., Wray, L., Qian, D., Pal, A., Dil, J. H., Osterwalder, J., Meier, F., Bihlmayer, G., Kane, C. L., Hor, Y. S., Cava, R. J. and Hasan, M. Z. Observation of unconventional quantum spin textures in topological insulators. *Science* **323**, 919 (2009).

[36] Nishide, A., Taskin, A. A., Takeichi, Y., Okuda, T., Kakizaki, A., Hirahara, T., Nakatsuji, K., Komori, F., Ando, Y. and Matsuda, I. Direct mapping of the spin-filtered surface bands of a three-dimensional quantum spin Hall insulator. *Physical Review B* **81**, 041309(R) (2010).

[37] Okuda, T., Takeichi, Y., Maeda, Y., Harasawa, A., Matsuda, I., Kinoshita, T. and Kakizaki, A. A new spin-polarized photoemission spectrometer with very high efficiency and energy resolution. *Review of Scientific Instruments* **79**, 123117 (2008).

[38] Roushan, P., Seo, J., Parker, C. V., Hor, Y. S., Hsieh, D., Qian, D., Richardella, A., Hasan, M. Z., Cava, R. J. and Yazdani, A. Topological surface states protected from backscattering by chiral spin texture. *Nature* **460**, 1106 (2009).

[39] Mishra, S. K., Satpathy, S. and Jepsen, O. Electronic structure and thermoelectric properties of bismuth telluride and bismuth selenide. *Journal of Physics: Condensed Matter* **9**, 461 (1997).

[40] Zhang, H., Liu, C.-X., Qi, X.-L., Dai, X., Fang, Z. and Zhang, S.-C. Topological insulators in Bi_2Se_3, Bi_2Te_3 and Sb_2Te_3 with a single Dirac cone on the surface. *Nature Physics* **5**, 438 (2009).

[41] Xia, Y., Qian, D., Hsieh, D., Wray, L., Pal, A., Lin, H., Bansil, A., Grauer, D., Hor, Y. S., Cava, R. J. and Hasan, M. Z. Observation of large-gap topological-insulator class with a single Dirac cone on the surface. *Nature Physics* **5**, 398 (2009).

[42] Chen, Y. L., Analytis, J. G., Chu, J.-H., Liu, Z. K., Mo, S.-K., Qi, X. L., Zhang, H. J., Lu, D. H., Dai, X., Fang, Z., Zhang, S. C., Fisher, I. R., Hussain, Z. and Shen, Z. X. Experimental realization of a three-dimensional topological insulator, Bi_2Te_3. *Science* **325**, 178 (2009).

[43] Hor, Y. S., Richardella, A., Roushan, P., Xia, Y., Checkeisky, J. G., Yazdani, A., Hasan, M. Z., Ong, N. P. and Cava, R. J. p-type Bi_2Se_3 for topological insulator and low-temperature thermoelectric applications. *Physical Review B* **79**, 195208 (2009).

[44] Hsieh, D., Xia, Y., Qian, D., Wray, L., Dil, J. H., Meier, F., Osterwalder, J., Patthey, L., Checkeisky, J. G., Ong, N. P., Fedorov, A. V., Lin, H., Bansil, A., Grauer, D., Hor, Y. S., Cava, R. J. and Hasan, M. Z. A tunable topological insulator in the spin helical Dirac transport regime. *Natrue* **460**, 1101 (2009).

[45] Hsieh, D., Xia, Y., Qian, D., Wray, L., Meier, F., Dil, J. H., Osterwalder, J., Patthey, L., Fedorov, A. V., Lin, H., Bansil, A., Grauer, D., Hor, Y. S., Cava, R. J. and Hasan, M. Z. Observation of time-reversal protected single-Dirac-cone topological insulator states in Bi_2Te_3 and Sb_2Te_3. *Physical Review Letters* **103**, 146401 (2009).

[46] Pan, Z.-H., Vescovo, E., Fedorov, A. V., Gardner, D., Lee, Y. S., Chu, S., Gu, G. D. and Valla, T. Electronic structure of the topological insulator Bi_2Se_3 using angle-resolved photoemission spectroscopy: Evidence for a nearly full surface spin polarization. *Physical Review Letters* **106**, 257004 (2011).

[47] Souma, S., Kosaka, K., Sato, T., Komatsu, M., Takayama, A., Takahashi, T., Kriener, M., Segawa, K. and Ando, Y. Direct measurement of the out-of-

plane spin texture in the Dirac-cone surface state of a topological insulator. *Physical Review Letters* **106**, 216803 (2011).

[48] Miyamoto, K., Kimura, A., Okuda, T., Miyahara, H., Kuroda, K., Namatame, H., Taniguchi, M., Eremeev, S. V., Menshchikova, T. V., Chulkov, E. V., Kokh, K. A. and Tereshchenko, O. E. Topological surface states with persistent high spin polarization across the Dirac point in Bi_2Te_2Se and Bi_2Se_2Te. *Physical Review Letters* **109**, 166802 (2012).

[49] Eto, K., Ren, Z., Taskin, A. A., Segawa, K. and Ando, Y. Angular-dependent oscillations of the magnetoresistance in Bi_2Se_3 due to the three-dimensonal bulk Fermi surface. *Physical Review B* **81**, 195309 (2010).

[50] Qu, D.-X., Hor, Y. S., Xiong, J., Cava, R. J. and Ong, N. P. Quantum oscillations and Hall anomaly of surface states in the topological insulator Bi_2Te_3. *Science* **329**, 821 (2010).

[51] Kim, S., Ye, M., Kuroda, K., Yamada, Y., Krasovskii, E. E., Chulkov, E. V., Miyamoto, K., Nakatake, M., Okuda, T., Ueda, Y., Shimada, K., Namatame, H., Taniguchi, M. and Kimura, A. Surface scattering via bulk continuum states in the 3D topological insulator Bi_2Se_3. *Physical Review Letters* **107**, 056803 (2011).

[52] Romanowich, M., Lee, M.-S., Chung, D.-Y., Mahanti, S. D., Kanatzidis, M. G. and Tessmer, S. H. Interplay of topological surface and bulk electronic states in Bi_2Se_3. *Physical Review B* **87**, 085310 (2013).

[53] Sato, T., Segawa, K., Guo, H., Sugawara, K., Souma, S., Takahashi, T. and Ando, Y. Direct evidence for the Dirac-cone topological surface states in the ternary chalcogenide $TlBiSe_2$. *Physical Review Letters* **105**, 136802 (2010).

[54] Kuroda, K., Ye, M., Kimura, A., Eremeev, S. V., Krasovskii, E. E., Chulkov, E. V., Ueda, Y., Miyamoto, K., Okuda, T., Shimada, K., Namatame, H. and Taniguchi, M. Experimental realization of a three-dimensional topological insulator phase in ternary chalcogenide $TlBiSe_2$. *Physical Review Letters* **105**, 146801 (2010).

[55] Chen, Y. L., Liu, Z. K., Analytis, J. G., Chu, J.-H., Zhang, H. J., Yan, B. H., Mo, S.-K., Moore, R. G., Lu, D. H., Fisher, I. R., Zhang, S. C., Hussain, Z. and Shen, Z. X. Single Dirac cone topological surface state and unusual thermoelectric property of mopounds from a new topological insulator family. *Physical Review Letters* **105**, 266401 (2010).

[56] Souma, S., Eto, K., Nomura, M., Nakayama, K., Sato, T., Takahashi, T., Segawa, K. and Ando, Y. Topological surface states in lead-based ternary telluride $Pb(Bi_{1-x}Sb_x)_2Te_4$. *Physical Review Letters* **108**, 116801 (2012).

[57] Kuroda, K., Miyahara, H., Ye, M., Eremeev, S. V., Koroteev, Y. M., Krasovskii, E. E., Chulkov, E. V., Hiramoto, S., Moriyoshi, C., Kuroiwa, Y., Miyamoto, K., Okuda, T., Arita, M., Shimada, K., Namatame, H., Taniguchi, M., Ueda, Y. and Kimura, A. Experimental verification of $PbBi_2Te_4$ as a 3D topological insulator. *Physical Review Letters* **108**, 206803 (2012).

[58] Neupane, M., Xu, S.-Y., Wray, L. A., Petersen, A., Shankar, R., Alidoust, N., Liu, C., Fedorov, A., Ji, H., Allred, J. M., Hor, Y. S., Chang, T.-R., Jeng, H.-T., Lin, H., Bansil, A., Cava, R. J. and Hasan, M. Z. Topological surface states and Dirac point tuning in ternary topological insulators. *Physical Review B* **85**, 235406 (2012).

[59] Okamoto, K., Kuroda, K., Miyahara, H., Miyamoto, K., Okuda, T., Aliev, Z. S., Babanly, M. B., Amiraslanov, I. R., Shimada, K., Namatame, H., Taniguchi, M., Samorokov, D. A., Menshchikova, T. V., Chulkov, E. V. and Kimura, A. Observation of a highly spin-polarized topological surface state in $GeBi_2Te_4$. *Physical Review B* **86**, 195304 (2012).

[60] Binnig, G., Rohrer, H., Gerber, C. and Weibel, E. Surface studies by scanning tunneling microscopy. *Physical Review Letters* **49**, 57 (1981).

[61] Binnig, G., Rohrer, H., Gerber, C. and Weibel, E. Tunneling though a controllable vacumm gap. *Applied Physics Letters* **40**, 178 (1982).

[62] Binnig, G., Rohrer, H., Gerber, C. and Weibel, E. 7×7 reconstruction on Si(111) resolved in real space. *Physcal Review Letters* **50**, 120 (1983).

[63] Binnig, G. and Rohrer, H. Scanning tunneling microscopy - from birth to adolescence. *Review of Modern Physics* **59**, 615 (1987).

[64] Bardeen, J. Tunnelling from a many-particle point of view. *Physical Review Letters* **6**, 57 (1961).

[65] Tersoff, J. and Hamann, D. R. Theory of application for the scanning tunneling microscope. *Physical Review Letters* **50**, 1998 (1983).

[66] Crommie, M. F., Lutz, C. P. and Eigler, D. M. Imaging standing waves in a two-dimensional electron gas. *Nature* **363**, 524 (1993).

[67] Hasegawa, Y. and Avouris, P. Direct observation of standing wave formation at surface steps using scanning tunneling spectroscopy. *Physical Review Letters* **71**, 1071 (1993).

[68] Petersen, L., Sprunger, P. T., Hofmann, P., Laegsgaard, E., Briner, B. G., Doering, M., Rust, H.-P., Bradshaw, A. M., Besenbacher, F. and Plummer, E. W. Direct imaging of the two-dimensional Fermi contour: Fourier-transform STM. *Physical Review B* **57**, R6858 (1998).

[69] Hoffman, J. E., McElroy, K., Lee, D.-H., Lang, K. M., Eisaki, H., Uchida, S. and Davis, J. C. Imaging quasiparticle interference in $Bi_2SrCaCu_2O_{8+\delta}$. *Science* **297**, 1148 (2002).

[70] Hüfner, S. *Photoelectron spectroscopy* (Springer, 2003), 3rd edn.

[71] Seah, M. P. and Dench, W. A. Quantitative electron spectroscopy of surface: A standard data base for electron inelastic mean free path in solids. *Surface and Interface Analysis* **1**, 2 (1979).

[72] Haight, R. Electron dynamics at surfaces. *Surface Science Reports* **21**, 275 (1995).

[73] Ishida, Y., Togashi, T., Yamamoto, K., Tanaka, M., Kiss, T., Otsu, T., Kobayashi, Y. and Shin, S. Time-resolved photoemission apparatus achieving sub-20-meV energy resolution and high stability. *Review of Scientific Instruments* **85**, 123904 (2014).

[74] Ishida, Y., Togashi, T., Yamamoto, K., Tanaka, M., Taniuchi, T., Kiss, T., Nakajima, M., Suemoto, T. and Shin, S. Non-thermal hot electrons ultrafastly generating hot optical phonons in graphite. *Scientific Reports* **1**, 64 (2011).

[75] Hanaguri, T., Igarashi, K., Kawamura, M., Takagi, H. and Sasagawa, T. Momentum-resolved Landau-level spectroscopy of Dirac surface state in Bi_2Se_3. *Physical Review B* **82**, 081305(R) (2010).

[76] Zhang, T., Cheng, P., Chen, X., Jia, J.-F., Ma, X., He, K., Wang, L., Zhang, H., Dai, X., Fang, Z., Xie, X. and Xue, Q.-K. Experimental demonstration of topological surface states protected by time-reversal symmetry. *Physical Review Letters* **103**, 266803 (2009).

[77] Alpichshev, Z., Analytis, J. G., Chu, J.-H., Fisher, I. R., Chen, Y. L., Shen, Z. X., Fang, A. and Kapitulnik, A. STM imaging of electronic waves on the surface of Bi_2Te_3: Topologically protected surface states and hexagonal warping effects. *Physical Review Letters* **104**, 016401 (2010).

[78] Okada, Y., Dhital, C., Zhou, W., Huemiller, E. D., Lin, H., Basak, S., Bansil, A., Huang, Y.-B., Ding, H., Wang, Z., Wilson, S. D. and Madhavan, V. Direct observation of broken time-reversal symmetry on the surface of a magnetically doped topological insulator. *Physical Review Letters* **106**, 206805 (2011).

[79] Beidenkopf, H., Roushan, P., Seo, J., Gorman, L., Drozdov, I., Hor, Y. S., Cava, R. J. and Yazdani, A. Spatial fluctuations of helical Dirac fermions on the surface of topological insulators. *Nature Physics* **7**, 939 (2011).

[80] Kuroda, K., Arita, M., Miyamoto, K., Ye, M., Jiang, J., Kimura, A., Krasovskii, E. E., Chulkov, E. V., Iwasawa, H., Okuda, T., Shimada, K., Ueda, Y., Namatame, H. and Taniguchi, M. Hexagonally deformed Fermi surface on the 3D topological insulator Bi_2Se_3. *Physical Review Letters* **105**, 076802 (2010).

[81] Fu, L. Hexagonal warping effects in the surface states of the topological insulator Bi_2Te_3. *Physical Review Letters* **103**, 266801 (2009).

[82] Zhou, X., Fang, C., Tsai, W.-F. and Hu, J. Theory of quasiparticle scattering in a two-dimensional system of helical Dirac fermions: Surface band structure of a three-dimensional toplogical insulator. *Physical Review B* **80**, 245317 (2009).

[83] Ren, Z., Taskin, A. A., Sasaki, S., Segawa, K. and Ando, Y. Large bulk resistivity and surface quantum oscillations in the topological insulator Bi_2Te_2Se. *Physical Review B* **82**, 241306 (2010).

[84] Taskin, A. A., Ren, Z., Sasaki, S., Segawa, K. and Ando, Y. Observation of Dirac holes and electrons in a toplogical insulator. *Physical Review Letters* **107**, 016801 (2011).

[85] Arakane, T., Sato, T., Souma, S., Kosaka, K., Nakayama, K., Komatsu, M., Takahashi, T., Ren, Z., Segawa, K. and Ando, Y. Tunable dirac cone in the topological insulator $Bi_{2-x}Sb_xTe_{3-y}Se_y$. *Nature Communications* **3**, 636 (2012).

[86] Zhang, J., Chang, C.-Z., Zhang, Z., Wen, J., Feng, X., Li, K., Liu, M., He, K., Wang, L., Chen, X., Xue, Q.-K., Ma, X. and Wang, Y. Band structure engineering in $(Bi_{1-x}Sb_x)_2Te_3$ ternary topological insulators. *Nature Communications* **2**, 574 (2011).

[87] Ren, Z., Taskin, A. A., Sasaki, S., Segawa, K. and Ando, Y. Optimizing $Bi_{2-x}Sb_xTe_{3-y}Se_y$ solid solutions to approach the intrinsic topological insulator regime. *Physical Review B* **84**, 165311 (2011).

[88] Kim, S., Yoshizawa, S., Ishida, Y., Eto, K., Segawa, K., Ando, Y., Shin, S. and Komori, F. Robust protection from backscattering in the topological insulator $Bi_{1.5}Sb_{0.5}Te_{1.7}Se_{1.3}$. *Physical Review Letters* **112**, 136802 (2014).

[89] Sobota, J. A., Yang, S., Analytis, J. G., Chen, Y. L., Fisher, I. R., Kirchmann, P. S. and Shen, Z. X. Ultrafast optical excitation of a persistent surface-state population in the topological insulator Bi_2Se_3. *Physical Review Letters* **108**, 117403 (2012).

[90] Kohsaka, Y., Taylor, C., Fujita, K., Schmidt, A., Lupien, C., Hanaguri, T., Azuma, M., Takano, M., Eisaki, H., Takagi, H., Uchida, S. and Davis, J. C.

An intrinsic bond-centered electronic glass with unidirectional domains in underdoped cuprates. *Science* **315**, 1380 (2007).

[91] Himpsel, F. J. and Fauster, T. Empty orbitals of adsorbates determined by inverse ultraviolet photoemission. *Physical Review Letters* **49**, 1583 (1982).

[92] Hüfner, S., Osterwalder, J., Reisterer, T. and Hulliger, F. Photoemission and inverse photoemission spectroscopy of NiO. *Solid State Communications* **52**, 793 (1984).

[93] See, A. K., Thayer, M. and Bartynski, R. A. Angle-resolved inverse-photoemission study of the nearly perfect $TiO_2(110)$ surface. *Physical Review B* **47**, 13722 (1993).

[94] Sato, H., Arita, M., Utsumi, Y., Mukaegawa, Y., Sasaki, M., Ohnishi, A., Kitaura, M., Namatame, H. and Taniguchi, M. Conduction-band electronic structure of 1t-TaS_2 revealed by angle-resolved inverse-photoemission spectroscopy. *Physical Review B* **89**, 155137 (2014).

[95] Jiang, R., Wang, L.-L., Huang, M., Dhaka, R. S., Johnson, D. D., Lograsso, T. A. and Kaminski, A. Reversible tuning of the surface state in a pseudobinary $Bi_2(Te-Se)_3$ topological insulator. *Physical Review B* **86**, 085112 (2012).

[96] Chen, Y. L., Chu, J.-H., Analytis, J. G., Liu, Z. K., Igarashi, K., Kuo, H.-H., Qi, X. L., Mo, S. K., Moore, R. G., Lu, D. H., Hashimoto, M., Sasagawa, T., Zhang, S. C., Fisher, I. R., Hussain, Z. and Shen, Z. X. Massive Dirac fermion on the surface of a magnetically doped topological insulator. *Science* **329**, 659 (2010).

[97] McElroy, K., Simmonds, R. W., Hoffman, J. E., Lee, D.-H., Orenstein, J., Eisaki, H., Uchida, S. and Davis, J. C. Relating atomic-scale electronic phenomena to wave-like quasiparticla states in superconducting $Bi_2Sr_2CaCu_2O_{8+\delta}$. *Nature* **422**, 592 (2003).

[98] Vishik, I. M., Nowadnick, E. A., Lee, W. S., Shen, Z. X., Moritz, B., Devereaux, T. P., Tanaka, K., Sasagawa, T. and Fujii, T. A momentum-

dependent perspective on quasiparticle interference in $Bi_2Sr_2CaCu_2O_{8+\delta}$. *Nature Physics* **5**, 718 (2009).

[99] Nechaev, I. A., Jensen, M. F., Rienks, E. D. L., Silkin, V. M., Echenique, P. M., Chulkov, E. V. and Hofmann, P. Hole dynamics in a two-dimensional spin-orbit coupled electron system: Theoretical and experimental study of the Au(111) surface state. *Physical Review B* **80**, 113402 (2009).

[100] Zhou, X. J., Wannberg, B., Yang, W. L., Brouet, V., Sun, Z., Douglas, J. F., Dessau, D., Hussain, Z. and Shen, Z. X. Space charge effect and mirror charge effect in photoemission spectroscopy. *Journal of Electron Spectroscopy and Related Phenomena* **142**, 27 (2005).

[101] Passlack, S., Mathias, S., Andreyev, O., Mittnacht, D., Aeschlimann, M. and Bauer, M. Space charge effects in photoemission with a low repetition, high intensity femtosecond laser source. *Journal of Applied Physics* **100**, 024912 (2006).

[102] Marsi, M., Belkhou, R., Grupp, C., Panaccione, G., Taleb-Ibrahimi, A., Nahon, L., Garzella, D., Nutarelli, D., Renault, E., Roux, R., Couprie, M. E. and Billardon, M. Transient charge carrier distribution at UV-photoexcited SiO_2/Si interfaces. *Physical Review B* **61**, R5070 (2000).

[103] Ishida, Y., Otsu, T., Shimada, T., Okawa, M., Kobayashi, Y., Iga, F., Takabatake, Y. and Shin, S. Emergent photovoltage on SmB_6 surface upon bulk-gap evolution revealed by pump-and-probe photoemission spectroscopy. Submitted.

[104] Hajlaoui, M., Papalazarou, E., Mauchain, J., Lantz, G., Moisan, N., Boschetto, D., Jiang, Z., Miotkowski, I., Chen, Y. P., Taleb-Ibrahimi, A., Perfetti, L. and Marsi, M. Ultrafast surface carrier dynamics in the topological insulator Bi_2Te_3. *Nano Letters* **12**, 3532 (2012).

[105] Park, S. R., Jung, W. S., Kim, C., Song, D. J., Kim, C., Kimura, S., Lee, K. D. and Hur, N. Quasiparticle scattering and the protected nature of the topological states in a parent topological insulator Bi_2Se_3. *Physical Review B* **81**, 041405(R) (2010).